UCLouvain

École polytechnique de Louvain

Rehab Robotics - Open-loop identification of a 2 degrees of freedom rehabilitation robot actuated with pneumatic artificial muscles

Authors: **Julien Guiaux Brinon, Luana Marsano da Costa Nunes**
Supervisors: **Renaud Ronsse, Benoît Herman**
Readers: **Bertrand Tondu, Frédéric Crevecoeur, Rafael Traldi Moura**
Academic year 2021–2022
Master [120] in Electro-mechanical Engineering

Abstract

Context Nowadays, the number of stroke victims continues to grow over the years. The resulting motor impairments are manifold and have a strong impact on the daily life of the affected person. To recover the lost skills, an intensive, adapted and repetitive rehabilitation procedure is essential. As those movements and the associated programs are time consuming and must be optimized, the robots progressively entered the medical field to assist therapists those last decades.

Objectives A pneumatic artificial muscles actuated robot was developed by Louvain Bionics and INSA Toulouse with the aim of post-stroke upper-limb rehabilitation. The objectives of this thesis are to solve the previously identified mechanical problems and to perform open-loop characterization of the device, highlighting its limitations and identifying its dynamics and the one of its actuators. This knowledge helps to better understand the robot overall behavior, guiding in the closed loop control design and bringing it a step closer to the project objective of finding out if this type of actuators has enough advantages with respect to classical electric motors to enter the medical field.

Experiments A systematic experimental approach was used throughout the entire project. Static and dynamic measurements of end-effector position and interaction forces with the user were performed and the data was used to identify the mass-spring-damper model parameters using temporal and frequency approaches and to validate the obtained results. Then, by applying force steps as inputs, with the robot maintained at a fixed position, and measuring the developed force at the handle, the system step response was constructed to identify the pressure regulators transfer function.

Results The investigations on the pneumatic artificial muscle actuated robot have shown promising abilities in torque and stiffness depending, however, on the geometrical configuration of the robot. It is demonstrated that the robot dynamics can be described by a mass-spring-damper system and the pressure regulators dynamics by a second order transfer function. Both must, nevertheless, have adaptive parameters evolving with the spatial position. The device has good prospects to enter the medical field if associated with a closed loop controller in order to adapt the performances to rehabilitation tasks.

Acknowledgments

The accomplishment of a master thesis is a demanding task and a long-term project combining multiple skills. Its proper completion can be attributed to our work but would not have been possible without the significant support of some people. Therefore, we would like to thank them greatly.

Firstly, we would like to thank our two supervisors, Prof. Renaud Ronsse and Prof. Benoît Herman, for their support and guidance throughout the year. Through their advice and discussions during our many meetings, they will have enabled us to carry out the thesis and to acquire new skills and knowledge, all of this in a pleasant and stimulating environment.

We also want to thank Prof. Bertrand Tondu, from the National Institute of Applied Sciences of Toulouse, for the material and expertise he was able to provide. The passionate discussion we had along with the multiple exchanges were of great interest for the research we were developing.

Thanks to the other two members of our jury, Prof. Frédéric Crevecoeur (UCLouvain) and Prof. Rafael Traldi Moura (University of São Paulo), for their interest in our work and for accepting to contribute their experience to the evaluation of our thesis.

We thank the team of mechanics and machinists of the CREDEM, in particular Vincent Musette for the machining of parts. Thanks to Antonin Dineur and Antoine Bietlot for their expertise concerning the software and electronics used. Thanks to Alex Bertholet for his help concerning the force sensor and its electronics.

We also want to thank all the friends for their support along this year, their advice and the considerable proofreading they have done. Thanks to our respective families that never stopped encouraging us and believing in the success of our studies.

Finally, we would like to highlight the pleasant dynamic that accompanied our daily work. All along the year, we have been a team at work and good friends on the side. We are grateful for the mutual support and investment in this important part of our academic journey.

Contents

Nomenclature

Acronyms

DoF	Degree of Freedom
I/P	Intensity/Pressure (converters)
CNS	Central Nervous System
PAM	Pneumatic Artificial Muscle
PID	Proportional Integral Derivative (controller)
PMA	Pneumatic Muscle Actuator
KBM	Mass-spring-damper (model)
D-H	Denavit-Hartenberg (convention)
MSE	Mean Squared Error
R^2	Coefficient of determination (statistics)

Dimensional variables

ε_i	Contraction ratio of muscle i
ε_0	Initial contraction ratio of the muscle
$R_{(i)}$	Radius of the pulley (of joint i)
$D_{(i)}$	Diameter of the pulley (of joint i)
l_{init}	Initial length of the muscle
l_0	Unloaded length of the muscle
l	Length of the muscle
δl_i	Initial shortening length of the muscle i = 1,2
L_i	Length of the segment i = 1,2

Angular variables

θ_i	Angle of the joint i = 1,2 in the conventional Denavit-Hartenberg (reference) frame
α_i	Angle of the joint i = 1,2 measured by the encoders, with respect to the initial configuration
α_0	Constant angle between the theta and alpha conventions (i.e. between reference and rotated frames)
$\theta_{i,init}$	Initial angular position of the joints in the reference frame
$\Delta\alpha_i$	Angular range of joint i = 1,2

Model variables

τ_i	Torque developed by joint i = 1,2
u_i	Command in pressure sent to muscle i = 1-4
P_i	Pressure inside muscle i = 1-4
K_j	Stiffness developed by joint j = 1,2 $\left[\frac{Nm}{rad}\right]$
B_j	Damping developed by joint j = 1,2 $\left[\frac{Nm \cdot s}{rad}\right]$
I	Inertia matrix of the robot segments $\left[\frac{Nm \cdot s^2}{rad}\right]$
K_C	Cartesian stiffness matrix of the robot $\left[\frac{N}{m}\right]$
B_C	Cartesian Damping matrix of the robot $\left[\frac{N \cdot s}{m}\right]$
M_C	Cartesian mass matrix of the robot $[kg]$
F	Force vector in the reference frame
(F_x, F_y)	End-effector forces expressed in the user/workspace frame
(X, Y)	Coordinates of the end-effector in the user/workspace frame
(V_x, V_y)	Speed of the end-effector in the user/workspace frame

Other notations/variables

(x_{w0}, y_{w0})	Fixed reference ("world") frame following the Denavit-Hartenberg convention
(x_{r0}, y_{r0})	Fixed "rotated" frame aligned with the initial configuration of the robot
(x_{u0}, y_{u0})	Fixed "user" frame aligned with the workspace
J	Jacobian operator/matrix
${}^{i}R_{j}$	Rotation matrix from frame j to frame i
Z	Impedance matrix of the system
m	Mass
c	Damping factor
k	Stiffness coefficient
G	Transfer function Gain
ζ	Transfer function damping ratio
ω_n	Transfer function natural frequency
M_p	Overshoot of the system
t_p	Peak time of the system

Introduction

Stroke is a medical condition with a global prevalence of more than 100 million people each year and remain the most common neurological condition found in the health care system[1]. The risks increase with age but a stroke can happen at any age. Among the survivors, the full functional recovery is relatively rare as more than 80% of the victims suffer from long-term disability [2].

Stroke consequences depend on the area of the brain in which it occurs and can be physical, cognitive, visual, sensory, perceptual or a combination of those. The mobility and abilities to perform everyday tasks are commonly and severely impacted, leading to reduced quality of life as well as poor psychological health. This usually results in discouraged people and even depression which hinders a good rehabilitation.

The medical emergency of a strokes requires immediate attention. The rehabilitation timing is crucial, the sooner it begins, the greater are the chances to regain lost abilities and daily life functions. To this aim, repetitive practice well-focused on the skills impaired and dedicated to stimulate the musculoskeletal system and the dedicated cortical areas is required. This rehabilitation process and the results associated are usually heterogeneous and patient dependant.

The role of technologies in stroke rehabilitation has become prevalent this last decades. As technology advances, innovative techniques and devices are appearing in the medical field, aiming to guide and improve the existing techniques or proposing new therapeutic programs [3]. One of the possible scenarios is the integration of robots in the process to optimize the proposed treatments, to reduce the therapist's workload, to save time and to make the rehabilitation tasks patient specific. The robot can provide an active accompaniment for repetitive tasks that will be designed depending on the motor function we are seeking to rehabilitate. The resistance or aid to movement should be adjusted depending on the target exercise, the evolution of the rehabilitation and even over one rehabilitation session. Next to this, it should provide precise measurements of the developed force, the current position in the workspace and quantify the evolution of the motor impairment of the patient. This tracking could then help to adapt and reorganise the strategy to both improve the effects on the impaired functions but also to keep the subject motivated. It is quite common to provide a feedback in real-time as well as a visual support to enhance the encouragement via an entertaining interface.

With this in mind, a project has been developed in a collaboration between

Louvain Bionics (UCLouvain) and INSA Toulouse in order to develop a robotic arm to rehabilitate victims of stroke. Some previous works aimed to study robots actuated by conventional electric motorisation while this research will try to identify the potential benefits of pneumatic actuation. The interests are already identified and are for example: the analogous behaviour of the pneumatic artificial muscles with the human skeletal ones, the compliance to the movement and the ability to control the implemented stiffness. However, the contribution of this thesis will be focused on a quantification and discussion of those benefits.

The project presented here is a continuation of previous researches. Therefore, the device that will be described and studied was already existing at the beginning of the thesis. However, some mechanical adjustments were needed in order to solve problems which have been identified in the previous thesis [4]. The implemented system is a 2 degree of freedom Scara robot in a planar configuration and thus composed of arm and forearm linked by revolute joints. The first objective was thus a mechanical redesign of some parts of the robot to be able to exploit the two joints over the entire workspace.

The results of the previous thesis consisted in a modeling of the force developed by the muscle used, a characterization of the force and stiffness limits of the robot and two proposed controllers, one low level and one based on an hybrid control in torque and stiffness. This was experimentally verified for the second joint only due to mechanical problems. This thesis then aims, at first, to develop a model based characterization of the torque and stiffness limits of both joints of the robot over the whole workspace. Then, to perform the identification and characterization of the device dynamics in the user frame. And finally, to identify the dynamic of the pressure regulators (Intensity to Pressure converters) controlling the pneumatic muscle actuators. To this aim, a systematic approach is used combining theoretical models and an experimental approach to obtain data, used to fit and validate of the models.

In other words, the global system in open loop can be represented as presented in the figure below and the dynamics characterization consists in identifying the red box while the regulators dynamics characterization attempts to identify the dashed box.

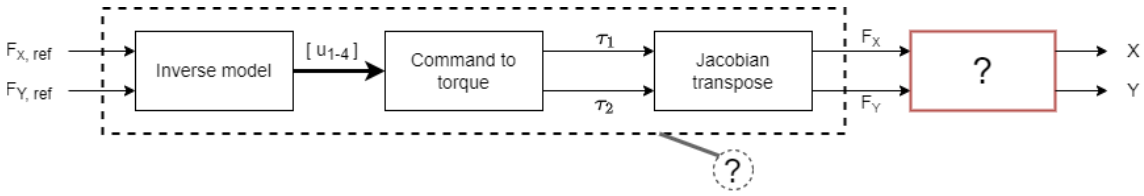

Global block diagram of the open loop system

In this diagram, $F_{X,ref}$ and $F_{Y,ref}$ are the commands in force expressed in the workspace Cartesian frame, $u_{[1-4]}$ are the pressure commands, τ_1 and τ_2 are the joint torques, F_X and F_Y represent the forces developed by the robot in the workspace-

attached frame and (X,Y) are the end-effector position in the same frame. The inverse model as well as the Jacobian and its transpose have already developed and are thus known.

The report will give, in chapter 1 an insight about the current state of the art of the research in neurorehabilitaion and the related therapies, the robots currently used or under development for rehabilitation purposes, the pneumatic artificial muscle technologies and the existing open loop identification methods. Chapter 2 will present a global overview of the system, the mechanical re-design that has been performed, the robot and the frame used to describe its behaviour and the principle of actuation based on the pneumatic muscles. The chapter 3 aims to characterize the torque and stiffness limits of the robot. Therefore, a verification of the force model applied to the current configuration of the robotic arm will be done, after which a model based characterization of the limits will be developed to derive the torque and stiffness domains in function of the joint angles. The open loop identification of the robot dynamics is performed in chapter 4 which first develops the theory in the Cartesian domain, explains how the data has been post-processed and then identifies the parameters expressing the dynamics using a temporal and frequency fit method. Both are compared and the accuracy of the obtained model is experimentally verified afterwards. Chapter 5 explains the open loop identification of the pressure regulator dynamics by considering the component limitations and the step response of the system (measured force for an imposed force command). Finally, the chapter 6 will conclude the thesis and propose areas of improvement.

Chapter 1

State of the art

This chapter aims to give an insight about the current state of the research areas related to the subject of the thesis. The close connection between the medical field and the robotic world arising from the topic of the work ahead, the first part of the chapter will focus on a description of the neurorehabilitation principles and present the existing therapies. Later on, a description of the existing technologies for robot-enhanced rehabilitation will be presented as well as an introduction to pneumatic artificial muscle actuators, their various types and operation principle. An overview of the open loop system identification will then be provided before concluding with a discussion about the practical implementation of the pneumatic muscles and their challenges.

1.1 Neurorehabilitation and existing therapies

The impairment of brain functions caused by a damage to the central nervous system (CNS) has a significant impact on the daily life of the affected people[3]. From all the different causes affecting the motor control of one side of the body (hemiparesis), stroke remains, at the present time, one of the leading causes of permanent disability around the world. With a global prevalence of 101.5 million people in 2019 [1], it remains the most common neurological condition found in the health care system. The natural history of post-stroke symptoms implies physical, cognitive and psychological impairments that results in mobility problems, communication disorders, difficulties in swallowing and emotional difficulties. About 80% of stroke survivors have upper limb sensorimotor deficiencies early after stroke, and only 5% to 20% of them demonstrate a full functional recovery of the arm. Among the survivors, 30 to 60% remain with minimal arm functioning beyond six month post-stroke [5].

A stroke can be caused either by a blood clot obstructing the blood flow to areas of the brain (ischemic stroke) or by vessel rupture (hemorrhagic stroke). The consequence of this blood flow reduction is a reduced oxygen supply causing brain cells to starve to death. This is designated as the acute phase of the stroke and occurs in the first hours post-stroke. Then, days to months after, the chronic phase starts with the regenerative process [6].

The acute phase treatments consist in restoring the blood flow as quickly as possible to stop the neuron starvation and minimize their death. Depending on the type of stroke, a thrombolytic treatment to dissolve the clot or a surgery to reconstruct the broken vessel will be done. The major goal of this first phase is to save as many brain cells as possible.

The chronic phase aims to help the patient to recover his motor functions. Therefore, the neurorehabilitation process starts.

Neurorehabilitation is a clinical subspecialty devoted to the restoration and maximization of functions that have been lost due to impairments caused by injury or disease of the nervous system [7].

This process helps to accelerate recovery of daily life abilities, reduce the symptoms and improve the patient well-being. To enhance the results of the rehabilitation, neuroplasticity has to be exploited to its fullest.

Neuroplasticity is the ability of the nervous system to change its activity in response to intrinsic or extrinsic stimuli by reorganizing its structure, functions, or connections [8].

Physical exercise stimulates the reconstruction of connections between neurons by means of this neuroplasticity. With an appropriate rehabilitation plan, adapted along the recovery process, the therapist tries to exploit the brain's ability to learn and therefore strengthen circuits or create new ones to recover as many functions as possible.

Nowadays, studies conducted in clinical environments aim at identifying a set of principles that should guide the design of post-stroke rehabilitation protocols. In [9], the authors have identified a set of principles based on existing work on motor learning and recovery. These principles consist in repetitive practice, spaced practice, dosage (duration of the therapy process), task-oriented practice, task-specific practice, variable practice, multi-sensory stimulation, variable and increasing difficulty, explicit or implicit feedback and promotion of the use of the affected limb. It seems that many of those are poorly operationalized and combined in clinical trials. The conclusion drawn from this research showed that some principles modulate specific brain areas within the motor areas of the cortex while other rely on networks of brain regions. The rehabilitation programs should thus focus on incorporating principles of both types to limit neuronal degradation and promote improvement.

To this aim, it is clear that the set of identified principles which dictates the quality of rehabilitation carried out today by various medical professionals, could be progressively incorporated by robot-assisted therapies. Physicians, rehabilitation nurses, physical therapists and others could be relieved and helped by robots to enhance the post-stroke recovery, freeing up time for tasks that require more of their expertise and skills.

1.2 Assisted therapy robots

In the last decades, rehabilitation robots have been proposed for improving treatment outcomes[3]. By assisting in complicated, diverse, long-time training, they help reducing therapists' workload and healthcare costs. The history of rehabilitation robotics, even if all sources do not agree on the same project, has slowly started in the 1960's. Projects like the Case Western University Arm, the Rancho Los Amigos Golden Arm and other Powered Human Exoskeleton researches have paved the way for what became known as upper limb rehabilitation robotics today [10] [11]. Current upper limb rehabilitation robots can be divided into two classes: exoskeletons and end-effector-base robots. They can also be classified into electric, pneumatic, hydraulic or non-driven, with respect to their actuation principle, or with respect to their control strategies, such as PID, fuzzy, neural networks, adaptive and sliding mode control [12].

The **exoskeleton** robots are connected to the patient at multiple points and the implementation of their joints is such that their axes match with the human joint axes. The work done in [12] lists some classic exoskeletons for upper limb rehabilitation and classifies them based on DoF, supported movements, control inputs and actuators. The *ULEL* exoskeleton (Fig. 1.1a) is a 3 DoFs robot developed in France (2017). It is cable driven with electric motors using sliding mode control. The *RETRAINER* (Fig. 1.1b) is a device developed in the UK (2017). The system consists of a passive 4 DoFs exoskeleton with springs to provide gravity compensation and electromagnetic brakes to hold target positions. The *ArmeoPower* robot (Fig. 1.1c) is more complete with its 6 DoFs and was launched in Switzerland (2015). Those three exoskeletons offer an adapted training according to the subject progress and evolving abilities. Assistance can be adapted depending on the patient's needs and the rehabilitation phase in order to motivate the assisted person to actively participate to the therapy.

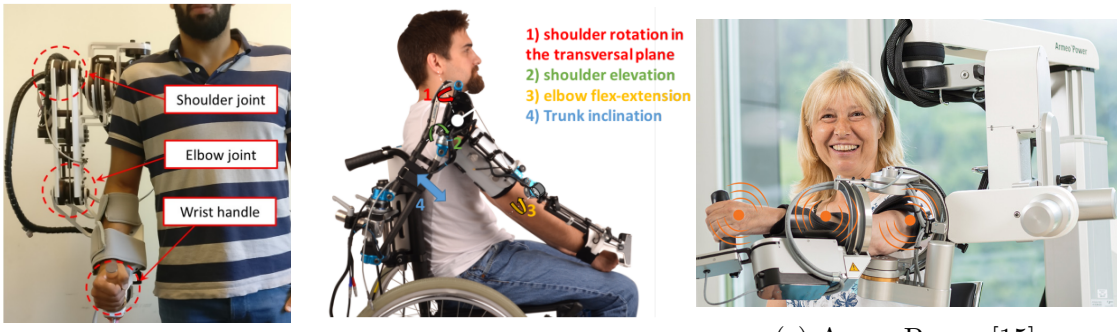

(a) ULEL [13] (b) RETRAINER [14] (c) ArmeoPower [15]

Figure 1.1: Three types of motorised (ULEL, ArmeoPower) or spring actuated (RETRAINER) exoskeleton

While those robots rely on electrical motorisation or springs to control the training, it is also possible to find ones that are pneumatically actuated. The *RUPERT* (Fig. 1.2a) has five DoFs driven by compliant pneumatic muscle actuators (PMA) to assist the movement of the arm (USA, 2008) while the *PNEU-WREX* (Fig. 1.2b) is a four DoFs robot actuated by pneumatic cylinders (USA, 2005).

(a) RUPERT [16] (b) PNEU-WREX [17]

Figure 1.2: Two types of pneumatically actuated exoskeleton

The **end-effector** robots are connected to the patient at one distal point and the implementation of their joints is such that their axes do not specifically match with the human joints. Some examples of implementations with diverse principles of actuation are available. The *REAplan* robot (Fig. 1.3a) developed by the Belgian company Axinesis (founded in 2015) consists in a height-adjustable table on which a Cartesian robot actuated by electric motors guides the patient during the therapy along with animations on a screen and sound provided by speakers. This allows the control of two DoFs. The *WAM* robot (Fig. 1.3b) is a 7 DoFs whole-arm manipulator (Korea, 2015). The forearm is attached at the distal position of the robot to manipulate the patient's arm in the 3D space. The interaction is encouraged via interactive games presented on a screen.

Another concept is the *Motore and MOTORevolution* robot (Fig. 1.4a) developed in Italy (2008-2009 and 2020-current). It is a portable and mobile haptic device on wheels, characterized by the absence of links. The forearm is attached on top of the robot and it moves on a table providing a feedback via an interface on a screen.

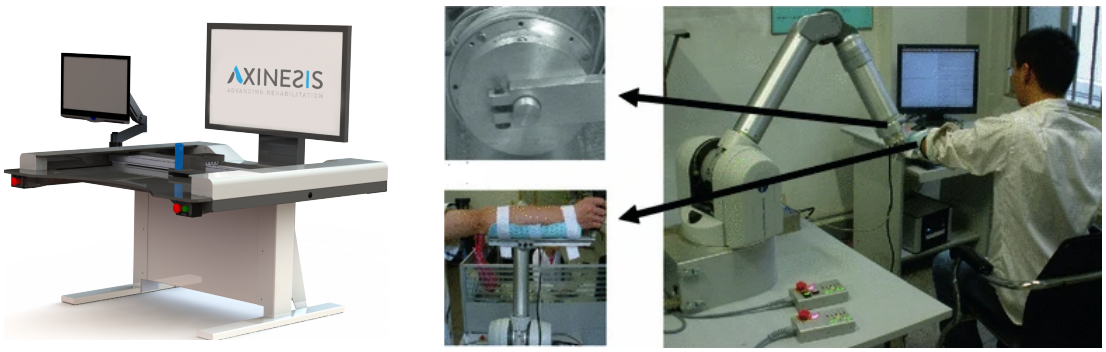

(a) REAplan [18] (b) WAM [19]

Figure 1.3: Types of end-effector rehabilitation robots

Other projects like the *EULRR* robot (Fig. 1.4b) are still under development (Shanghai, 2020-current). It consists in two 7 DoFs manipulators interacting with the patient arms via two handles. The robot can be moved and integrates a set of cameras to follow the movement and adjust the rehabilitation parameters. It aims to provide an interactive set of games via Virtual-Reality glasses.

(a) Motore [20]

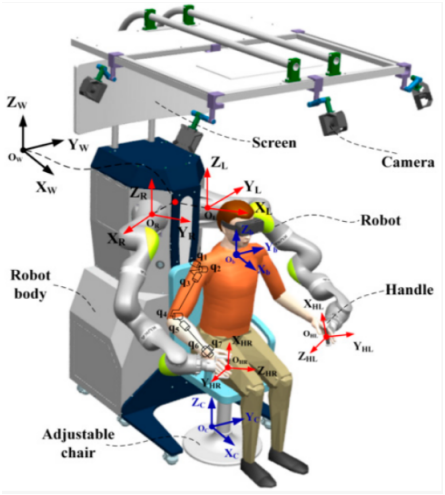

(b) EULRR [21]

Figure 1.4: Types of end-effector rehabilitation robots

The list of end-effector robots for rehabilitation presented here is not exhaustive. Various other designs, mostly actuated with electric motors, have been developed over the years. Again, the work done in [12] lists some projects of end-effector robots aiming to help with rehabilitation of the upper limb and classifies them based on number of DoFs, supported movements, control strategies and actuator types.

1.3 Pneumatic Artificial Muscles (PAMs)

1.3.1 Description

PAMs are contractile elements used to implement linear motion by means of injected pressure. The constitutive part is a flexible and reinforced membrane attached on one or both ends to the load. Those muscles will radially expand while axially contract when air is injected in the flexible membrane. This allows to exert an axial force on the attached load in a linear and unidirectional way. Since their first apparition in the 1930's, various artificial muscles have been developed and nowadays, two types of PAMs are the ones most frequently used: the Braided muscles and the Pleated Pneumatic muscles[22].

Braided muscles are composed of an inner elastic tube covered/surrounded by a braided sleeve. The fibers of the braid run helically about the longitudinal direction and form a pantograph network (Fig. 1.5a). When the pressure is applied, the tube presses against the sleeve causing the pantograph structure to elongate and shorten in the circumferential and longitudinal directions, respectively. This causes the angle between the fibers (braid angle θ) to increase and a force is applied at the extremities as the muscle contracts (Fig. 1.5b). The most common braided muscle structure is the *McKibben Artificial muscle* having both its tube and sleeve connected at both ends to fittings.

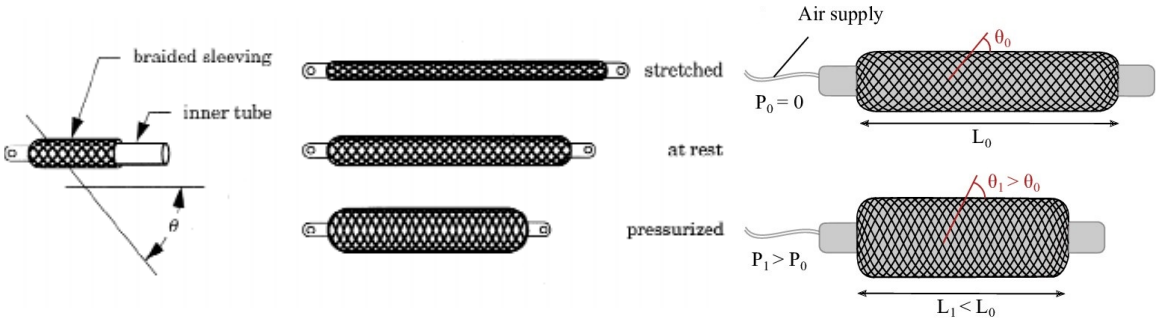

(a) Braided muscle, McKibben muscle [22]

(b) Actuation principle [23]

Figure 1.5: Braided muscle and its actuation principle

The Pleated PAM design has been developed by Daerden [24] in order to improve the performances of PAM with respect to the braided structure. The major drawbacks of the McKibben muscle are its inherent dry friction and threshold pressure, which make accurate position control harder to achieve. Other disadvantages are the limited displacement and the energy needed to deform the membrane. The pleated design solves this using a rearranging membrane so that no material strain is involved when inflated. A number of pleats in the axial direction (Fig. 1.6) will unfold when the membrane is expanding, keeping the stresses in the parallel direction negligible. Therefore, the amount of energy required to expand the membrane, and thus contract the muscle, remains low.

(a) Pleated muslce stretched and inflated [22]

(b) Actuation principle [24]

Figure 1.6: Pleated muscle in 3 inflated states

Another widely used type of muscles are the *Festo Fluidic Muscle DMSP* (Fig. 1.7a). They consist of contractible tubing made up of a rubber diaphragm with a non-crimped fiber made of aramid yarns on the inside (Fig. 1.7b). The yarns serve as reinforcement and transmit power [25]. The principle behind those PAMs is thus similar to the McKibben design but with the fibers placed inside the diaphragm. This is the type of muscle that is implemented in the current version of the 2D Planar Scara robot of this thesis.

(a) Festo Fluidic Muscle DMSP [25]

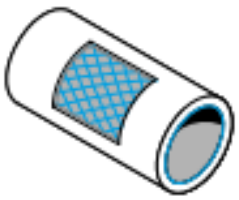

(b) Inner aramid yarns [25]

Figure 1.7: Festo Fluidic Muscle DMSP and their design

The pneumatic artificial muscles above-mentioned behave like a spiral spring and have a natural stiffness[1]. They confer a passive compliance[2] or *natural compliance* [26] to the robot which depends on the materials and manufacturing principle used to form the muscle actuator. Due to their natural damped spring nature, they provide a behavior analogous to the one of skeletal human muscles.

A principle followed by the PAMs which relates the rendered impedance at the end-effector with the one of the human arm is the following : if a robot-arm - kinematically analogous to the human arm - is powered by actuators - whose stiffness is similar to that of the human joints - then the compliance at the end of the robot-arm will match that of the human arm [27].

In summary, as previously mentioned, one of the McKibben artificial muscle limitation is the non-linear kinetic friction induced by the braided shell [26]. The dry friction occurring causes torque disruption and alters the accurate position control when the speed increases. However, this friction also results in a natural compliance that reproduces the softness of human joints. Other designs of muscles like the pleated muscle help mitigate those effects but McKibben muscles are still commonly used with some compromise with respect to the friction.

1.3.2 Control, Torque and Joint Range

The control of PAMs is essential to correctly impose the desired behavior (force, elongation, stiffness). Each PAM is usually interfaced with an electrical system composed of intensity to pressure (I/P) converters that manage the inflation and deflation of the muscles with respect to a feedback provided by multiple sensors and a command sent by the controller. When assembled in an agonist-antagonist configuration, PAMs allow to develop torques around revolute joints. In this case, they are usually linked to pulleys through cables or chains (Fig. 1.8). Using various sets of pressure P_1 and P_2, adjustable position, torque and stiffness can be achieved. This will depend on the control strategy implemented.

[1] *Stiffness* characterizes the resistance of an elastic body to an applied deformation
[2] *Compliance* is the ability to adapt to an external disturbance

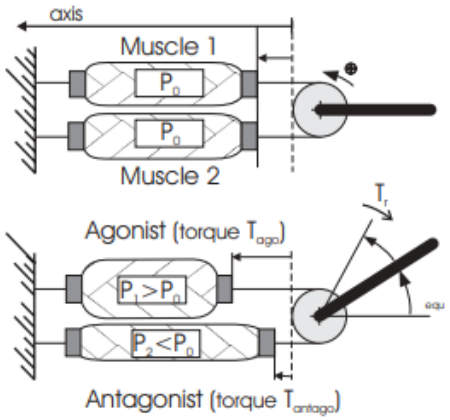

Figure 1.8: Antagonistic McKibben muscle actuator: functioning principle [27]

In the literature, various models have been developed to express the force produced by artificial pneumatic muscles. Depending on the type of those pneumatic actuators, corresponding representations exist. Nevertheless, the latter usually depends on the elongation/contraction ratio ε and the injected pressure P so that $F(\varepsilon, P)$. A mathematical expression of the force for McKibben artificial muscle is available in [22], [26] and [27]. For pleated artificial muscle, force expressions were developed in [22] and [24]. For the Festo Fluidic Muscle DMSP, the model identified in a previous master thesis, that also had the robot studied here as subject, will be used [4].

The torque developed at the joint presented in figure 1.8 is[26]

$$\tau = R \cdot (F_{Muscle,2}(\varepsilon_2, P_2) - F_{Muscle,1}(\varepsilon_1, P_1)) \ [Nm] \tag{1.1}$$

and the actuator joint range is

$$\theta_{min,max} = \left[-\frac{\Delta\varepsilon_{max} l_0}{R}; +\frac{\Delta\varepsilon_{max} l_0}{R} \right] \ [rad] \tag{1.2}$$

where R is the pulley radius, $\Delta\varepsilon_{max}$ is the maximum variation of the contraction ratio of the muscles with respect to the initial contraction ratio ε_0, ε_i is the current contraction ratio of each muscle, P_i are the two muscle pressures and l_0 is the initial length of the muscle.

The design choices have some impact on the abilities of the robot in terms of the joint torque and angular range. The impact of the radius of the pulley can be seen in the two equations above: an increase of R allow to develop higher torques but limits the joint range to lower values. A compromise must be found for this parameter as well as for the initial length of the McKibben muscles l_0. The latter allows to achieve higher range of motion when increased but makes the robot considerably bigger.

1.4 Open loop system identification

Several techniques can be used to perform system identification, depending on the type of system as well as the goal of the identification. For example, if it is done

in order to better understand the system, the objective will be obtaining a model based on physical principles. If a simple parametrization of the behavior is desired, the mathematical model does not necessarily correspond to physical characteristics. The results of this identification can also be used to design and improve closed-loop controllers.

In the context of human movement, a variety of skillful movements that can be performed is noted, as well as an ability to adjust the dynamic characteristics of the musculoskeletal system depending on the task to be performed. Therefore, interest in the describing the human arm dynamics has grown during the last decade. To this aim, elementary models are usually used to try to identify the impedance of the arm. One of the possibilities being the most frequently used is the spring-damper-mass system (denoted here KBM model), also named stiffness damping and inertia model.

The KBM model is used as a linearization for small deviations around an equilibrium point and is convenient as it has been demonstrated to approach and describe the human behaviour (for the arm or leg) with high degree of accuracy[28] [29]. Depending on the application, the identification of the model will be done in the joint or Cartesian (end-effector or reference) space. The governing equation is the following

$$M\ddot{\mathbf{x}} + B\dot{\mathbf{x}} + K(\mathbf{x} - \mathbf{x}_0) = F$$

where x is a vector representing the displacement of a multi-body system of mass described in the matrix M, subject to spring forces characterized by spring constant in a matrix K and damping forces resisting to the change of motion characterized by damping coefficient in a matrix B. F represents the applied force on the system.

Many studies on human arm mechanical impedance (i.e. stiffness, damping and inertia) have been performed over the years. In [29], the authors identified the mass-spring-damper matrices of the human arm using a two-joint muscle model in the horizontal plane in order to investigate the relationship between these components and the posture of the arm. Results in terms of an elliptical representation for the human arm mass, damping and stiffness in the Cartesian plan are presented in figure 1.9. Other works focus on more complete modelling and identification as in [30] where a systematic method for characterizing the arm impedance in the 3D space is presented. In [28], the authors identified human hand impedance during the different phases of a ball-catching task. Those results in term of hand inertia, viscosity and stiffness are synthesized in table 1.1.

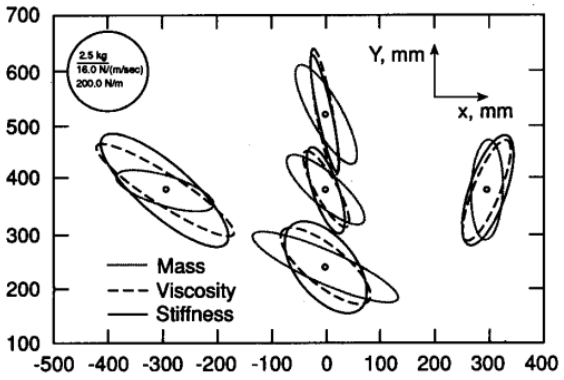

Figure 1.9: Mass, damping and stiffness ellipses of human subject based on a KBM model of a simple two-joint muscle model in 2D [29]

Table 1.1: Measured human hand impedance during a ball-catching task synthesized from [28]

	K_e (N/m)	B_e (N s/m)	M_e (kg)
Stable posture	67.04	20.56	1.36
Before motion	102.02	23.02	1.40
Task-readiness	115.65	23.04	1.43
After motion	113.35	16.93	1.18

Since in recent years the interest in rehabilitation and rehabilitation robots has become a matter of great concern, the analysis of robotic devices, robotic arm and others has seen great advances. Therefore, the representation using the mass-spring-damper model has extended to robotics in a bio-mimetic way in order to have proper models for the robot dynamics and to be able to develop pure or hybrid impedance controllers for rehabilitation purposes. In [19], the impedance identification and adaptive control of an upper-limb rehabilitation robot is investigated. They identify the KBM models of the human arm and the robot and verify the effectiveness of an adaptive PI-damp controller of the WAM robot presented previously (Fig. 1.3b).

Other works focus on pneumatic artificial muscles actuated robots for rehabilitation. This is the case in [31] where a robot similar to the one studied in this thesis is analysed. The robot is presented in figure 1.10a and the author managed to implement a control scheme based only on a spring-damper model. In [32], the two-link soft robot arm presented in figure 1.10b is also actuated with pneumatic muscles. The study presents a complete dynamic characterisation that could be used to control the device. In this case, the identification was obtained by means of PAM and arm dynamics simulation via software, such as *Matlab*® *Simulink*[33]. Validations of the obtained models for the PAM and arm a posteriori have shown that the model offered good performances.

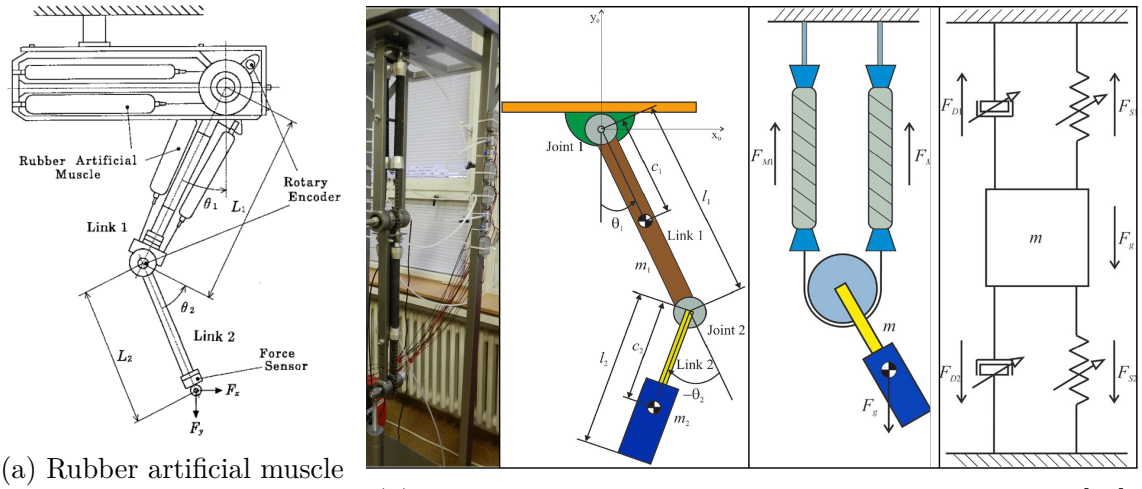

(a) Rubber artificial muscle manipulator [31]

(b) Planar robotic arm with PAM and its KBM model [32]

Figure 1.10: Two PAM actuated robotic arm identified with KBM models

1.5 PAMs in practice

When consulting the literature about upper-limb rehabilitation robots, it is noteworthy that the robots actuated by electrical motors have taken the lead over the pneumatically actuated robots. Among the pneumatic robots that have emerged, only a few have been marketed or are used for regular clinical treatments. Besides, the majority remains in the prototype state.

While trying to understand the reasons why those new types of robots commonly remain in the research domain and do not spread over the market, multiple authors have compared the pneumatic actuation principle to the conventional ones in order to draw out their advantages and disadvantages. Industrial robots are known to be powerful and accurate but their structure and motorization principle (electric motor for most of them) makes them heavy and highly rigid. Humans, however, have arms that are light and not very accurate, with a natural joint flexibility. Thus, if it is expected that the workspace will be shared between both, a reorientation towards robots showing the same characteristics than humans should appear [26].

It is clear that multi-joint robots are necessary for rehabilitation as well as strategies combining rhythmic and discrete primitive movement to be able to stimulate a larger set of cortical areas and ensure an in depth recovery. Motivation is one of the pillars of rehabilitation, therefore special attention must be given to the development of adapted and progressive assisted tasks. With an adaptive strategy focusing on the achieved performances to regulate the impedance of the robot, the provided guidance can be set to an appropriate level.

In an effort to identify the benefits of the pneumatic systems, the authors of [34] have listed various elements. They mention the compactness, as well as higher payload to weight or power to weight ratio offered in comparison with classical

actuated robots. The compliance avoids the conventional rigidity of the electric motorisation. Pneumatic artificial muscles offer natural compliance due to their analogy to skeletal muscles and, when combined with force sensors, they allow to produce efforts in a safe and comfortable way. They also mention the possibility of offering a relatively low-cost solution for simpler applications that do not ask for high precision or high dynamic performance.

However, even considering those advantages, previous works have shown the multiples drawbacks that confine this technology to the research stage. In [4], the author evokes the complexity of using such technologies due to non-trivial control. Another point that is problematic is the lifetime of muscles with respect to the one of electrical motors. Due to stress concentration at the junctions, the longevity is limited. The deformation achievable with the PAMs remains bellow 35% of their initial length which thus limits the range of operation of the device implementing these actuators. Last but not least, the comfort of the impaired patient during the process of recovery can be affected by the noticeable noise produced, given the need for an air exhaust.

The authors of [34] have presented a table of comparison of actuators shown in figure 1.11. As mentioned in [32]: "Use of soft actuators in robotics can be considered for machines, which position within the industry should not be viewed as replacing (for the current robots) but rather complementary". Some complete devices with great prospects have been created as for the *RUPERT* or *PNEU-WREX* exoskeleton as well as the *Rubber artificial muscle manipulator* presented earlier but they only paved the way for future projects involving pneumatic artificial muscles.

Table 1. Comparison of actuators.

Actuator	Advantages	Disadvantages
Pneumatics	Cheap, quick reponse time, simple "bang-bang" control.	Position control difficult, fluid compressible, noisy.
Hydraulics	High power/weight ratio, low backlash, very strong, direct drive possible.	Less reliable, expensive, servo control complex, noisy.
Electrics	Accurate position and velocity control, quiet, relatively cheap.	Low power and torque/weight ratios, possible sparking.

Figure 1.11: Comparison of actuators (pneumatics, hydraulics, electrics) [34]

1.6 Summary

As stroke is a medical condition affecting globally more than 100 million people per year and causing impairment of brain functions related to physical, psychological and social abilities of the victim, the development of efficient techniques for treatment is necessary. The latter must be carried out early in the rehabilitation process and aim to be patient specific, intensive, task-oriented and repetitive. For that purpose, robots have made their appearance in the field of rehabilitation to improve the

therapies and relieve the medical staff.

During the last decades, rehabilitation robots of various forms have appeared. They are classified in two categories: exoskeleton or end-effector robot and vary with respect to their principle of actuation. Among those, the pneumatic artificial muscle actuators are becoming increasingly investigated. They consist in an elastic membrane, which constitute a contractile element, used to implement linear motion by means of injected pressure. However, when assembled in an agonist-antagonist configuration, they allow to develop torques and adjustable joint stiffness.

In an effort to develop controllers to regulate the robot behaviour, mainly in terms of the perceived end-effector impedance, methodologies to characterize robotic arms have been used. Those methods are usually the ones used to describe the human arm dynamics and consist in a mass-spring-damper system identification. The literature concerning this identification is plentiful for the human arm but remains scarce for the pneumatically actuated robotic arms characterization.

The major advantages of the two-link planar robot actuated by pneumatic artificial muscles are their intrinsic compliance, high power to weight ratio and their low cost. On the other hand, they are still rather imprecise, even if controlled in closed-loop, and noisy but this does not justify why they remain scarce or are not marketed in the medical world. Based on this observation, the subject of this master thesis will be the continuation of the development of a prototype robot driven by pneumatic artificial muscles with the aim to help in post-stroke upper-limb rehabilitation. The following chapter will focus on the description of the robot along with the mechanical redesign carried out to improve the new version with respect to the previous one.

Chapter 2

Description of the robot and Mechanical Redesign

This chapter introduces the robot as a whole, describes in more detail its main elements and presents the mechanical redesign which has been carried out. The initial position as well as the different reference frames are defined. The agonist-antagonist pneumatic muscle principle of actuation is explained. Finally, some notations used in the following chapters are also defined.

2.1 A global overview of the system

The 3D CAD design of the robot presented in figure 2.1 is a SCARA robotic arm. The device is inspired by the behavior of the human arm and implements 2 DoFs: *flexion-extension* of the shoulder and elbow. The rotation of the two joints is made possible as a result of a system of cables and pulleys, actuated by 4 pneumatic artificial muscles (two pairs of *agonist-antagonist* muscles).

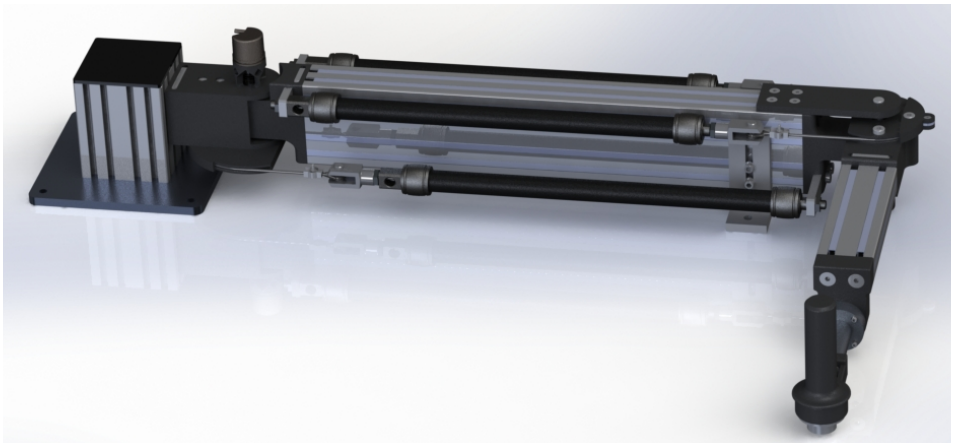

Figure 2.1: 3D CAD design of the robot [4]

The robot arm itself is part of an integrated electro-mechanical system and the links between the different entities are shown in figure 2.2. The software *LabView*

is used to interface the robot and its electronics, providing an interface with the user, that can then control, setup and program the robot. The current commands computed (for each muscle) are then converted into pressures by Intensity/Pressure converters and they output compressed air - at the desired pressure - that supplies the robot. These selected pressures are sent to the four respective muscles, which inflate, and this activation of the muscles allows the robot to move. Regarding instrumentation, in order to obtain a feedback in position and force, two angular (encoders) and one force sensor are used to return information about the current state of the system to the LabView program for control purposes. The link between the software and the hardware parts is established by a CompactRio (embedded controller manufactured by National Instrument).

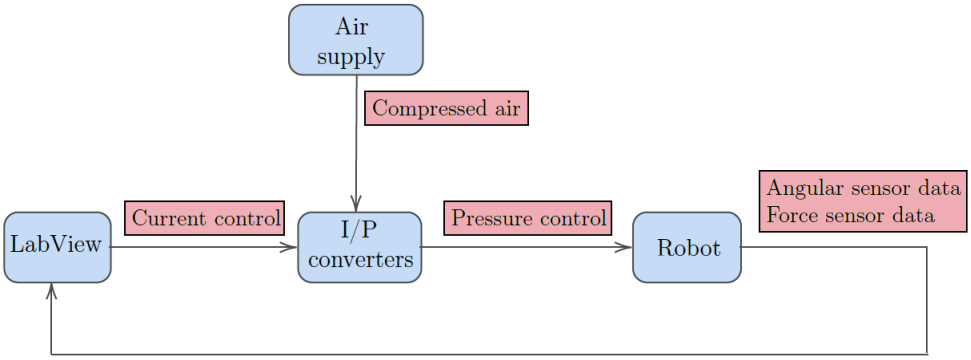

Figure 2.2: Block diagram of system operation [4]

The Frame and segments

The link between the robotic arm and the table is made via a rigid support, which is bolted (Fig. 2.3). This defines the position of the reference frame of the whole device. The segments analogous to the human arm and forearm are made of aluminium extrusions to be rigid and to limit bending (Fig. 2.4). They are rectangular, hollow to limit the weight and contain slots that can be used to hide the cables or attach additional parts. The respective lengths of segments one and two are $L_1 = 700$mm and $L_2 = 450$mm. The four pneumatic artificial muscles are attached along the first segment (human arm equivalent) to produce the desired forces.

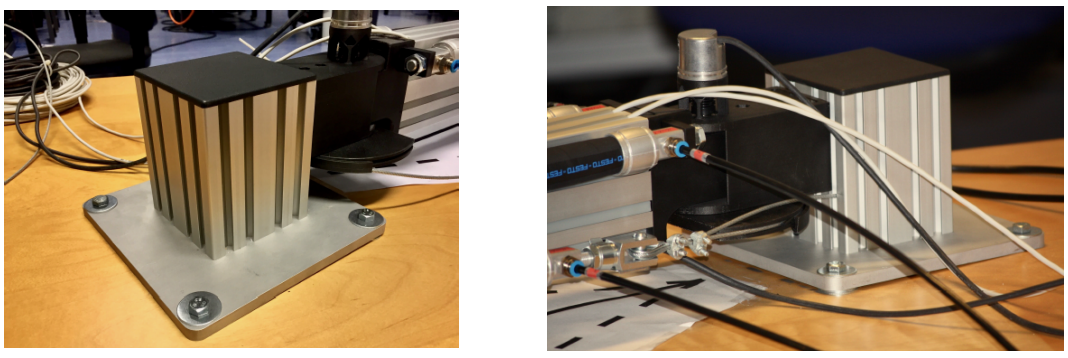

Figure 2.3: The frame [4]

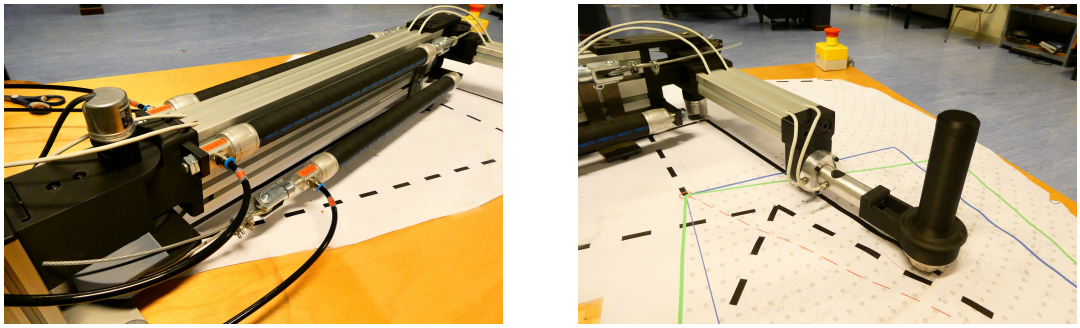

(a) Segment 1 (b) Segment 2

Figure 2.4: The segments

The Joints

Two joints connect the solid segments together and allow rotation around two vertical axis (shoulder and elbow, Fig. 2.5). Two pulleys ensure a conversion of the developed forces into torques and help to stiffen the system via the co-contraction of the *agonist-antagonist* pair of muscles. These parts are 3D printed using Onyx and Kevlar fibers for reinforcement and are attached to the joints via through-bolts. The pulley diameters for joints one and two are respectively $D_1 = 140$mm and $D_2 = 90$mm. Next to this, the joints allow an angular range of $\Delta\alpha_1 = 45°$ and $\Delta\alpha_2 = 65°$. The original design used until the beginning of this thesis presented some mechanical limitations and asked for improvement/redesign.

Figure 2.5: The joints [4]

First, new socket screws are used to avoid screw-head imprint destruction when applying tightening torque. Their increased head thickness and hexagonal socket cap size ensure resistance to tightening. Secondly, the part at the end of the first arm (human arm), responsible for linking the rest of the second joint and second arm (human forearm), was bending when significant tension was applied to the cables, which was the case when high stiffness was desired. To solve this problem, the shaft ensuring the connection of the different parts has been elongated and a second plain bearing has been added above the pulley thanks to a new part that is fixed to the first arm (Fig. 2.6). This helps to take up the bending moments occurring in the

connecting beam. As it can be observed in figure 2.7, the impact of the new part is significant and solves the issue.

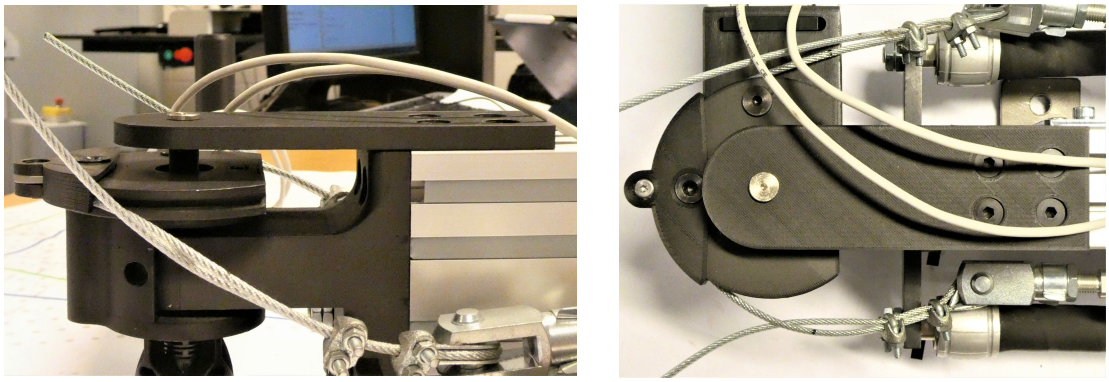

Figure 2.6: The reinforcement part

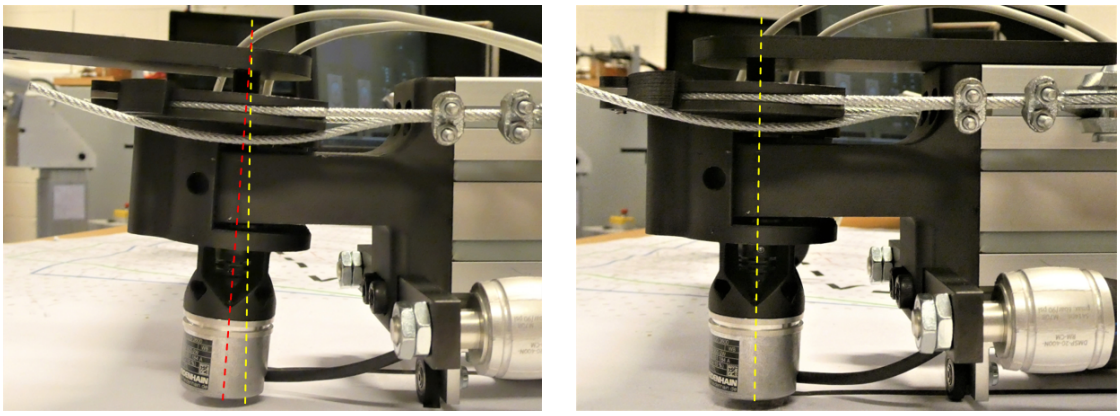

(a) Before (b) After

Figure 2.7: Effect of the new design

The Handle

The interaction between the patient and the robot is performed using a handle (Fig. 2.8a). The handle is orthogonal to the 2D working area and rotates freely around its axis. The part has been 3D printed in Onyx and is fixed at the end of the force sensor. The whole system rests on a carrier ball (Fig. 2.8b) ensuring free motion in all possible directions (2D). This also limits the contact with the table to a single point, therefore limiting friction.

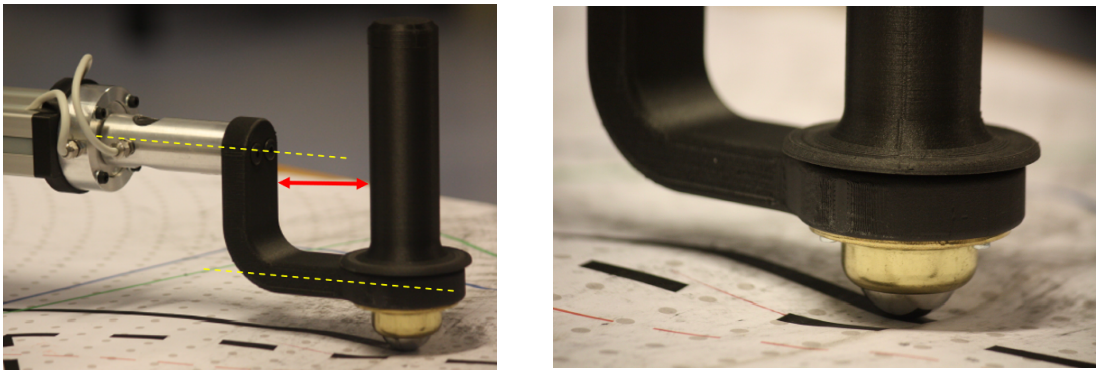

(a) Handle (b) Carrier ball

Figure 2.8: The handle and its carrier ball [4]

The original design of the interaction block also showed some weaknesses that needed to be improved. First, the anchor point between the handle and the force sensor was lowered. This change was originally designed to enlarge the space around the handle because, with the original part, the back of the patient's hand was touching the sensor in some configurations. The patient can now sweep the entire angular range of the work-space without touching the attachment with the sensor (Fig. 2.9a). Moreover, the new design is no longer "L" shaped. This limits the lever effects when applying a force on the handle and decreases the difference between the force sensed and the one effectively applied. Next to this, reinforcement has been added to the bottom part of the handle support to reduce bending under loading. The second change on this part is the new carrier ball. The original one was blocking at times because it was designed to be placed with the ball upwards (but here used with the ball downwards). Therefore, a new one, more adapted to have its ball downwards, was mounted (Fig. 2.9b).

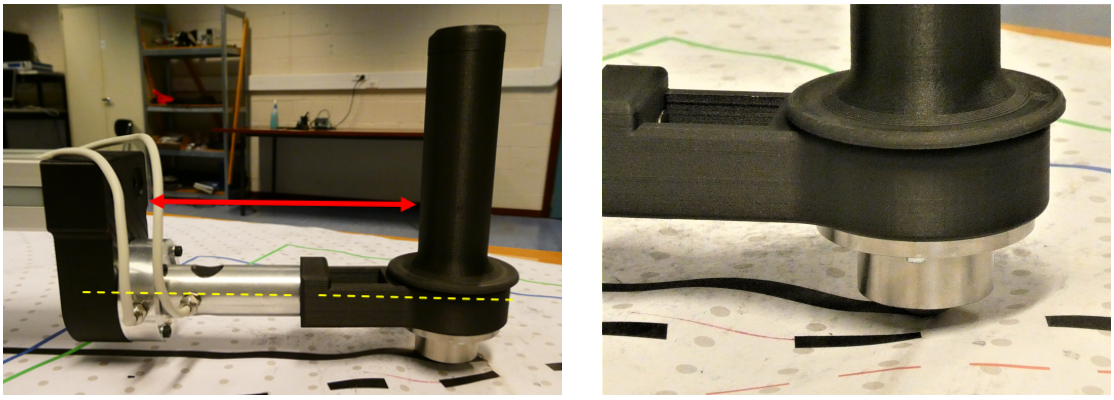

(a) New handle configuration (b) Carrier ball

Figure 2.9: The new handle configuration and its new carrier ball

The Cables

The connection between the two muscles of a joint is made by means of metal cables running through the pulleys (Fig. 2.10). They are fixed with cable ties and

steel thimbles. Originally, the only way to avoid a relative motion between the cable and the pulley was the use of a 3D printed cable-compressing cover, tightened by two screws (in addition to the friction involved). However, this did not prevent the cable from slipping, leading to a disruption of the mechanism during operation.

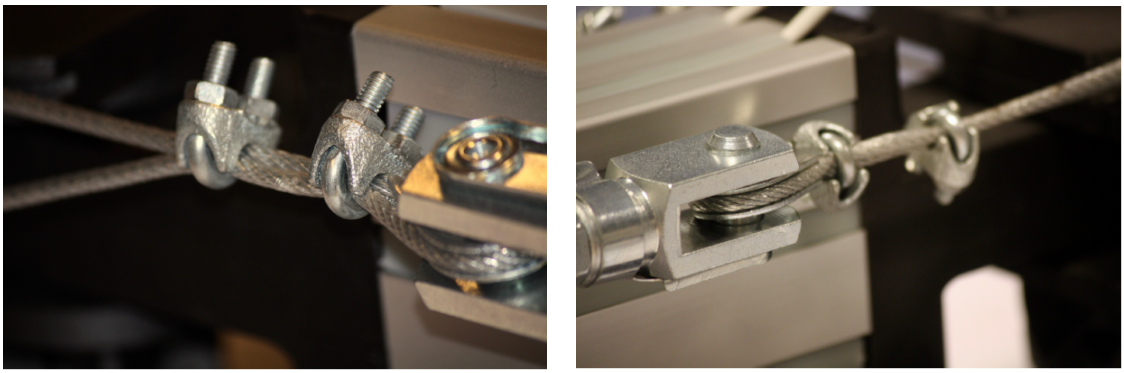

Figure 2.10: The cables [4]

The solution was provided by a grooved metal part (Fig. 2.11a and 2.12). This last is inserted between the Onyx cover and the cable and crushes the cable via the tightening of the screws (Fig. 2.11b). The grooves act as small teeth biting the cable to maintain it in place.

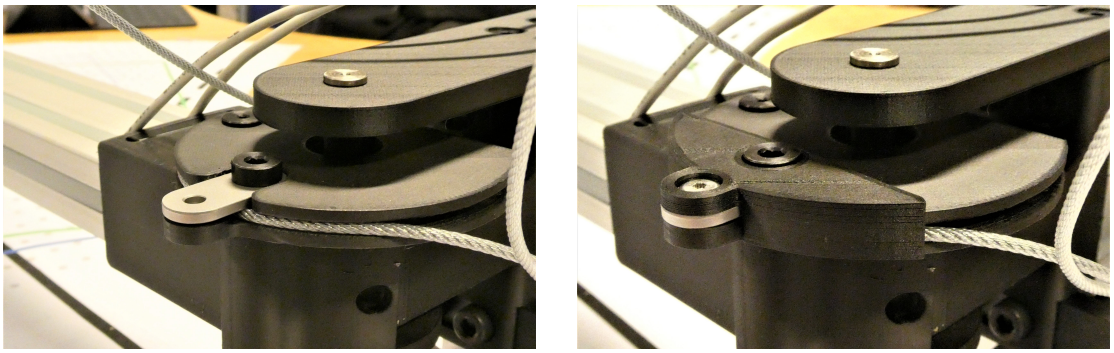

(a) Clamping part (b) Pulley cover

Figure 2.11: The clamping part and the Onyx cover to apply tightening

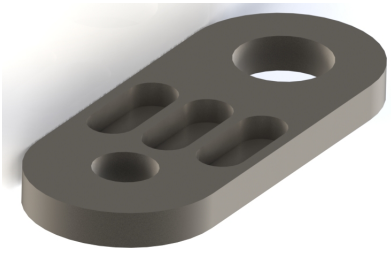

Figure 2.12: Clamping part CAD model (bottom view)

The Pneumatic Artificial Muscles

Four pneumatic artificial muscles are used to actuate the robot. They are fixed on the sides of the first segment and have an unloaded length (l_0) of 400 mm. Those muscles are the Festo Fluidic Muscles DMSP presented in section 1.3. They are supplied with compressed air from the Intensity/Pressure converters to induce their contraction.

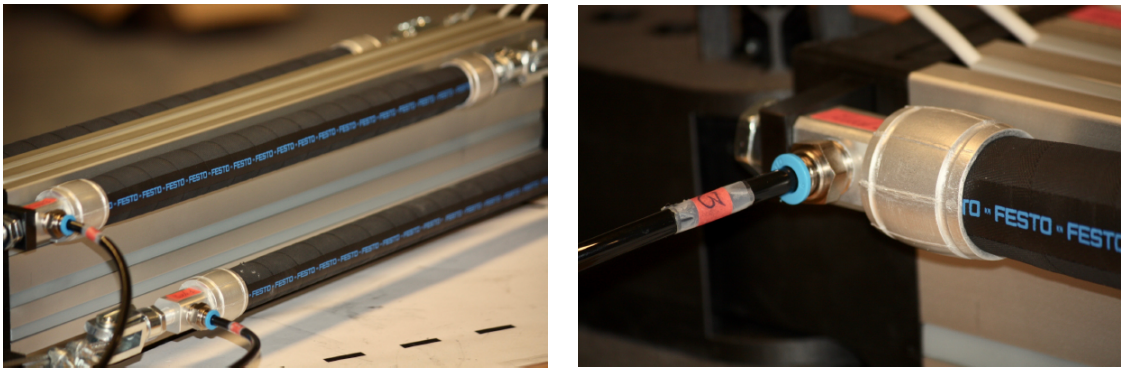

Figure 2.13: The pneumatic artificial muscles [4]

The 1^{st} joint/arm locking mechanism

For the sake of simplicity when experiments or rehabilitation tasks only require the second arm to move, a locking mechanism has been added. The part consists of an "L" shaped plate with an oblong hole on the longest face and a classic one on the smallest (Fig. 2.14). The first helps sliding the part up, to avoid contact with the table when in free configuration, and down, to lock the arm using a bolt and butterfly nut through the table.

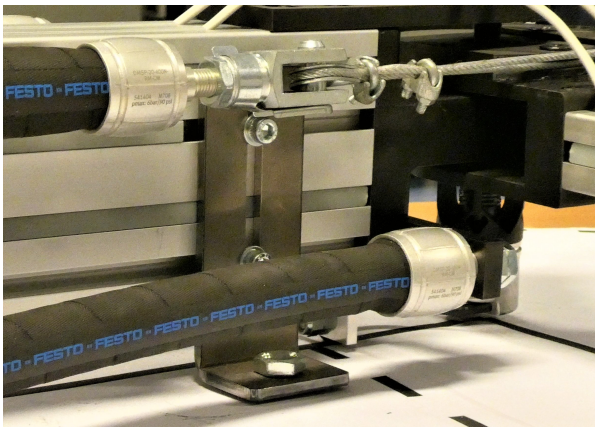

Figure 2.14: The 1^{st} joint/arm locking mechanism

The Sensors, Intensity/Pressure converters and CompactRIO

The angular sensors

To provide information from the robot about the angular position of its two arms, angular sensors are placed at each joint (Fig. 2.15). Placed on top of the first joint and above the second, they provide the angular variation from the initial position and thus track the movement of the arm and forearm. The second sensor was originally touching the table (Fig. 2.15b) due to the first arm and joint flexion under their weight but this has been solved by placing a supporting wheel under the first section at the distal position (Fig. 2.16).

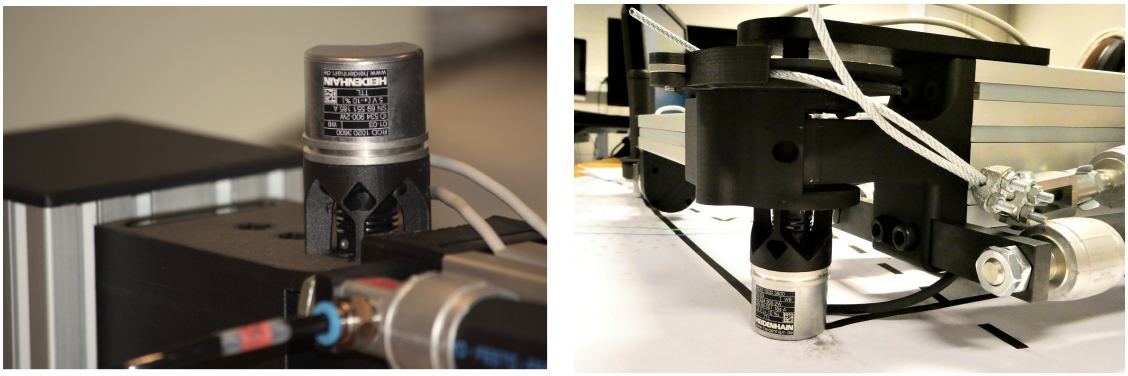

(a) Angular sensor joint 1 [4]

(b) Angular sensor joint 2 (before)

Figure 2.15: The two angular sensors

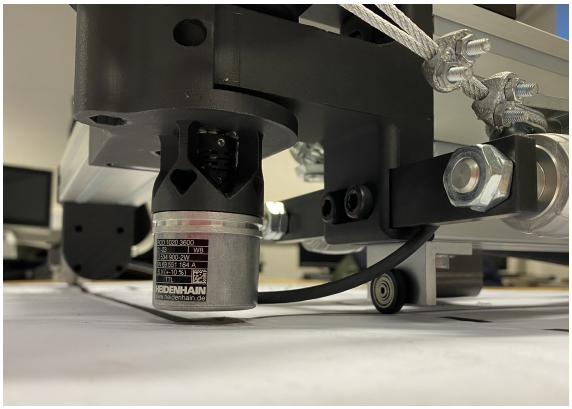

Figure 2.16: Angular sensor joint 2 (after)

The force sensor

To obtain the force resulting from the robot-user interaction, a bi-axial force sensor is mounted at the end of the forearm, before the handle (Fig. 2.17). The load rating along the X- and Z-axis is 20 kg and they are respectively defined along the length of the sensor and its radius. The anchor point between the sensor and the second arm has also been lowered in order to match the change in height of the anchor point between the sensor and the handle (Fig. 2.17a). The two force values are used as the

output of the system and the force-voltage relationships (X- and Z-axis, Fig. 2.17b) of the sensor have been established in previous work[4]. Those relationships are close to linear and have the following form:

$$\begin{cases} F_x\ [N] = \frac{1}{0.09} \cdot U_x\ [V] \\ F_z\ [N] = \frac{1}{0.06} \cdot U_z\ [V] \end{cases} \tag{2.1}$$

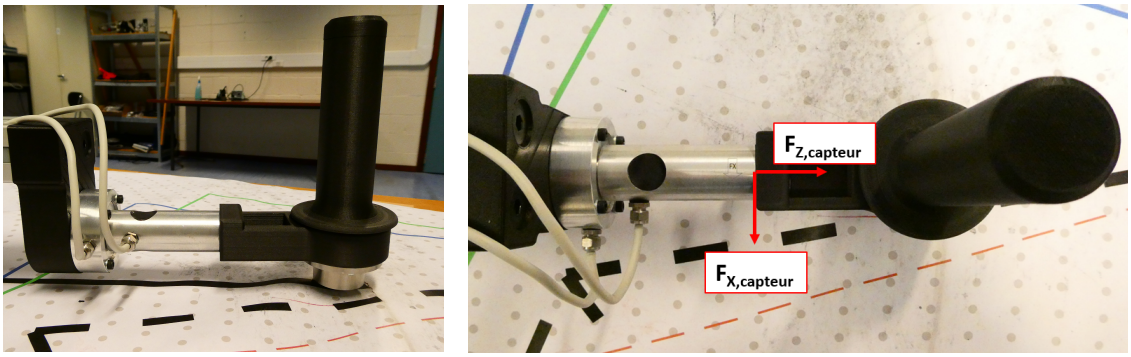

(a) Force sensor side view (b) Force sensor axis

Figure 2.17: The force sensor

The intensity/pressure (I/P) converters

The system has four I/P converters, responsible for converting, as their name indicates, the intensity (current) provided by the CompactRIO in miliAmpère into a pressure, sent to each muscles via plastic tubes (Fig. 2.18). They range from 0.4 to 20 mA and output from 0.1 to 5 bar, having a linear relationship between their input and output. The transfer function was presented in previous work[4], which also verified experimentally the linearity of this function. The I/P converters are thus reliable and the current-pressure transfer function has the following form:

$$P[bar] = 326.67 \cdot I[A] - 1.63 \tag{2.2}$$

Figure 2.18: The I/P converters and the pressure distributor [4]

The CompactRIO

" The CompactRIO is a device from the National Instrument industry that provides an industrial control and monitoring solution using sensor or protocol-specific packaged I/O modules with real-time capabilities (Fig. 2.19). It is used to realise the communication between the sensor data, the FPGA and the CPU. It is composed of different modules that respectively take care of reading or sending information through the system.

- Module 1 is the NI 9265. It is a 4-channel, 16-Bit analog current output module. It takes care of sending pressure commands from the software to the robot through the FPGA interface.
- Module 2 is the NI 9403. It is a 32-channel, TTL digital input/output module. It is used to receive information from the angular sensors.
- Module 3 is the NI 9215. It is a 4-channel, 16-Bit simultaneous analog input module. It is used to transmit the load cell information through the FPGA interface. " [4]

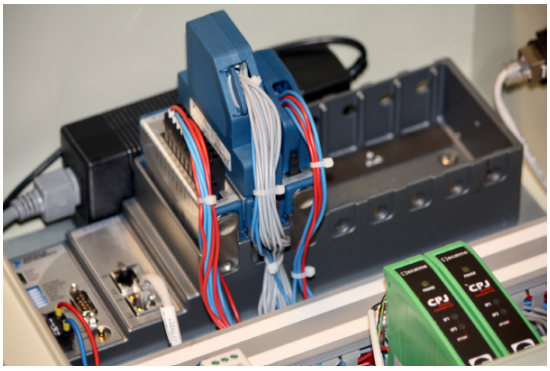

Figure 2.19: The CompactRio

2.2 Reference frame and initial position

To describe the behaviour of the robot in its workspace, some conventions and notations have to be defined as shown in figure 2.20. First, a reference frame (world "w") (x_{w0}, y_{w0})[1] (in red) is defined. This first is set according to the Denavit-Hartenberg (D-H) convention and allows to derive the Jacobian operator for the Scara robot in the planar configuration. The neutral position of the robot is shown in dashed-line, the θ angles respect the D-H convention to establish the robot kinematics. It must be noted that the neutral configuration of the robot is not aligned with the (x_{w0}, y_{w0}) frame. Thus, a second frame (rotated "r") (x_{r0}, y_{r0}) (in blue) is defined to be aligned with the first segment. With this, the α angles - measured by the encoders - represent the movement of the two segments (arm and forearm) away from their

[1]The 0 index indicates that the frame remains fixed in space and does not translate or rotate as the robot is moving

initial configuration. The two frames are separated by a rotation expressed with the α_0 angle.

$$\alpha_0 = \arctan\left(\frac{L_2}{L_1}\right) \tag{2.3}$$

where L_1 and L_2 are respectively the first and second segment length.

The relationships between the angles in the (x_{w0}, y_{w0}) and the (x_{r0}, y_{r0}) frames are

$$\begin{cases} \theta_1 = \theta_{1,init} + \alpha_1 \\ \theta_2 = \theta_{2,init} + \alpha_2 \end{cases} \tag{2.4}$$

with $\theta_{1,init} = 90° + \alpha_0$ and $\theta_{2,init} = -90°$ the initial angular position of the joints with respect to the D-H convention so that the first segment is aligned with y_{r0} and the second is parallel to x_{r0}.

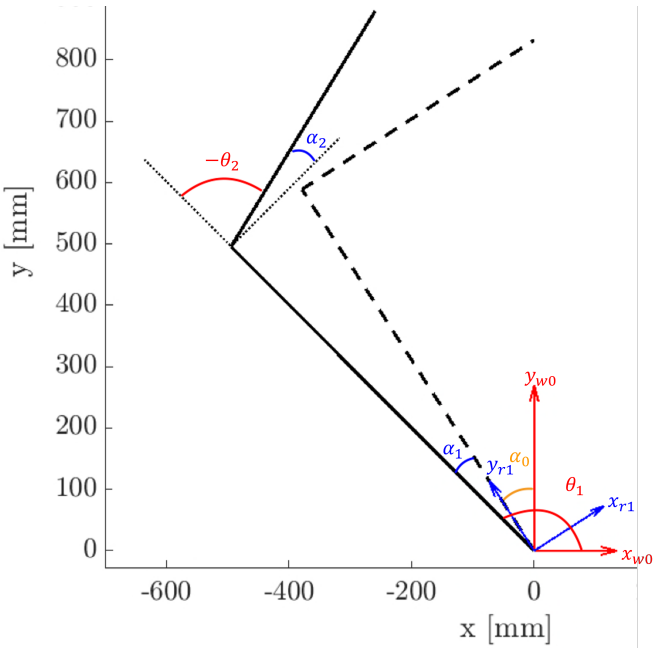

Figure 2.20: The robotic arm in its coordinate system

The angular range (orange dot-dashed-line, Fig. 2.21) around the initial configuration, measured by the incremental encoders is

$$\begin{cases} \alpha_1 = [-22.5°; 22.5°] \\ \alpha_2 = [-32.5°; 32.5°] \end{cases}$$

From the development in Appendix A, the expression for the Jacobian and the end-effector force in the reference frame can be obtained[2]

[2]For the following $C_{\theta_i} = cos(\theta_i)$, $S_{\theta_i} = cos(\theta_i)$, $C_{12} = cos(\theta_1 + \theta_2)$ and $S_{12} = sin(\theta_1 + \theta_2)$

$$J = \begin{pmatrix} -a_1 S_{\theta_1} - a_2 S_{12} & a_2 S_{12} \\ a_1 C_{\theta_1} + a_2 C_{12} & a_2 C_{12} \end{pmatrix} \quad (2.5) \qquad F_{x_{w0},y_{w0}} = {}^0R_2 \; F_{x_s,y_s} \quad (2.6)$$

$$ {}^0R_2 = \begin{pmatrix} C_{12} & -S_{12} \\ S_{12} & C_{12} \end{pmatrix} \quad (2.7)$$

where F_{x_s,y_s} denotes the force in the end-effector following the D-H convention.

The two presented frames, (x_{w0}, y_{w0}) and (x_{r0}, y_{r0}), help to define the problem as seen by roboticists. The first one serves as a basis to develop the D-H convention, to express the kinematics and dynamics. The second has been established to make the conversion between the measured angles α and the ones from the convention. However, seen from the workspace perspective, these two frames are not intuitive to the user (robot operator, clinician, patient), which means, for example, results are harder to interpret. Therefore, a workspace parallel to the table edges has been chosen (blue rectangle in Fig. 2.21) and a new frame (user "u"), to describe the positions, movements and forces, has been defined (in green). This last will be denoted by (x_{u0}, y_{u0}) and is centered at the position of the end-effector (handle) in the initial configuration of the robot (black dashed line, Fig. 2.21). The axes of the frame are parallel to the defined workspace. Unless otherwise specified, the results presented further in this thesis will be given in this last - working - frame.

The three frames defined are fixed in space (indicated by the "0" index in their notation), i.e. they do not rotate or translate as the robot is moving (black solid-line, Fig. 2.21). The central position of the user/workspace frame has been arbitrarily chosen to be at the end-effector neutral position. This could have been placed at the center of the workspace, in one of its corners or somewhere else, but placing it at this position seemed the more intuitive choice.

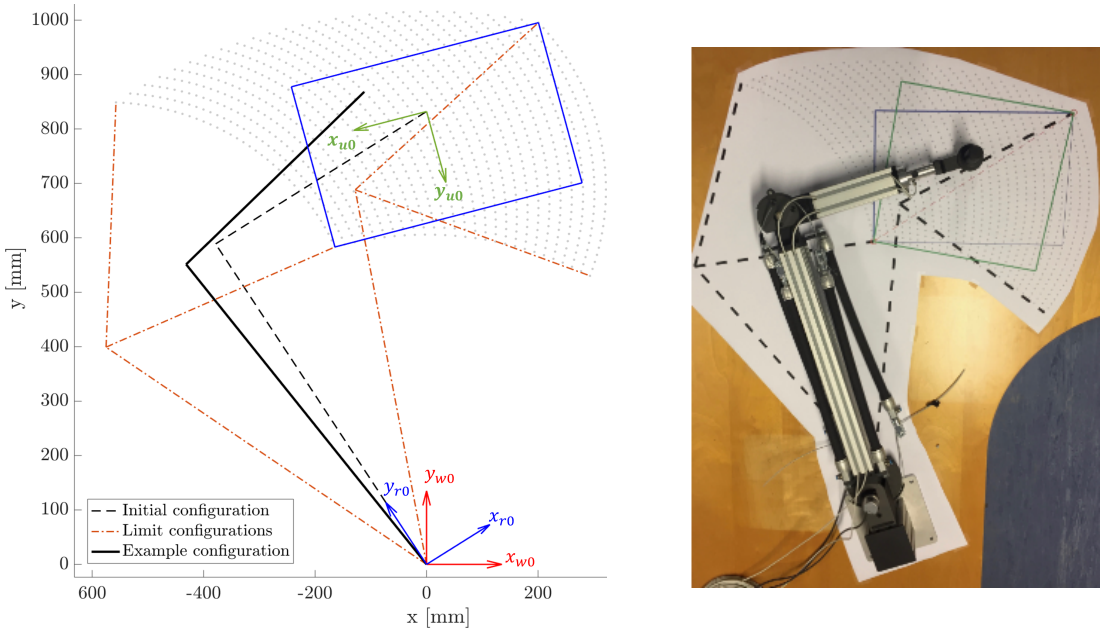

Figure 2.21: The three frames and the robot in its workspace

2.3 Antagonistic muscle actuator: principle of actuation

To produce a rotation of the joints, a pair of muscles exerts a force on two diametrically opposed points of a pulley. To relate the contraction ratio/elongation of the two muscles with the angular displacement, some concepts must be defined. The initial length of the muscles denoted l_{init} depends on their unloaded length $l_0 = 400$mm and on the initial shortening length δl. It has been established in [4] that the initial pressure in the two muscles in order to tension the cables around the pulley is 2.3 bar. This corresponds to the initial shortening of the pair of muscles needed to correctly engage the cable in the pulley. The numerical value of these, respectively for joints one and two, are $\delta l_1 = 55$mm and $\delta l_2 = 51$mm. To understand those quantities, they are graphically presented in figure 2.22.

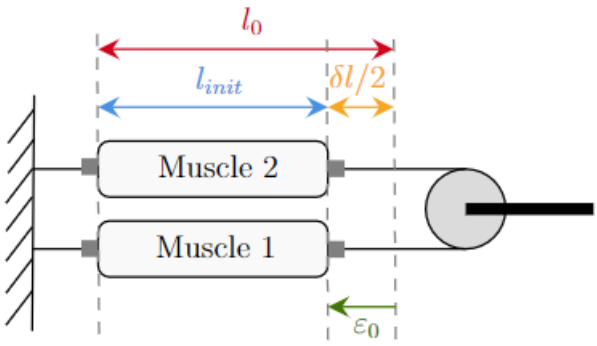

Figure 2.22: Initial length of the muscles (neutral position)[4]

The initial length l_{init} can be obtained as well as the initial contraction ratio

$$\begin{cases} l_{init} = l_0 - \dfrac{\delta l}{2} \\ \varepsilon_0 = \dfrac{l_0 - l_{init}}{l_0} \end{cases} \tag{2.8}$$

To ensure an adequate placement of the cables in the pulley grooves, the δl have to be identical on both side of the pulley. Otherwise, a risk of slacking is expected. After a calibration of the robot, the cables have been attached to place the robot in the initial configuration seen in figure 2.20 (dashed-line) when the same pressure on 2.3 bar is applied to the agonist-antagonist pair of muscles. Finally, in order to obtain a rotation, a variation of pressure is applied between the two muscles of a joint. The rotation of the pulley and thus the attached segment of an angle α around the neutral position can be related to the contraction ratio of each muscle (Fig. 2.23)

$$\begin{cases} \varepsilon_1 = \varepsilon_0 - \dfrac{R\alpha}{l_0} \\ \varepsilon_2 = \varepsilon_0 + \dfrac{R\alpha}{l_0} \end{cases} \tag{2.9}$$

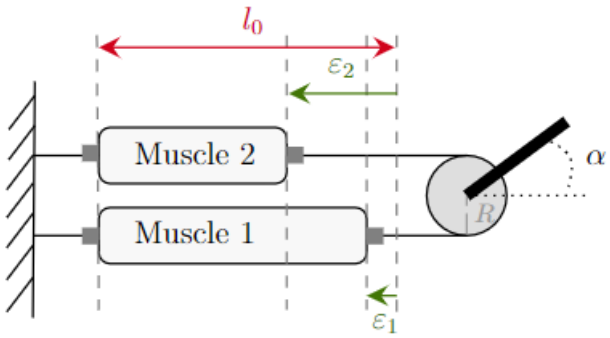

Figure 2.23: Length of the muscles (movement away from neutral position)[4]

It must be noted that the first joint is assembled slightly differently than the assembly showed in the presented figures. In that case, the pulley is maintained fixed on the support bolted to the table and the first segment turns around it. However, this different configuration can still be assimilated to the case in figure 2.23 and the same equation 2.9 but in this case the muscle numbering has to be permuted (muscle one would be on top and the other way round).

2.4 Summary

The robot consists in a 2 DoFs SCARA planar device. Two rotational joints allow the displacement of the first segment (arm) and the second (forearm) thanks to pneumatic artificial muscles as actuators. The patient interacts with the device via the end-effector handle resting on a carrier ball and measurements of the forces during the rehabilitation is done by means of a bi-axial sensor. Angular encoders record the angular displacement from the initial configuration and the communication between the robot and the CompactRIO is done via the *Labview*[35] software.

Some mechanical problems have been solved after a proper mechanical redesign. This helped to avoid bending in the second joint, ensure that the second angular sensor does not touch the table, allow motion of the patient's hand around the handle without hitting the handle support, limit the lever effects that distorted the force sensor measurements and prevent the cable from slipping inside the pulley groove.

To study the system, three reference frames have been defined. The first allows to establish the kinematics and dynamics following the Denavit-Hartenberg convention, the second rotates this convention to be aligned with the initial configuration of the robot from which the angular displacements are measured and the third helps to express the results of the performed experiments in a frame centered around the end-effector starting point and aligned with the workspace, for more convenience and easier interpretations.

The actuation principle based on two agonist-antagonist pair of muscles allows to induce rotations of the joints by contracting those using compressed air at different pressures. The relationship between the elongation of the muscles and the angular

displacement have been established and will be used later on to study the force, torque and stiffness achieved by the robot.

The main parameters useful to model and describe the robot behaviour and to study the dynamics of the robot that have been mentioned in this chapter are listed in table 2.1.

Table 2.1: Summary of the robots' key parameters

Parameters	**Joint 1**	**Joint 2**	**Unit**
Length of segments, L_i	700	450	mm
Pulley diameter, D_i	140	90	mm
Angular range, $\Delta\alpha_i$	45	65	$^\circ$
Initial shortening length, δl	55	51	mm

Chapter 3

Model based characterization of torque and stiffness limits of the robot in joint space

This chapter is intended to highlight the physical limitations of the robot. First, the force model experimentally developed in previous work[4] is recalled and a validation of this model is made, now considering the robot in its assembled configuration. Then, torque and stiffness limitations for each joint, their linkage given the agonist-antagonist actuation and the impact of position and pressure on those quantities is investigated.

3.1 Experimental force model validation

When it comes to modeling the behavior of an artificial pneumatic muscle, different approaches can be used. Some of them are purely theoretical while other try to fit experimental data in order to represent the behavior of the muscle in its actual configuration. The aim is thus to obtain the relationship describing the force developed by the pneumatic muscle as a function of its elongation and the pressure.

In previous work [4], it has been shown that the physical model based on the McKibben muscles was not appropriate to describe the behavior of the Festo muscles implemented on the robot because of their physically different nature. In a second step, the author has shown that the relationship provided by the manufacturer for the force to contraction link was again not representative in our case. Major differences were observed at low forces mainly due to the product characteristics and the ambient conditions that differed from those specified in a note of the data-sheet. A last step has thus helped to obtain a new experimental model adapted to the muscles mounted on the robot.

In the experiment formerly done, the procedure consisted in hanging the muscle vertically and subjecting it to a variable load. Thanks to different pressure applied and elongation measurements, a polynomial regression was then performed to fit

the data. The best result was given by a 5^{th}-order polynomial model, in order to correctly predict the changes at low force accurately. Note that the pressure P has been kept to the 1^{st}-order as to facilitate the inversion of the model and to be consistent with the approach provided by the manufacturer. In the model, forces are expressed in Newton [N], pressures in Pascal [P] and elongations are given in relative values ($\varepsilon = \frac{l_0 - l}{l_0}$).

First Experimental Model

$$F(P,\varepsilon) = aP\varepsilon^4 + bP\varepsilon^3 + cP\varepsilon^2 + dP\varepsilon + eP + f\varepsilon^5 + g\varepsilon^4 + h\varepsilon^3 + i\varepsilon^2 + j\varepsilon + k \quad (3.1)$$

Table 3.1: Values of the polynomial coefficients (First model)

a	b	c	d	e	f
-1.235	0.8748	-0.1696	0.003	0.0025	-6394597.5996

g	h	i	j	k
4353194.3094	-1296730.9029	188507.2445	-12713.2922	-58.1436

However, the set-up used to derive the experimental model is significantly different than the configuration of the muscles when assembled on the robot. Therefore, it has been decided to verify the validity of the first model and its coefficients when the muscles are mounted on the robot.

Methods

The following procedure was used: the robot is set in the configuration with the first segment locked and only one of the muscles is connected to the second joint pulley. In this one-muscle set-up, there are three pressure values that can actually be applied and provide meaningful measurements ($P = 2, 3$ and 4 bar). This limitation arises from the fact that pressure under 2 bar does not ensure a correct pre-tension on the cables, while pressure over 4 bar induces an initial shortening of the muscle causing the joint to be mechanically blocked due to the robot geometry. For each pressure imposed, the initial muscle shortening and the initial angle of the second arm are measured. An operator then moves the handle on the workspace, performing a 30^o displacement divided in twenty steps of around 1.5^o. The force at the handle is recorded and the muscle force is considered to be the reaction to the operator's measured force.

Results and Discussion

The comparison between the data obtained experimentally and the curves described by the polynomial fit previously done is shown in figure 3.1. Even though some differences may be observed, the new measurements are well described by the

previously developed model. With this in mind, the choice was made to keep the current experimental model in order to describe the force, pressure, elongation relationship.

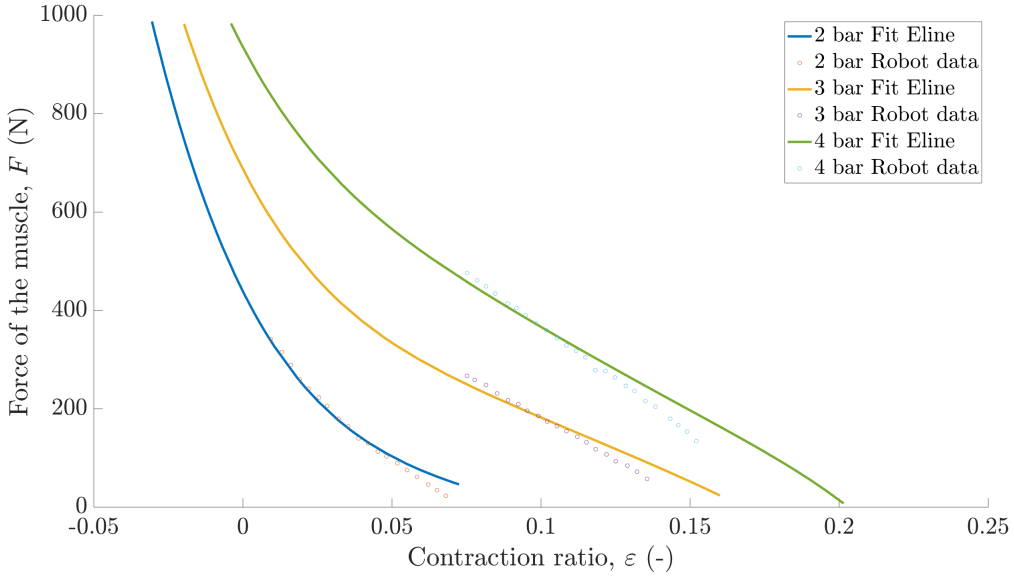

Figure 3.1: Force developed by the muscle as a function of the contraction ratio

3.2 Model based characterization

Methods

Based on the force developed by each muscle, it is possible to derive what are the torque and stiffness at a given joint, for specified pressure and elongation - since $F(\varepsilon, P)$. It is also possible to better understand how torque and stiffness are related, as well as the impact of the elongation and pressure.

The torque and stiffness developed a given joint can be expressed as [26] [36]:

$$\tau = R(F_2(\varepsilon_2, P_2) - F_1(\varepsilon_1, P_1)) \tag{3.2}$$

$$K = -\frac{\partial \tau}{\partial \alpha} = -R\left(\frac{F_2(\varepsilon_2, P_2)}{\partial \alpha} - \frac{F_1(\varepsilon_1, P_1)}{\partial \alpha}\right) \tag{3.3}$$

where $F_i(\varepsilon_i, P_i)$ is the force developed by pneumatic muscle i and is described by the 5^{th}-order polynomial experimental model presented in the previous section.

$$\begin{aligned} F(\varepsilon, P) &= aP\varepsilon^4 + bP\varepsilon^3 + cP\varepsilon^2 + dP\varepsilon + e + f\varepsilon^5 + g\varepsilon^4 + h\varepsilon^3 + i\varepsilon^2 + j\varepsilon + k \\ F(\varepsilon, P) &= A(\varepsilon)P + B(\varepsilon) \end{aligned} \tag{3.4}$$

Since the force is a function of the elongation ε, which, for a pair of muscles, is given by[1]

$$\begin{cases} \varepsilon_1 = \varepsilon_0 - \frac{R\alpha}{l_0} \\ \varepsilon_2 = \varepsilon_0 + \frac{R\alpha}{l_0} \end{cases} \tag{3.5}$$

It can be clearly observed that torque and stiffness capabilities depend on joint configuration. Furthermore, using the above relationship between ε and α, it is also possible to rewrite the stiffness equation as[2]

$$K = -\frac{R^2}{l_0}\left(\frac{\partial F_2}{\partial \varepsilon_2} + \frac{\partial F_1}{\partial \varepsilon_1}\right) \tag{3.6}$$

.

If physical limits of the robot, i.e. 0 bar $\leq P_1, P_2 \geq 5$ bar, are also taken into account, from equations 3.2 and 3.6 it can also be observed that not only are those quantities intrinsically linked, but also that one bounds the other. This becomes clearer if the force expression is rewritten for a given position (i.e. given $(\varepsilon_1, \varepsilon_2)$). In this case, forces are (from equation 3.4)

$$\begin{cases} F_1(P_1) = A_1 P_1 + B_1 \\ F_2(P_2) = A_2 P_2 + B_2 \end{cases} \tag{3.7}$$

The forces then are simply linearly dependent on the pressure, meaning torque is proportional to the difference between both pressures $(P2 - P1)$ while stiffness is proportional to the sum $(P_2 + P_1)$. Considering P_1 and P_2 must stay within the specified range, the sum is bounded to $P_2 + P_1 = 10$ bar ($P_2 = P_1 = 5$ bar), but then $P2 - P1 = 0$ bar. Conversely, the difference is bounded to $P_2 - P_1 = \pm 5$ bar ($P_2 = 5$ bar, $P_1 = 0$ bar or $P_2 = 0$ bar, $P_1 = 5$ bar), but then $P_2 + P_1 = 5$ bar. Ultimately, for a specified joint configuration, for a desired torque, there is a range of available stiffness. Conversely, for a desired stiffness, an attainable torque range is defined.

From those relationships, it is then possible to find the locus of achievable stiffness and torque for a given configuration. This locus is given by a quadrilateral, since it will be the intersection of the four sets of inequations $[P_1 \geq 0 \text{ bar}, P_2 \geq 0 \text{ bar}]$, $[P_1 \leq 5 \text{ bar}, P_2 \geq 0 \text{ bar}]$, $[P_1 \geq 0 \text{ bar}, P_2 \leq 5 \text{ bar}]$ and $[P_1 \leq 5 \text{ bar}, P_2 \leq 5 \text{ bar}]$.

In order to find this locus, the first step is discretizing the angular range of each joint in 1^o steps. Then, for each discretized position, the four vertices of the quadrilateral are found as follows. Two of the vertices represent configurations with K_{max} and K_{min} for $\tau = 0$ Nm. The maximum stiffness K_{max} is achieved, for an angular configuration where $P_1 > P_2$[3], when $P_1 = 5$ bar, $P_2 = P_{2,max}$ bar, where $P_{2,max}$ is the pressure that ensures $F_1 = F_2$. Following the same reasoning, the minimum stiffness K_{min} is the configuration in which $P_1 = P_{1,min}$ bar, $P_2 = 0$ bar. However,

[1] These relationships were described in Chapter 2

[2] Full mathematical development can be found in appendix B

[3] The same reasoning can be conducted considering the case $P_2 > P_1$, since a joint angular range is given as $[-\alpha, +\alpha]$. Only one case was developed for the sake of concision.

due to the robot's characteristics, a minimum force is needed to ensure that there is no slacking of the cables. For the neutral position, previous work[4] has determined this minimum force[4]. This force can then be used to find the pressure configuration $P_1 = P_{1,min}$ bar, $P_2 = P_{2,min}$ bar which, given the geometrical configuration (and, thus, the elongation of each muscle), ensures that there is no slacking of the cables. This represents the case with K_{min}.

The two other vertices are given by the maximum and minimum torques (τ_{max} and τ_{min}) achievable, i.e. $P_1 = 5$ bar, $P_2 = 0$ bar and $P_1 = 0$ bar, $P_2 = 5$ bar. In both cases, the sum of pressures is 5 bar, so the stiffness are the same. If this stiffness is defined as K_τ, it is then possible to summarize the four vertices of each locus (limit conditions) for each position as described in table 3.2. Finally, the quadrilateral is drawn by connecting these vertices.

Table 3.2: Limit conditions for a given joint configuration where $P_1 > P_2$

τ	K	P_1	P_2
0	K_{min}	$P_{1,min}$	$P_{2,min}$
0	K_{max}	5 bar	$P_{2,max}$
τ_{max}	K_τ	0 bar	5 bar
τ_{min}	K_τ	5 bar	0 bar

Results and Discussion

The overall results are shown in figures 3.2 and 3.3. It can be clearly seen that those capabilities do not remain constant for different joint configurations.

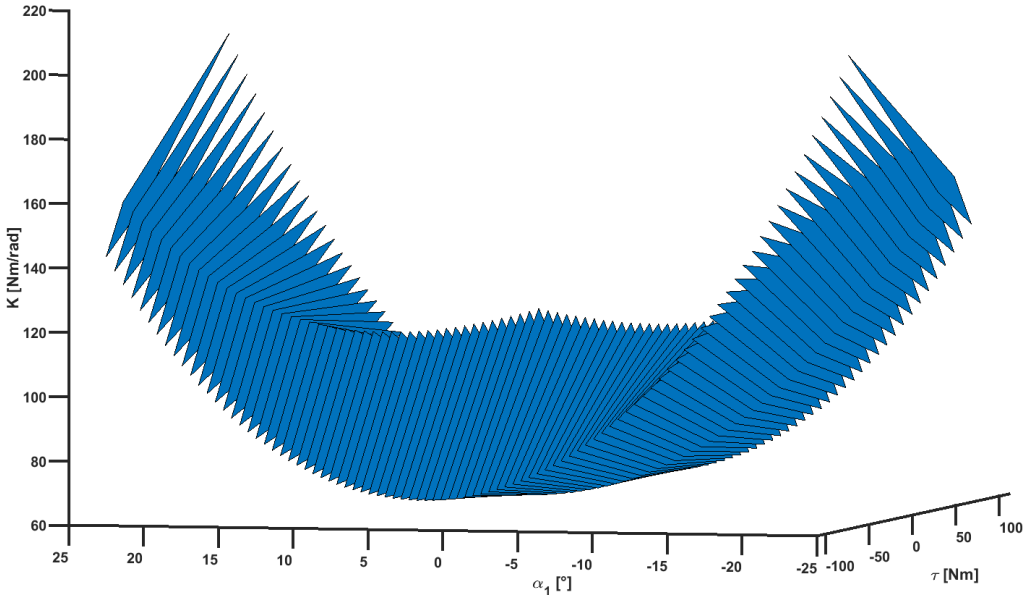

Figure 3.2: Locus of (achievable stiffness, torque) pairs for full range of joint 1 positions

[4]This is the force given by $P = 2.3$ bar on all four muscles and $\varepsilon_0 = 6.88\%$ (for joint 1) and $\varepsilon_0 = 6.38\%$ (for joint 2), meaning $F_{init} = 188.47$N for joint 1 and $F_{init} = 131.08$N for joint 2

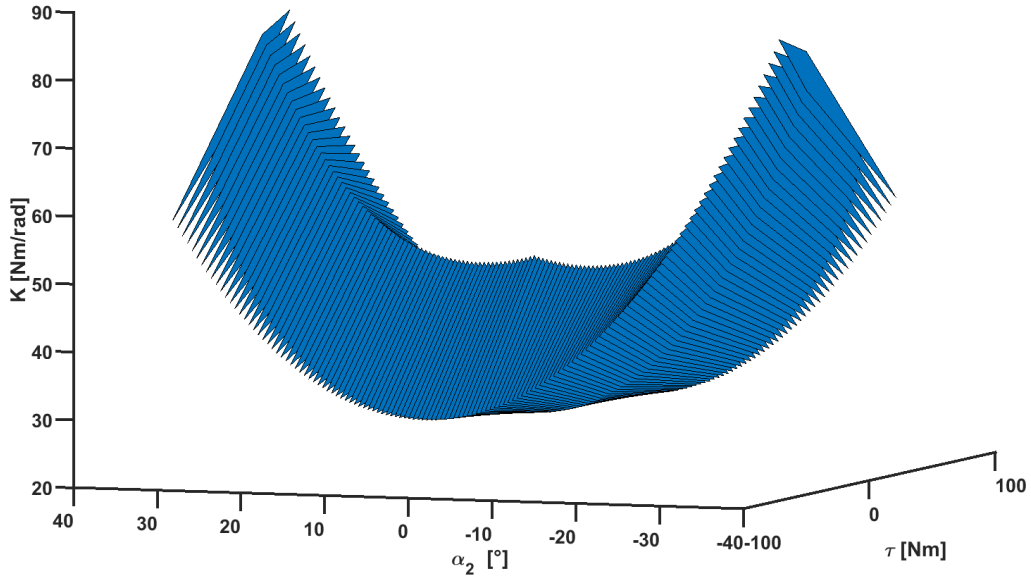

Figure 3.3: Locus of (achievable stiffness, torque) pairs for full range of joint 2 positions

In order to better understand the meaning of those loci, it is interesting to analyse the result for a specific configuration as an example (Fig. 3.4a and 3.4b). The orange dots are the limit configurations, i.e. (τ_{min}, K_τ), (0, K_{min}), (0, K_{max}), (τ_{max}, K_τ). Then, the dotted red line illustrates the possible stiffness values, given a desired torque (here $\tau_1 = 25$ Nm and $\tau_2 = 25$ Nm). Finally, the dotted green line illustrates the analogous situation: possible torque domain, given a desired stiffness (here, $K_1 = 75$ Nm/rad and $K_2 = 45$ Nm/rad). This illustrates that, as previously mentioned, when considering the physical limits of the robot, a desired torque bounds the possible stiffness achievable and a desired stiffness limits the possible torque achievable.

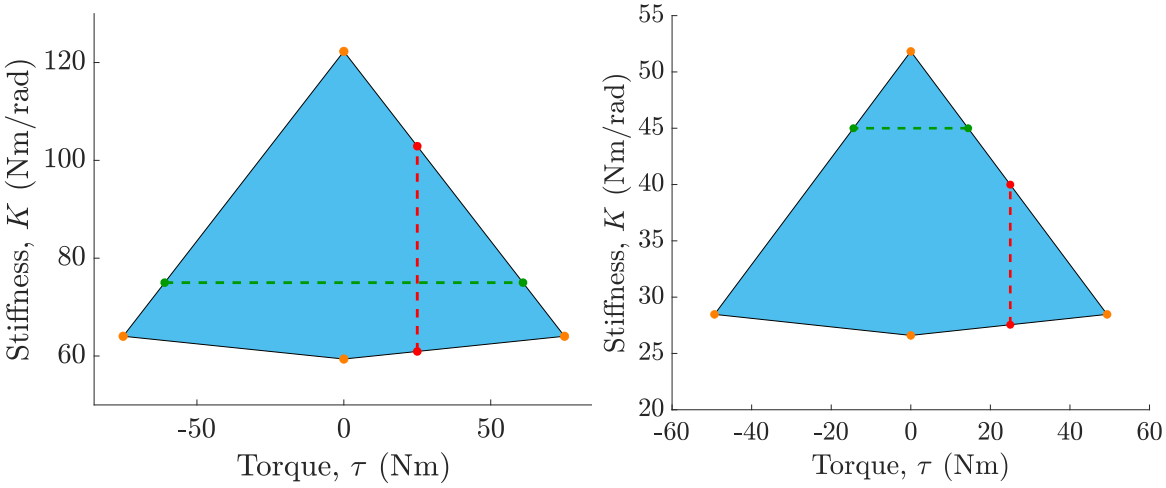

(a) Robot capability domain for joint 1 - $\alpha_1 = 0°$

(b) Robot capability domain for joint 2 - $\alpha_2 = 0°$

Figure 3.4: Example of robot capabilities locus for specific configuration $\alpha_1 = \alpha_2 = 0°$

From the limit torque curves (Fig. 3.5a and 3.5b), it is possible to establish the maximum and minimum torque capabilities at each configuration. In addition to that, a range of torque that is achievable for the whole joint space (for each joint) can be determined. For joint 1, this range is [-31.5 Nm, 31.5 Nm] and for joint 2, [-22 Nm, 22 Nm]. It must be noted that those torques are achievable for a different set of stiffness values, for each configuration.

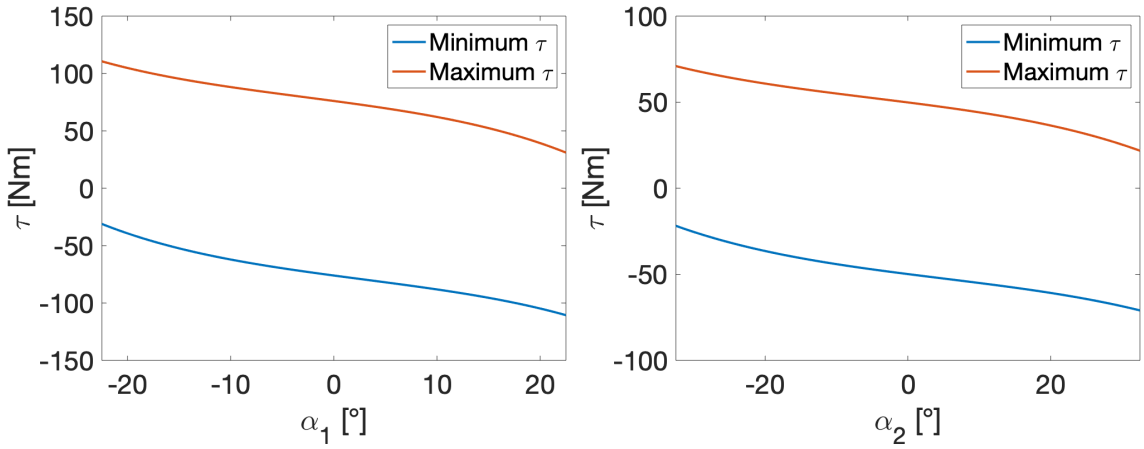

(a) Torque limits for joint 1

(b) Torque limits for joint 2

Figure 3.5: Torque limits for robot joints - evaluated independently

Other valuable insights can be extracted from minimum and maximum stiffness at $\tau = 0$ Nm. This is illustrated in figures 3.6a and 3.6b. The differences in stiffness and torque capabilities absolute values can be explained by geometrical differences (pulley radius $R_1 \neq R_2$) and differences in initial elongation $\varepsilon_{0,1} \neq \varepsilon_{0,2}$.

Both curves are symmetric - as expected from the elongation evolution considering the principle of actuation of the agonist-antagonist assembly. There is also a narrowing of the achievable stiffness range ΔK. Clearly, the lowest achievable stiffness is obtained when $\alpha_i = 0°$, $i = (1, 2)$. This is because it is the neutral position, i.e. the position in which $P_1 = P_2 = 2.3$ bar, so the only initial pressure needed in the muscles is the one to ensure that we have the anti-slacking force. It also means that it is the configuration in which the variation of pressures can be the highest (from the initial 2.3 bar to 5 bar for both muscles), which translates into the largest $\Delta K = K_{max} - K_{min}$.

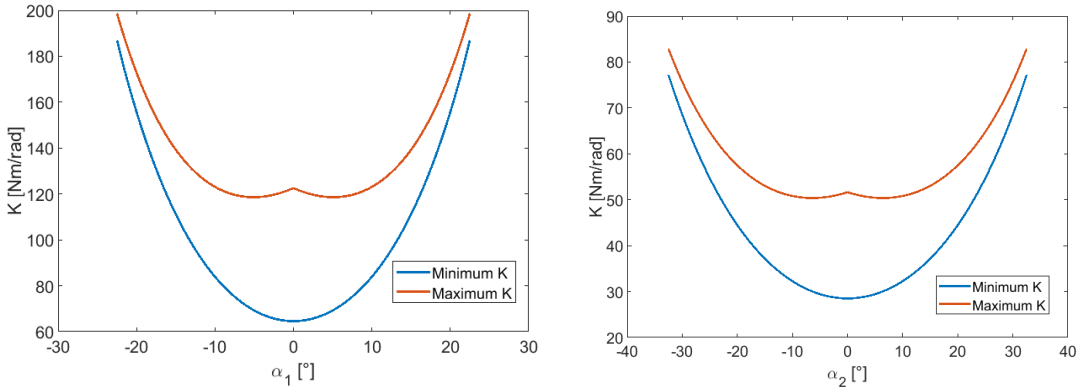

(a) Stiffness limitations at $\tau = 0$ Nm - joint 1 (b) Stiffness limitations at $\tau = 0$ Nm - joint 2

Figure 3.6: Stiffness limits for $\tau = 0$ Nm - evaluated independently for each joint

The curves for minimum and maximum stiffness do not have, however, the same shape. In order to understand this difference and specially the explanation behind the fact that a peak is observed at $\alpha_i = 0°$ for the maximum stiffness, additional investigation of the impact of each muscle on the stiffness was conducted.

Investigation of difference in the shape of the limit stiffness curves

Methods

The investigation is done based on the analysis of half the angular range of joint 1 ($[0; 22.5°]$). Since the same type of behavior is observed for both joints and that the curves are symmetrical, the results can be extended to the full angular range, as well as the second joint. The evolution of pressures as a function of the angular position for the minimum and maximum stiffness at zero torque is obtained following the reasoning that led to table 3.2. Then, based on those curves, it is possible to better understand this different shape between both limit conditions.

Results and Discussion

The result obtained is illustrated in figures 3.7a and 3.7b. It is clear that the evolution is not the same. For the minimum stiffness, one pressure increases and the other decreases as the angular position evolves. For the maximum one, one pressure stays constant (at the physical limit) and the other decreases in order to ensure that the angular position and zero torque conditions are respected.

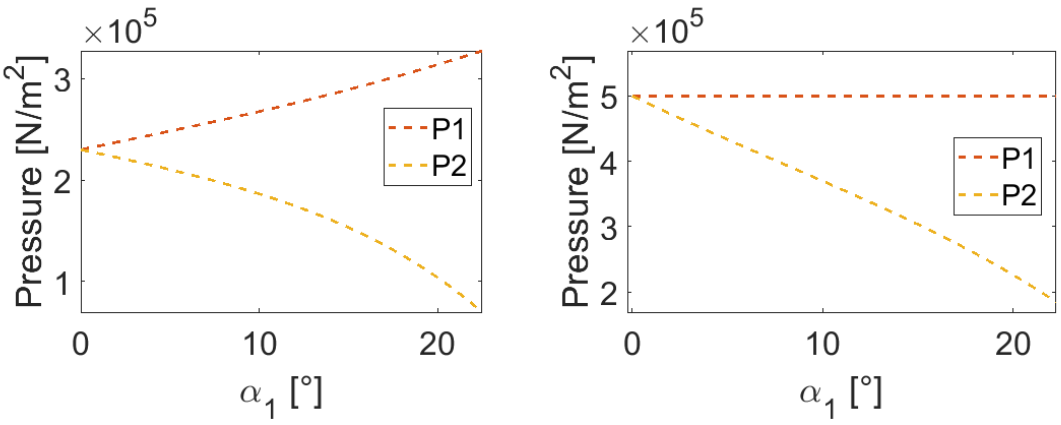

(a) Pressure evolution for joint 1 ($\alpha_1 = [0; 22.5°]$) - minimum stiffness

(b) Pressure evolution for joint 1 ($\alpha_1 = [0; 22.5°]$) - maximum stiffness

Figure 3.7: Pressure evolution in function of the angular position for limit stiffness conditions

This difference is then translated into the contributions of the two muscles to the joint stiffness, particularly concerning the contribution of the muscle associated with $P1$ (Fig. 3.8a and 3.8b). Then, for the minimum stiffness case, the evolution of $P1$ is such that the contribution of this muscle to the stiffness remains relatively constant. The overall shape of the minimum stiffness is then governed by the contribution of the muscle associated with $P2$. However, for the maximum stiffness, the $P1$ muscle contribution decreases, while the $P2$ contribution has a similar shape (since $P2$ has a similar behavior for minimum and maximum stiffness). This explains the shape of the maximum stiffness, in which the fact that $P1$ contribution is not a simple offset changes the minimum of the curve, shifting it to the right (and no longer at the center). Due to the symmetry, this creates a peak at $\alpha_1 = 0°$ and explains the difference between the overall shape of the two limit curves.

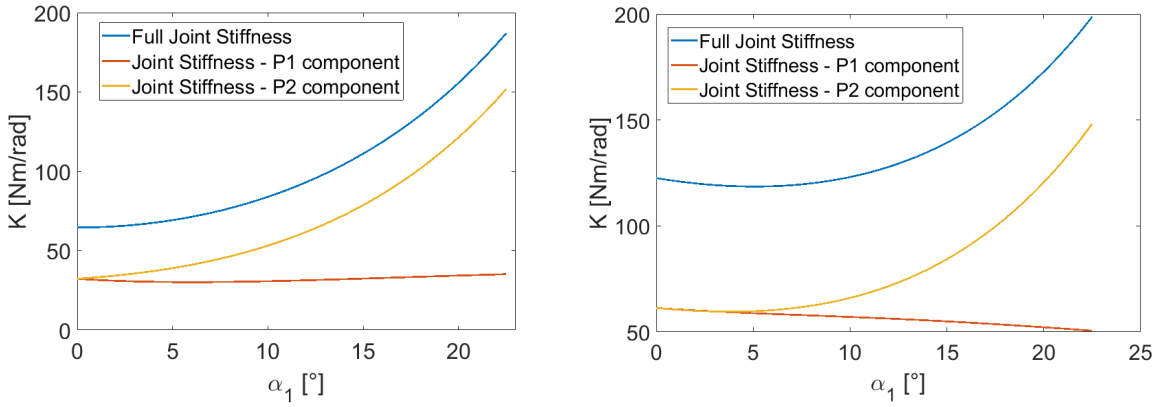

(a) Stiffness limits - joint 1 ($\alpha_1 = [0; 22.5°]$) - minimum stiffness

(b) Stiffness limits - joint 1 ($\alpha_1 = [0; 22.5°]$) - maximum stiffness

Figure 3.8: Stiffness components evolution in function of the angular position for limit conditions

3.3 Summary

In order to better understand the limitations the robot, a model based characterization to identify torque and stiffness limits was performed. Since those two quantities depend on the force, a first step was revisiting the force model previously developed. The model for the muscle force as a function of the pressure and its elongation, developed in [4] was verified, considering now the muscles in their working configuration.

The validated model was then used to obtain the locus of achievable torque and stiffness for each of the two joints of the robot. These quantities depend on the force, so they also depend on elongation, from position, and pressure. Their limits come from the limits on the pressure values and there are four limiting configurations: minimum and maximum stiffness for zero torque and minimum and maximum torque. The procedure used to find these points, as well as the resulting loci, was described. The locus for each angular configuration is a quadrilateral since, for a given position, forces depend linearly on pressure. Analysing one example of locus, the fact that torque and stiffness will bound each other was illustrated. Using this quadrilateral, it is possible to find stiffness range for a given torque (or torque range for a desired stiffness).

Then, some global analyses were presented with respect to those limiting conditions. The maximum and minimum achievable torques for the two joints were shown. They depend on the angles made by the segments, however a range of achievable torques for the whole workspace could be obtained. Joint one is able to achieve a range of $[-31.5, 31.5]$ Nm and joint two $[-22, 22]$ Nm. The limit stiffness at zero torques can be described by two curves over position range, one representing the minimum and the other, the maximum. It was identified that the range narrows as one moves away from the central configuration, this being explained by the imposed limit of 5 bar in the muscles and additional constraints in pressure when moving from the center position, needed in order to keep the pose of the robot. The lowest achievable joint stiffness is when the robot is in neutral position. Further analyses were conducted in order to better understand why minimum and maximum curves do not have the same shape.

Chapter 4

Open loop identification of the robot dynamics

The previous chapter provided insight on torque and stiffness capabilities of the robot's joints. However, it did not take into account damping or mass effects on the behavior of the robot. It was also done in the joint frame, whereas the robot is intended to move in the Cartesian reference frame defined in chapter 2. The following chapter describes the experimental characterization of the robot, in order to establish possible differences between model based characterization as well as identify the impact of damping and mass phenomena. This is carried out in the central reference frame and the goal is to obtain a full dynamic characterization, considering a mass-spring-damper system.

4.1 Dynamic model transposition - from joint to Cartesian domain

In order to represent the results in a Cartesian reference frame, the transposition from inertia, angular damping and angular stiffness to mass, linear damping and linear stiffness can be performed as follows [29]. From the two-link model of the robotic arm in the 2D frame, each of the muscles is represented as a linear series combination of spring and damper elements. If the equilibrium angular position is defined as θ_0, a model of the torque-displacement relationship can be established[1] :

$$\tau = K_j[\theta - \theta_0] + B_j\dot{\theta} \tag{4.1}$$

where K_j and B_j are respectively the joint stiffness and damping matrices around the equilibrium angular position. Considering the inertia of the two segments represented by their inertia matrices $I(\theta_0)$ and taking into account the Coriolis and centrifugal effects in $C(\theta_0, \dot{\theta})$, the full joint-based model of the 2D Scara robot becomes:

[1]For the rest of this section, the "j" subscript expresses a matrix defined in the joint space while the "C" subscript expresses a matrix defined in the Cartesian space

$$\tau = I(\theta_0)\ddot{\theta} + C(\theta_0, \dot{\theta}) + B_j\dot{\theta} + K_j[\theta - \theta_0] \tag{4.2}$$

As it is more convenient to work in the Cartesian frame, it is possible to use the following relationships to establish the relation between the joint-based model to the Cartesian-based model:

$$\tau = J^T(\theta_0)F \tag{4.3}$$
$$\dot{X} = J(\theta_0)\dot{\theta} \tag{4.4}$$
$$\delta X = J(\theta_0)\delta\theta \tag{4.5}$$

where F is the force on the end-effector expressed in the Cartesian reference frame and (4.5) is obtained from (4.4) according to the virtual work principle. Finally, (4.5) is valid if small displacements are assumed and thus approximately valid for small excursions from the equilibrium point. Therefore:

$$X - X_0 \approx J(\theta_0)[\theta - \theta_0] \tag{4.6}$$

Differentiating (4.4), we obtain:

$$\ddot{X} = J(\theta_0)\ddot{\theta} + J(\dot{\theta}_0)\dot{\theta} \tag{4.7}$$

As for small excursions the derivative of the Jacobian is negligible:

$$\ddot{X} \approx J(\theta_0)\ddot{\theta} \tag{4.8}$$

Using (4.3), (4.4), (4.6) and (4.8) in (4.2), and by dropping the theta-argument, it is possible to derive:

$$F = J^{-T}[IJ^{-1}\ddot{X} + B_jJ^{-1}\dot{X} + K_jJ^{-1}(X - X_0)] \tag{4.9}$$

This can be re-written:

$$F = M_C\ddot{X} + B_C\dot{X} + K_C(X - X_0) \tag{4.10}$$

where Cartesian mass, damping and stiffness matrices at the Cartesian equilibrium point X_0 are:

$$M_C = J^{-T}IJ^{-1} \tag{4.11}$$
$$B_C = J^{-T}B_jJ^{-1} \tag{4.12}$$
$$K_C = J^{-T}K_jJ^{-1} \tag{4.13}$$

Considering the configuration of the 2D Scara robot studied here, the joint stiffness and damping matrices are diagonal. The form of the inertia matrix can be derived from the dynamic equations for the elbow and shoulder torques τ_2 and τ_1 which can be found from kinematics, the Newton-Euler equations and d'Alembert's Principle for the robot configuration [37]:

$$\begin{bmatrix}\tau_1\\ \tau_2\end{bmatrix} = \begin{bmatrix}I_{11} & I_{12}\\ I_{21} & I_{22}\end{bmatrix}\begin{bmatrix}\ddot{\theta}_1\\ \ddot{\theta}_2\end{bmatrix} + \begin{bmatrix}C_1\\ C_2\end{bmatrix} \tag{4.14}$$

with

$$I_{11} = I_1 + I_2 + m_2 l_1 l_2 cos(\theta_2)\frac{m_1 l_1^2 + m_2 l_2^2}{4} + m_2 l_1^2 \tag{4.15}$$

$$I_{22} = I_2 + \frac{m_2 l_2^2}{4} \tag{4.16}$$

$$I_{12} = I_{21} = I_2 + \frac{m_2 l_1 l_2}{2} cos(\theta_2)\frac{m_2 l_2^2}{4} \tag{4.17}$$

where m_1, m_2 are the mass and I_1, I_2 are the rotational inertias of segment 1 and 2 respectively. The joint inertia, damping and stiffness matrices can thus be expressed with the following generalized shape:

$$I = \begin{bmatrix}I_1 & I_3\\ I_3 & I_2\end{bmatrix} \quad (4.18) \quad B_j = \begin{bmatrix}B_1 & 0\\ 0 & B_2\end{bmatrix} \quad (4.19) \quad K_j = \begin{bmatrix}K_1 & 0\\ 0 & K_2\end{bmatrix} \quad (4.20)$$

As presented in 4.11 to 4.13, the transformation between the joint to the Cartesian space can be formalized as a pre-multiplication by the inverse of the Jacobian's transpose and post-multiplication by the inverse of the Jacobian. Thus it comes in a generalized way so that:

$$R_C = (J^{-1})^T R_j J^{-1} = A^T R_j A \tag{4.21}$$

with $A = J^{-1} = \begin{bmatrix}a & b\\ c & d\end{bmatrix}$ a matrix of any kind. This yields:

$$\begin{aligned} M_C &= \begin{bmatrix}a & c\\ b & d\end{bmatrix}\begin{bmatrix}I_1 & I_3\\ I_3 & I_2\end{bmatrix}\begin{bmatrix}a & b\\ c & d\end{bmatrix} \\ &= \begin{bmatrix} a^2 I_1 + 2acI_3 + c^2 I_2 & abI_1 + cdI_2 + (ad+bc)I_3 \\ abI_1 + cdI_2 + (ad+bc)I_3 & b^2 I_1 + 2bdI_3 + d^2 I_2 \end{bmatrix} \end{aligned} \tag{4.22}$$

and

$$K_C = \begin{bmatrix}a & c\\ b & d\end{bmatrix}\begin{bmatrix}K_1 & 0\\ 0 & K_2\end{bmatrix}\begin{bmatrix}a & b\\ c & d\end{bmatrix} = \begin{bmatrix} a^2 K_1 + c^2 K_2 & abK_1 + cdK_2 \\ abK_1 + cdK_2 & b^2 K_1 + d^2 K_2 \end{bmatrix} \tag{4.23}$$

The same reasoning used for K_C can be applied to obtain B_C, since they are both diagonal. Given the development in 4.22 and 4.23, that the I_j elements can either be positive or negative depending on the angular position θ_2 and that the B_j and K_j are positive definite, the general form of the M_C, B_C and K_C matrices can be set as

$$M_C = \begin{bmatrix} M_{xx} & M_{xy} \\ M_{xy} & M_{yy} \end{bmatrix} [kg] \quad (4.24) \qquad B_C = \begin{bmatrix} B_{xx} & B_{xy} \\ B_{xy} & B_{yy} \end{bmatrix} \left[\frac{N}{(m/s)}\right] \quad (4.25)$$

$$K_C = \begin{bmatrix} K_{xx} & K_{xy} \\ K_{xy} & K_{yy} \end{bmatrix} \left[\frac{N}{m}\right] \quad (4.26)$$

with the following constraints: all matrices are symmetric and B_C and K_C matrices have positive diagonals[2].

4.2 Data acquisition and Post-processing

From the torque and stiffness relationships, combined with the experimentally derived force expression, it was possible to obtain the direct model of the robot: given a set of pressures (P_1, P_2) for one pair of muscles, obtain position, stiffness and torque developed by that joint. It was also established that force, and as a consequence, torque and stiffness, depend linearly with the pressure at a given position. It is then also possible to invert the model[4]. The inverse model developed takes three inputs for each joint i: position (α_i) - in order to obtain the elongation, stiffness (K_i) and torque (τ_i) and determines the pressure pair (P_1, P_2) for that joint. The expression of the inverted model is developed in Appendix B. Using this inverse model, the robot is controlled in open loop, as shown in figure 4.1.

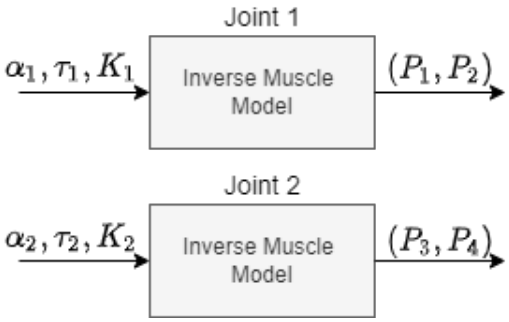

Figure 4.1: Open Loop control of the muscle: specified α, τ and K are translated into the pressure pair for each joint

The final workspace is determined as the blue rectangle in figure 4.2a. Since the stiffness limits depend on the position, five points of interest (marked in red) were chosen: the center of the workspace as well as points around 3/4 of the demi-diagonals of the rectangle. The angles that describe those positions were obtained from the inverse kinematics of the robot. At each position of interest, an 8cmx8cm square (or the circumscribed circle) was used as reference for the movements, as illustrated

[2]The units of the KBM matrices are presented here and are respectively for K, B, M: $[kg], \left[\frac{N}{(m/s)}\right]$ and $\left[\frac{N}{m}\right]$ but for the sake of conciseness, the following results for those matrices are given without their units.

by figure 4.2b. For each point of interest, not only dynamic trials were made, in which the operator used the red circle as reference for a continuous movement, but static trials were also conducted. For these trials, the light blue points were used as references, meaning for each trial, nine points were considered. The need for both types of trials is explained in the next section.

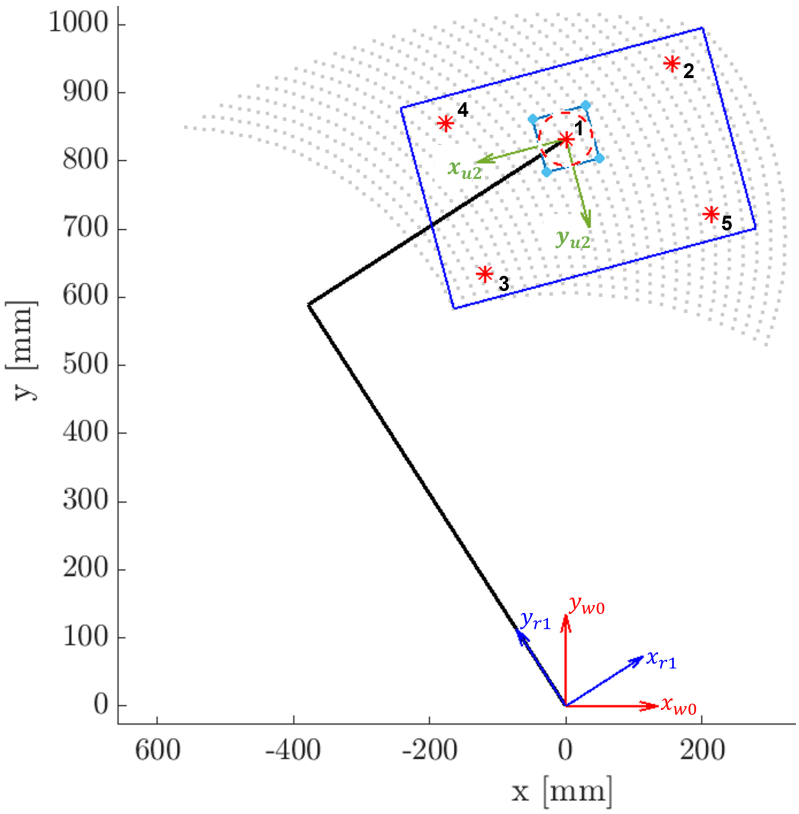

(a) Points of interest chosen for the trials and reference for movements in scale

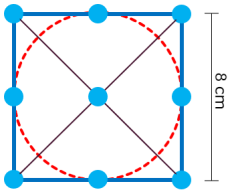

(b) Detail of the reference used for movements during experimental trials

Figure 4.2

On top of position, torque and stiffness need to be specified. For this characterization, the case where the robot does not impose an active torque (i.e. $\tau_1 = \tau_2 = 0$ Nm) is considered. Taking this into account, as well as the position, it is possible to use the theoretical characterization presented above to determine the range of possible stiffness values at those points of interest, independently for each joint. Then, for each point, it was decided to test both a low and a high stiffness configuration, so that $K_{low} = K_{min}$ and $K_{high} = K_{max} - 0.2 \cdot \Delta K$, where $\Delta K = K_{max} - K_{min}$ and $K_{max/min}$ is the maximum/minimum stiffness for a given configuration. The numerical values that correspond to these configurations are shown in table 4.1. This resulted in 10 configurations tested (two stiffness - minimum and maximum - for five points). In order to eliminate hysteresis phenomena in the muscle, measurements only started after the robot was in steady state.

For static trials, data is collected for 5s after stabilization at each one of the 9

Table 4.1: Input values for the inverse model used for experimental characterization

	α_1 [deg]	α_2 [deg]	$K_{low,1}$ [Nm/rad]	$K_{high,1}$ [Nm/rad]	$K_{low,2}$ [Nm/rad]	$K_{high,2}$ [Nm/rad]
1	0	0	60.8	110	26.6	46.8
2	-16	20.5	117.2	138.1	44.1	55
3	16.5	-26	121.2	141.1	56.3	64.2
4	10	6.5	81.2	113.8	28.2	45.9
5	-13.5	-11.5	99.5	125.3	31.8	47.2

points. For dynamic trials, data is collected for 90 seconds. During this time, an operator moves the handle at different speeds in order to obtain a rich frequency content. In both cases, position and force measurements are obtained using the robot own instrumentation, using a sampling time $T_s = 50$ ms. This sampling time was chosen since the governing loop of the system runs at around $30 \sim 40$ ms. Also, for each configuration, two trials were made, in which two different operators manipulated the robot.

After data acquisition, some post processing had to be performed. The available information from the encoders are positions (α_1, α_2), which are translated to Cartesian XY coordinates in the central reference frame using direct kinematics. Then, in order to obtain velocities, the position signal is derived ($\dot{x}_t = \frac{x_{t+1}-x_t}{Ts}$ and $\dot{y}_t = \frac{y_{t+1}-y_t}{Ts}$), then forward-backward filtering was done in order to remove high-frequency noise that might have been induced with the derivation. A 10th-order butterworth filter, with cutoff frequency of 8Hz, which is a standard cutoff frequency value when it comes to human movement[38], was used. A similar procedure was carried out in order to obtain the acceleration ($\ddot{x}_t = \frac{\dot{x}_{t+1}-\dot{x}_t}{Ts}$ and $\ddot{y}_t = \frac{\dot{y}_{t+1}-\dot{y}_t}{Ts}$) and forward-backward filtering was applied. Finally, as previously mentioned, measured forces (F_x, F_z) are in the sensor's reference frame, so a rotation is needed in order to put them in our central reference frame.

4.3 System identification from dynamic equations - time domain

Methodology

With the information obtained via the experiments, the first goal was to try to identify the parameters that could describe the system using the dynamic equations. For the static trials, the system is described as a pure spring (Eq. 4.27) and, due to the symmetry of matrix K_C, there are only three parameters to be fitted. The equilibrium positions X_0 and Y_0 were taken from the measured starting position, since a difference was observed between the desired equilibrium position (from table 4.1) and the measured one. Another requirement regarding the values from matrix K_C is that the diagonals, i.e. $k_{1,s}$ and $k_{2,s}$, must be positive values.

$$\begin{bmatrix} F_x \\ F_y \end{bmatrix} = K_{C,static} \begin{bmatrix} (X - X_0) \\ (Y - Y_0) \end{bmatrix}, \text{ where } K_{C,static} = \begin{bmatrix} k_{1,s} & k_s \\ k_s & k_{2,s} \end{bmatrix} \tag{4.27}$$

In order to comply with these constraints regarding the form of matrix K_C, the system was rewritten (Eq. 4.28) so that the symmetry condition could be imposed. There are then two equations per data point. Also, given the sampling period and data acquisition procedure previously described, there are around 900 data points per static trial. Therefore, in order to obtain the three parameter values using all data points, a linear least-squares solver with linear constraints was used, and constraints were defined so that $k_{1,s} > 0$ and $k_{2,s} > 0$.

$$\begin{bmatrix} (X - X_0) & (Y - Y_0) & 0 \\ 0 & (X - X_0) & (Y - Y_0) \end{bmatrix} \begin{bmatrix} k_{1,s} \\ k_s \\ k_{2,s} \end{bmatrix} = \begin{bmatrix} F_x \\ F_y \end{bmatrix} \tag{4.28}$$

For the dynamic trials, a similar procedure was followed, with the system being described as a full mass-spring-damper system (equation 4.29). Since the Cartesian matrices are all symmetrical, there are now twelve parameters to be determined. The equilibrium positions X_0 and Y_0 are again taken from the measured starting position.

$$\begin{bmatrix} F_x \\ F_y \end{bmatrix} = M_C \begin{bmatrix} \ddot{X} \\ \ddot{Y} \end{bmatrix} + B_C \begin{bmatrix} \dot{X} \\ \dot{Y} \end{bmatrix} + K_C \begin{bmatrix} (X - X_0) \\ (Y - Y_0) \end{bmatrix}, \text{ where} \\ M_C = \begin{bmatrix} m_1 & m_3 \\ m_3 & m_2 \end{bmatrix} B_C = \begin{bmatrix} b_1 & b_3 \\ b_3 & b_2 \end{bmatrix} K_C = \begin{bmatrix} k_1 & k_3 \\ k_3 & k_2 \end{bmatrix} \tag{4.29}$$

The system was again rewritten (equation 4.30) as to impose the symmetry condition - this time for all three matrices. There are again two equations per data point and, from trials duration and sampling period, around 1800 data points per trial. A linear least-squares solver with linear constraints was used, and constraints were defined so that $k_1 > 0$, $k_2 > 0$, $b_1 > 0$ and $b_2 > 0$.

$$\begin{bmatrix} \ddot{X} & \ddot{Y} & 0 & \dot{X} & \dot{Y} & 0 & (X - X_0) & (Y - Y_0) & 0 \\ 0 & \ddot{X} & \ddot{Y} & 0 & \dot{X} & \dot{Y} & 0 & (X - X_0) & (Y - Y_0) \end{bmatrix} \begin{bmatrix} m_1 \\ m_3 \\ m_2 \\ b_1 \\ b_3 \\ b_2 \\ k_1 \\ k_3 \\ k_2 \end{bmatrix} = \begin{bmatrix} F_x \\ F_y \end{bmatrix} \tag{4.30}$$

In order to obtain the numerical values, 80% of the data collected was used[3]. The reason for this choice was the fact that understanding how well the fitted parameters describe the system is not trivial by simply analysing the matrices. By fitting the parameters using 80% of the data, it is then possible to use the remaining 20% as a test set to better quantify the quality of the fit.

Results and Discussion

An example of the results obtained is illustrated by the matrices below. They represent trials made at point 1 (Center), at maximum and minimum stiffness[4].

$$K_{C,static_{MIN}} = \begin{bmatrix} 145.9 & 73.5 \\ 73.5 & 387.0 \end{bmatrix} K_{C,static_{MAX}} = \begin{bmatrix} 200.3 & 101.7 \\ 101.7 & 516.6 \end{bmatrix}$$

4.1: $K_{C,static}$ matrix for point 1 - minimum ($_{MIN}$) and maximum ($_{MAX}$) stiffness

$$M_C = \begin{bmatrix} 0.93 & -0.053 \\ -0.053 & -0.027 \end{bmatrix} B_C = \begin{bmatrix} 26.6 & 9.4 \\ 9.4 & 0.9 \end{bmatrix} K_C = \begin{bmatrix} 253.7 & 107.1 \\ 107.1 & 364.0 \end{bmatrix}$$

4.2: K, B, M matrices for point 1, minimum stiffness

$$M_C = \begin{bmatrix} 0.97 & -0.22 \\ -0.22 & -0.052 \end{bmatrix} B_C = \begin{bmatrix} 17.8 & 6.2 \\ 6.2 & 2.5 \end{bmatrix} K_C = \begin{bmatrix} 304.1 & 166.7 \\ 166.7 & 491.5 \end{bmatrix}$$

4.3: K, B, M matrices for point 1, maximum stiffness

From those values, it is interesting to compare the stiffness values fitted using the least-squares solver to the ones predicted by the force model, translated to Cartesian stiffness values using equation 4.13. The choice to perform both a static and a dynamic trial was motivated by the difference observed between the experimentally fitted parameters and the ones predicted by the model. For the diagonal terms, this is illustrated in figure 4.3. It appears that the stiffness is higher than predicted which could be from the quality of the fit or from differences in how the stiffness was obtained experimentally and with the model.

[3]Since there were two measurements for each trial (two operators), the results were then averaged

[4]Results for the other tested points can be found in Appendix C

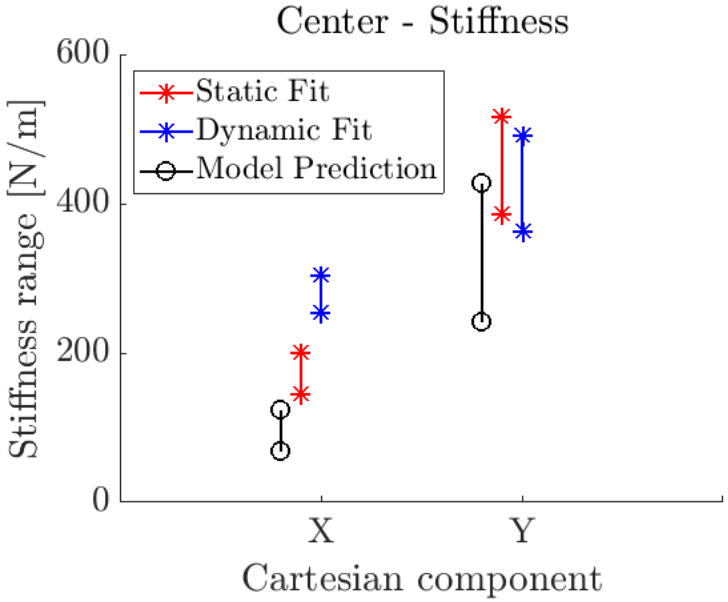

Figure 4.3: Diagonal stiffness terms comparison

To determine the quality of the fit, the following has been done. As previously stated, understanding how well the fitted parameters describe the system solely from the values of the matrices is not trivial. Therefore, from the remaining 20% of data and the fitted K_C, B_C, M_C matrices, the force predicted by the fit was obtained (from equation 4.29) and was then compared to the measured force for this data. The result can be seen in figures 4.4 and 4.5. Overall, at low frequencies the fitted parameters describe quite well the system for both X and Y-axis components.

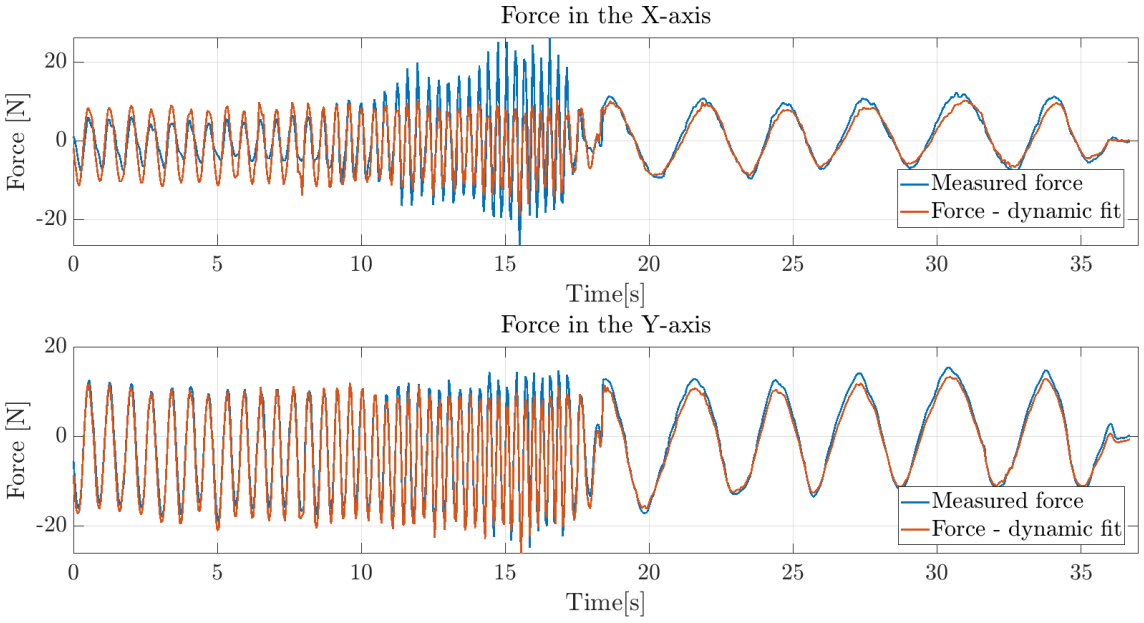

Figure 4.4: Measured and computed forces for point 1, minimum stiffness

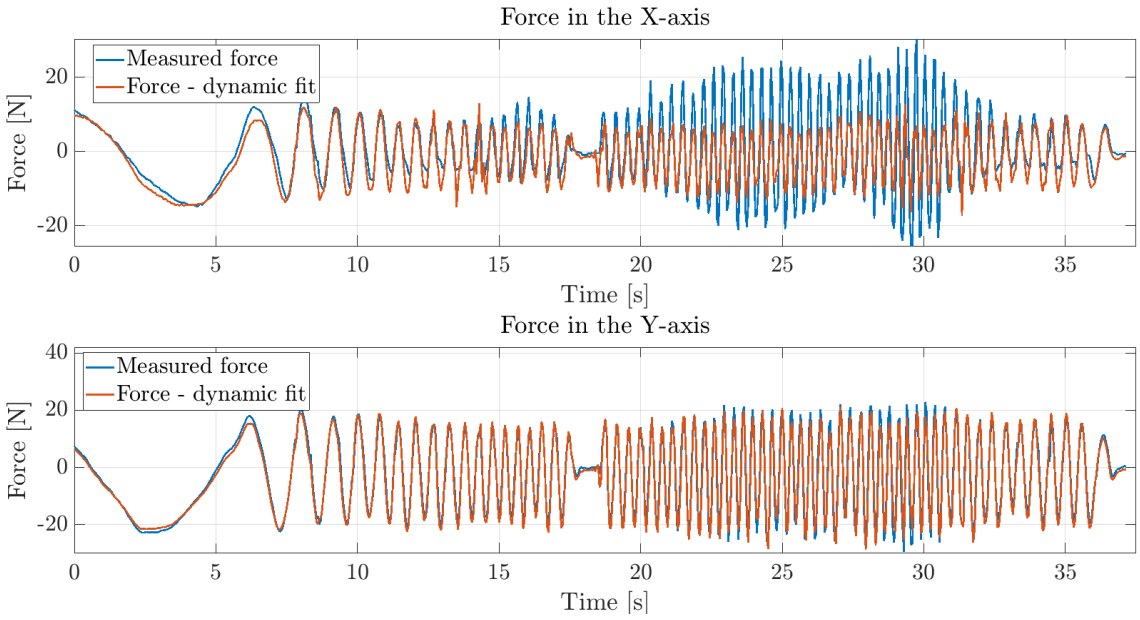

Figure 4.5: Measured and computed forces for point 1, maximum stiffness

The fact that the description of the system in low frequencies is close to the reality indicates that the difference observed between predicted stiffness values from the force model and fitted ones most likely does not come from fitting errors. In order to confirm this, it is interesting to decompose the total force in its three components (elastic, damping and inertial) to see if the behaviour of the robot agrees with the classic behavior of a mass-spring-damper system, i.e. for forces at low frequencies, the stiffness component dominates.

The results of the decomposition are shown in figures 4.6 and 4.7. They effectively confirm that the behavior of the system, as described by the fitted parameters, agrees with the behaviour of a mass-spring-damper system. Therefore, even if the values experimentally obtained for the stiffness do not agree with the ones predicted by model, they are most likely to be the real stiffness experienced by the operators. With increasing frequencies, damping components and then inertial components become more significant, also corresponding to a mass-spring-damper system behavior.

A possible explanation regarding the difference obtained between the measured stiffness and the one predicted by the model is the fact that the predicted stiffness is obtained from the derivative of the force. Nonetheless, the force model - presented in chapter 3 - is highly non linear and so its derivative at one point has a value specific for that point that may not correspond well to points nearby. The one obtained via the fitted parameter tries to find the slope that best approximates the force/displacement relationship over the whole set of Δx explored during one trial. In other words, the value obtained from the derivative represents the slope at the equilibrium point, whereas the one obtained via the temporal fit is the value that best approximates the slope over the whole range of Δx travelled during a trial.

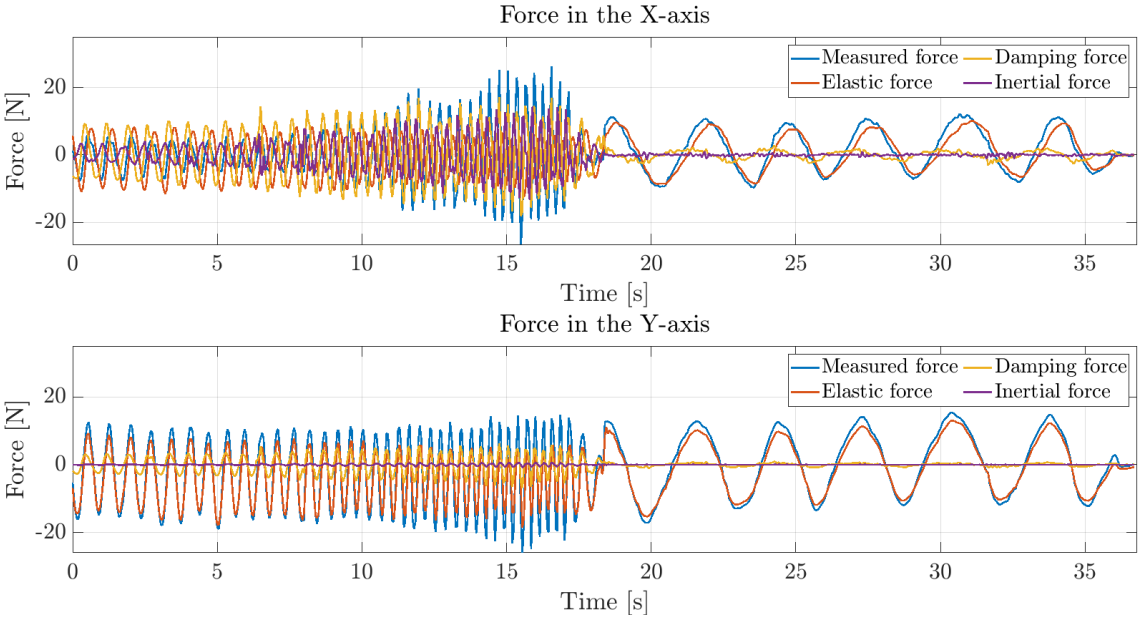

Figure 4.6: Force decomposition for point 1, minimum stiffness

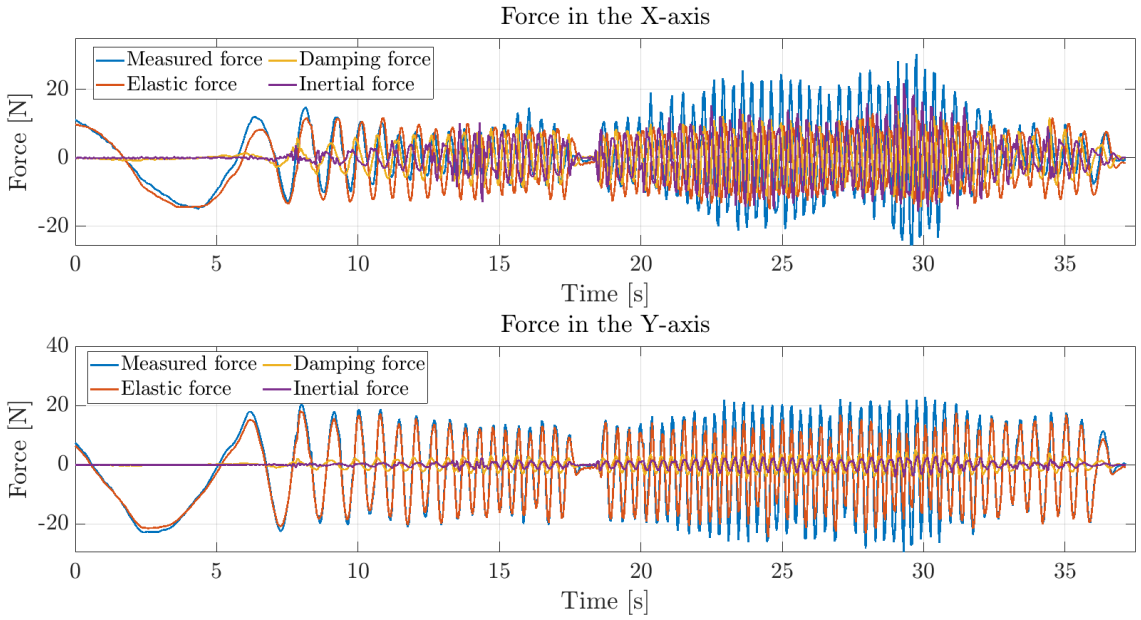

Figure 4.7: Force decomposition for point 1, maximum stiffness

It was also noted that there is a difference in accuracy of the fit between different frequencies, which can be better quantified by analysing the mean-squared error (MSE). In order to do that, both trials showed in the figures above were split in half. For the first one, the first half was considered to be high frequency and the second, low frequency - and inversely for the second trial. The results can be observed in table 4.2. Since both sets contained the same amount of data, it is possible to compare and analyse the values from both trials simultaneously.

Table 4.2: Mean-Squared Error for point 1 trials

(a) Minimum stiffness

	Low freq.	High freq.	Full test set
X-axis	2.0	26.6	14.3
Y-axis	4.6	1.8	3.2

(b) Maximum stiffness

	Low freq.	High freq.	Full test set
X-axis	8.2	61.4	34.9
Y-axis	2.6	9.2	5.8

It can be noted that, for the X-axis, there is a larger difference of MSE values for high and low frequencies, as it would be expected from visual inspection of the figures. For the Y-axis, the difference between low and high frequencies is inconsistent between trials - for minimum stiffness, MSE at low frequencies is larger but the inverse is observed for maximum stiffness. However, since the difference between them is significantly smaller compared to the differences observed for the X-axis, this indicates that the quality of the fit in Y is conserved for different frequencies. The difference in fit accuracy at higher frequencies for the force in the X-axis motivated conducting a study in the frequency domain, as described in the next section.

The MSE values for the complete test set were also used in order to confirm quantitatively the fact that the fitted parameters for the Y-axis force describe more accurately the system than the ones for the X-axis. As expected, in both cases the MSE for the complete data set is larger for the X-axis when compared to the one in the Y-axis - around five times larger.

Another way of quantifying the quality of the fit is using the R^2 or coefficient of determination, which represents the amount of variance in the dependent variable accounted for/explained by the model. For $R^2 = 1$, this means a perfect model - which means that a higher coefficient of determination is an indication of a more accurate fit. Again, it can be confirmed that the fit quality is better in the Y-axis (Tab. 4.3). Also, it is clear that the models do not predict perfectly the force.

Table 4.3: Coefficient of determination for temporal fit of point 1 - minimum and maximum stiffness

	Min	Max
X-axis	0.7544	0.6581
Y-axis	0.9689	0.9681

4.4 System identification from system impedance - frequency domain

The results obtained in the previous section indicate that the system can be appropriately described by a spring-mass-damper system. However, for the X component, a difference in the fit quality in function of the frequency - which translates into the presence of more or less significant damping and inertial forces -

was observed. This motivated performing a frequency domain analysis, using the impedance concept.

Methods

The impedance of a system describes the relationship between effort and flow variables. In the mechanical domain, it is then described as the ratio between the Laplace transform of the force to the speed so that

$$Z(s) = \frac{F(s)}{V(s)} \tag{4.31}$$

For a simple 1 DoF mass-spring-damper system, the dynamic equation in the time domain is[5]:

$$f = m\ddot{x} + b\dot{x} + k\Delta x \tag{4.32}$$

This equation in the frequency domain can be obtained from the speed and force Laplace transforms, so that:

$$F = (ms + b + \frac{k}{s})V \tag{4.33}$$

$$\frac{F}{V} = ms + b + \frac{k}{s} \tag{4.34}$$

The transfer function above represents then the impedance of the system. It is then possible to obtain the Bode diagram describing the system behavior in function of the frequency. Analysing the Bode magnitude diagram for a generic mass-spring-damper system (Fig. 4.8), it is possible to note three distinct phases. At low frequencies, the spring behavior dominates, associated with the decreasing slope. At high frequencies, the mass behavior dominates, characterized by the increasing slope. Finally, in between, the damper behavior dominates and it is characterized by a simple gain (no slope).

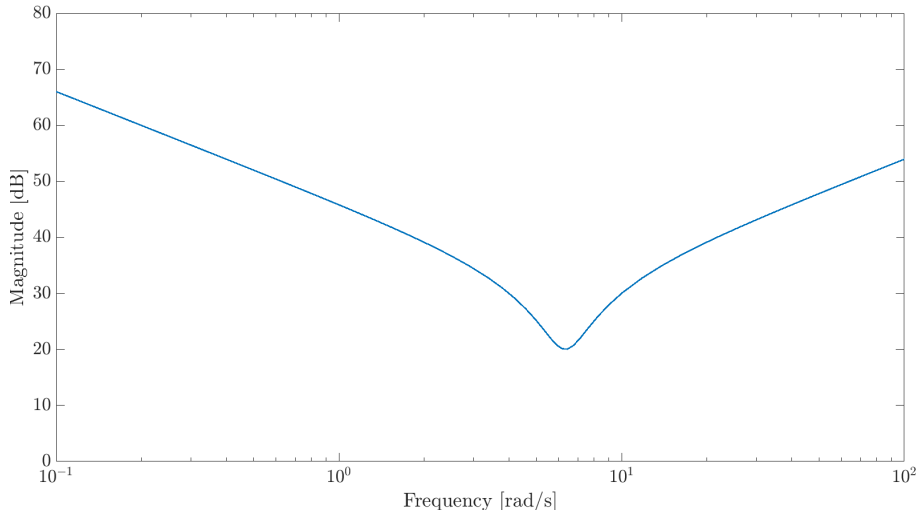

Figure 4.8: Magnitude bode plot of the impedance of a mass spring damper system

[5]Here, k, b and m represent generalized parameters for stiffness, damping and mass

From the mass (m), spring (k) and damper (b) values, the impedance of the system at a certain frequency (ω) can be obtained as:

$$Z = \frac{\sqrt{(b*\omega)^2 + (k - m*\omega^2)^2}}{\omega} \text{ with } |F| = Z \cdot |V| \tag{4.35}$$

where |F| and |V| denote the magnitude of the force and the v respectively, from their single-sided amplitude spectrum.

For a 2 DoF coupled system, such as the Scara robot which is subject of this work, it is possible to obtain an equivalent expression by extending these notions. From the dynamic equations in the time domain (Eq. 4.29), the equations in the frequency domain are:

$$F_x = \left(m_1 s + b_1 + \frac{k_1}{s}\right) V_x + \left(m_3 s + b_3 + \frac{k_3}{s}\right) V_y$$
$$F_y = \left(m_3 s + b_3 + \frac{k_3}{s}\right) V_x + \left(m_2 s + b_2 + \frac{k_2}{s}\right) V_y$$

And from the impedance:

$$|F_x| = Z_1 \cdot |V_x| + Z_3 \cdot |V_y|$$
$$|F_y| = Z_3 \cdot |V_x| + Z_2 \cdot |V_y|$$

where

$$Z_i = \frac{\sqrt{(b_i*\omega)^2 + (k_i - m_i*\omega^2)^2}}{\omega}, i = \{1, 2, 3\}$$

Then, the procedure in order to obtain the parameters from the frequency equations and the data obtained from the experiment and post-processing was as follows. From the data, the single-sided amplitude spectrum (obtained from the Fast Fourier transform) of the force and speed signals, as well as the frequency values, were extracted. To take into account the trials performed by the two different operators at each experimental configuration, the two values obtained for those magnitudes were averaged. Also, a user-defined function was specified as:

$$F = Z_1 \cdot V_1 + Z_2 \cdot V_2 + Z_3 \cdot V_3 \text{ so that:}$$

$$\rightarrow \text{ When } F = F_x,\ F = F_x = Z_1 \cdot V_x + Z_2 \cdot V_y + Z_3 \cdot 0$$

$$\rightarrow \text{ When } F = F_y,\ F = F_y = Z_1 \cdot 0 + Z_2 \cdot V_x + Z_3 \cdot V_y$$

This allowed all nine parameters to be fitted simultaneously, assuring that the symmetry condition would be respected. The data used as input for the function is then the magnitude of V_1, V_2 and V_3, as well as the frequency. Using the newly

obtained data mentioned above and this user-defined function, a non-linear curve-fitting solver was used in order to find the best parameters to describe the system, in the least-squares sense. The fitted parameters from the temporal analysis were used as the initial points for the curve-fitting solver.

An example of what was obtained for the single-sided amplitude spectrum of the force and speed signals is depicted in figures 4.9 and 4.10. Those are the results for point 1, minimum stiffness. Analysing their content, it was determined that the force signal for frequencies higher than 22 rad/s was considerably low when compared to the rest of the spectrum. For this reason, only frequencies up to that value were used when performing the fit.

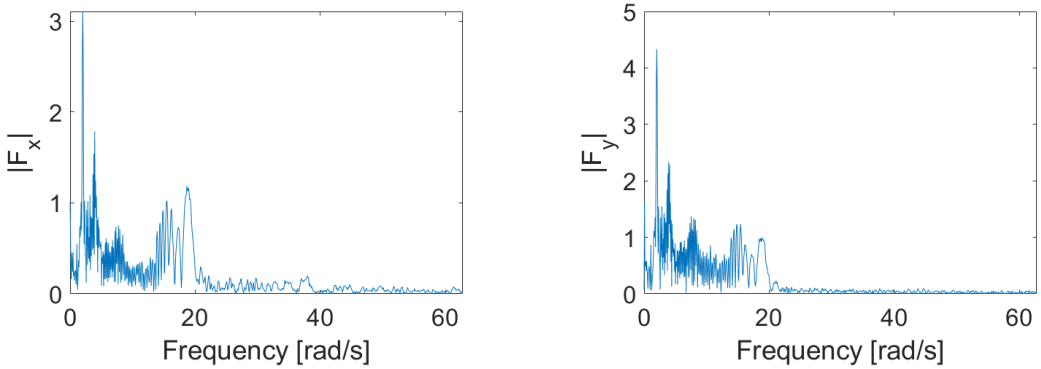

(a) X-axis force (b) Y-axis force

Figure 4.9: Single sided amplitude spectrum - force signals

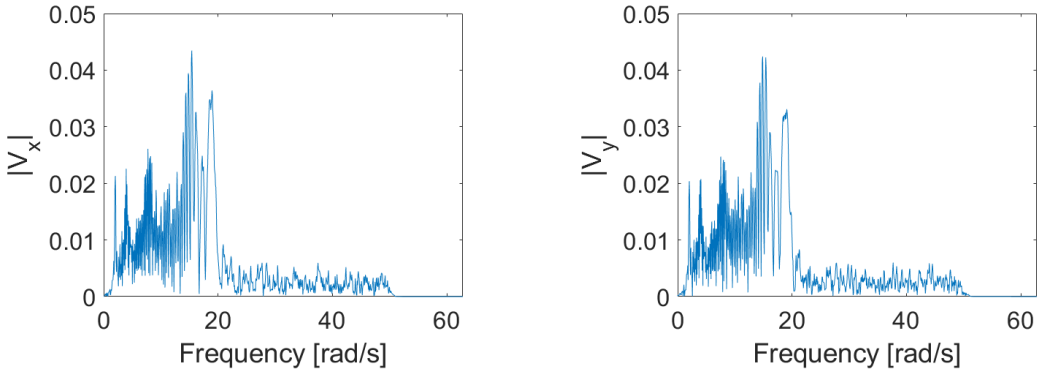

(a) X-axis velocity (b) Y-axis velocity

Figure 4.10: Single sided amplitude spectrum - velocity signals

Results and Discussion

From the parameter values obtained, it is possible to write the K_C, B_C and M_C matrices. If point 1 is once more used as an example, the obtained results are[6]:

[6]As for the temporal fit, results for the other tested points can be found in Appendix D

$$M_C = \begin{bmatrix} 1.9 & 0.53 \\ 0.53 & 0.0024 \end{bmatrix} B_C = \begin{bmatrix} 12.9 & 2.6 \\ 2.6 & 16.9 \end{bmatrix} K_C = \begin{bmatrix} 203.8 & 103.5 \\ 103.5 & 332.9 \end{bmatrix}$$

4.4: K, B, M matrices obtained for point 1, minimum stiffness

$$M_C = \begin{bmatrix} 1.9 & 0.70 \\ 0.70 & 0.0015 \end{bmatrix} B_C = \begin{bmatrix} 14.4 & 1.9 \\ 1.9 & 18.7 \end{bmatrix} K_C = \begin{bmatrix} 248.3 & 124.7 \\ 124.7 & 414.1 \end{bmatrix}$$

4.5: K, B, M matrices obtained for point 1, maximum stiffness

In order to have a better understanding of how well those values capture the behavior associated with the experimentally obtained force magnitude, figures 4.11 and 4.12 show the magnitude obtained via the estimated parameters alongside the experimental one, for both minimum and maximum stiffness. Qualitatively, there seems to be a good agreement between the predicted and measured values.

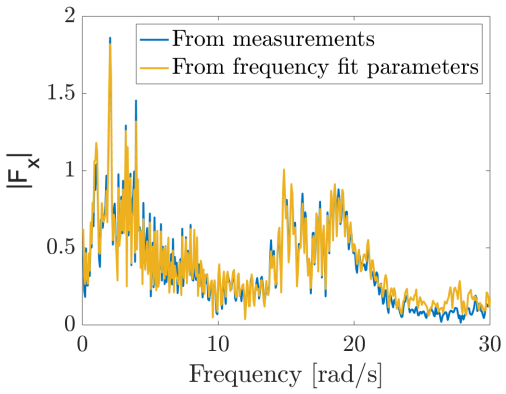

(a) X-axis force - Point 1

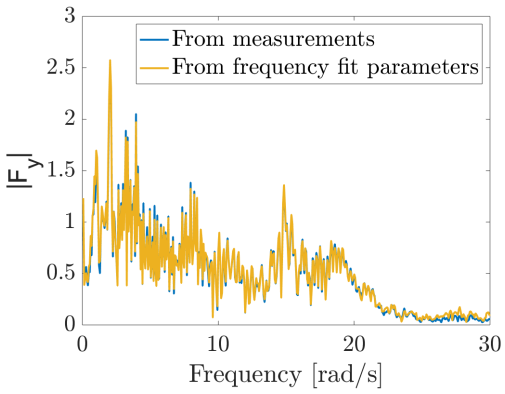

(b) Y-axis force - Point 1

Figure 4.11: Single sided amplitude spectrum of force signals - minimum configuration

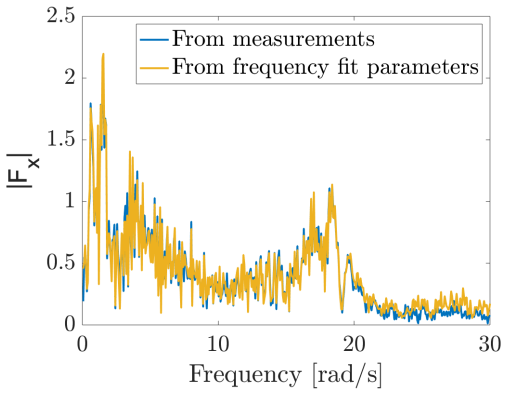

(a) X-axis force - Point 1

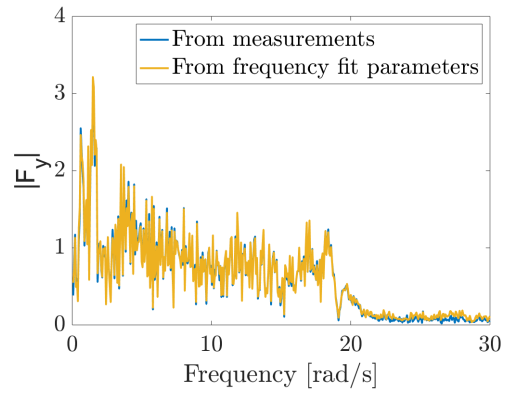

(b) Y-axis force - Point 1

Figure 4.12: Single sided amplitude spectrum of force signals - maximum configuration

The coefficient of determination can again be used to evaluate quantitatively the quality of the fit. The values obtained are in table 4.4. Even if a better fit quality is observed in the Y-axis, the values for the coefficient of determination are high for the X-axis as well $R^2_{mean} \approx 0.83$).

Table 4.4: Coefficient of determination for frequency fit of point 1 - minimum and maximum stiffness

	Min	Max
X-axis	0.8095	0.8622
Y-axis	0.9867	0.9877

4.5 Comparison - temporal and frequency domain fit

The values of the matrices for the frequency fit are not exactly the same as the ones obtained via the temporal fit performed in the previous section. In order to try to compare the results obtained by the two different methods, a first approach is comparing the coefficient of determination obtained by each fit. From tables 4.3 and 4.4, it is observed that, in both cases, the R^2 values for the Y-axis are considerably high ($R^2 > 0.95$) and are better than the ones obtained for the X-axis. Also, for the X-axis, there is a more significant difference between the values obtained for the temporal fit and the frequency fit.

The difference between Y-axis and X-axis is larger in the temporal fit. This could be due to the fact that higher frequencies were not considered when performing the frequency fit. Given that it was also showed that the temporal fit was less accurate at higher frequencies, this choice when performing the frequency fit could have impacted the results.

Another interesting analysis is comparing the measured force with the one predicted by the fitted parameters yielded by each model, when using the equations in time domain. From the result (Fig. 4.13 and 4.14), it can already be noted that the frequency fit has lower accuracy than the temporal fit in the temporal domain.

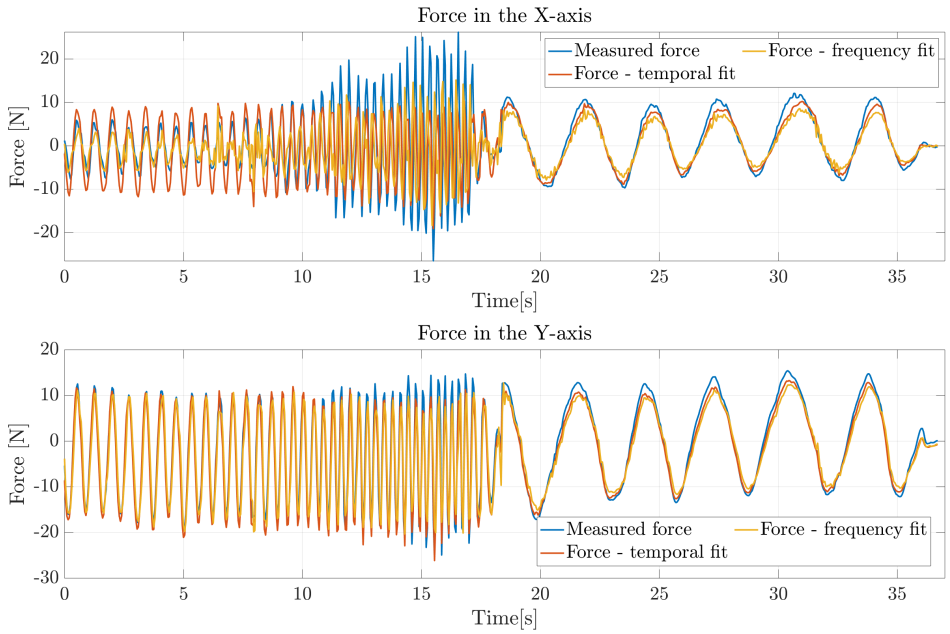

Figure 4.13: Measured and computed forces for different predicted parameters - Point 1, minimum stiffness

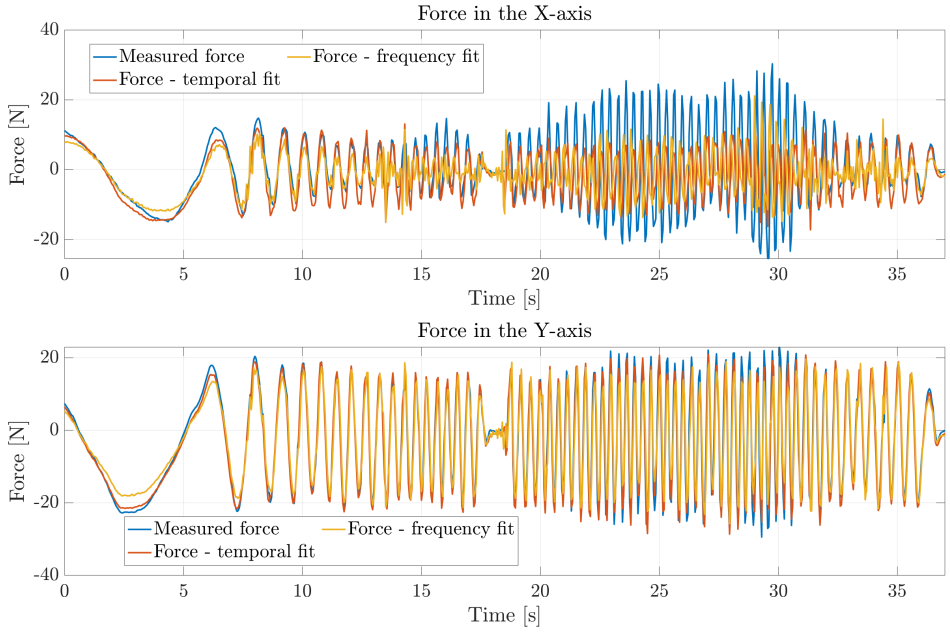

Figure 4.14: Measured and computed forces for different predicted parameters - Point 1, maximum stiffness

Another way of comparing the results is by comparing the force magnitude obtained when using the two different sets of parameters (Fig. 4.15 and 4.16). In this case, the parameters obtained via the frequency fit are the ones that better

estimate the force magnitude.

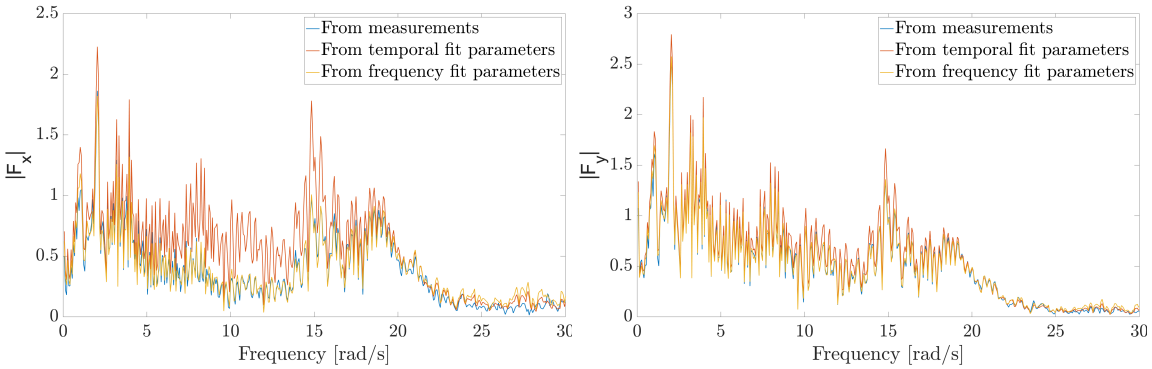

(a) X-axis force - Point 1 (b) Y-axis force - Point 1

Figure 4.15: Single sided amplitude spectrum of force signals fitting comparison - minimum configuration

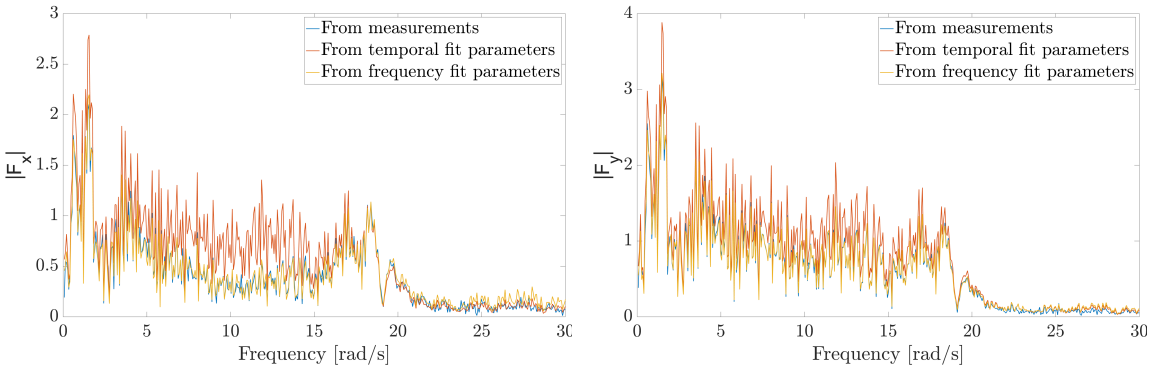

(a) X-axis force - Point 1 (b) Y-axis force - Point 1

Figure 4.16: Single sided amplitude spectrum of force signals fitting comparison - maximum configuration

Comparing both results is therefore not straightforward and one cannot claim with certainty that one is better than the other. Regardless, both methods yield results that are acceptable, considering that the objective is to better understand the global behavior of the system. Further comparison can be made by analysing the other points as well.

4.6 Graphical elliptic representation and comparison for different poses

Methods

A concise graphical way of representing the impedance matrix is using an ellipse, characterized by its surface, aspect ratio and orientation. The surface is proportional

to the determinant of the matrix, the aspect ratio is defined by the ratio of its larger to its smaller eigenvalues and the orientation is given by the angle between the direction of the principal eigenvector and the X-axis. To transform a 2D-symmetric matrix Z into an elliptic representation in function of surface, aspect ratio and orientation, the following equations are used [29]

$$Z = \begin{bmatrix} s_1 & s_2 \\ s_2 & s_3 \end{bmatrix} \tag{4.36}$$

$$\lambda_{2,1} = \frac{1}{2}\left[(s_1 + s_3) \pm \sqrt{(s_1 + s_3)^2 + 4(s_2^2 - s_1 s_3)}\right] \tag{4.37a}$$

$$A = \pi \lambda_1 \lambda_2 \tag{4.37b}$$

$$R = \frac{\lambda_2}{\lambda_1} \tag{4.37c}$$

$$\theta = tan^{-1} \frac{s_2}{\lambda_2 - s_3} \tag{4.37d}$$

where λ_i are the eigenvalues ($\lambda_2 \geq \lambda_1$), A is the area, R is the aspect ratio and θ is the orientation.

The qualitative interpretation of the ellipse is the following: the major axis is the direction along which the impedance is maximum Z_{max}, whereas the minor axis is the direction of the minimum impedance Z_{min}. The angle of the ellipse θ gives the direction of the major axis, thus the impedance Z_{max}. As those impedance terms multiply the position, speed and acceleration, giving respectively the elastic, damping and inertial components of the force (equation 4.10), they represent the direction along which the impact of those components in the overall perceived force are the largest and smallest.

Results and Discussion

The ellipses obtained for the K_C, B_C and M_C matrices identified for the five points of interest, previously shown in figure 4.2a, are presented below. Both the temporal and frequency identification of the matrices are used to provide the results in the elliptic form. For each of the two methods, the results for the minimum and maximum stiffness imposed are illustrated. For each of the three investigated matrices, a reference circle with indicated units and corresponding values helps to have an idea of the numerical value of the parameters.

The ellipses representing the stiffness can be observed in figure 4.17. From results obtained via the temporal fitting method (Fig. 4.17a), a difference between the ellipses for K_{min} and K_{max} is observed, as expected. The same conclusions can be drawn for the frequency fitting method (Fig. 4.17b) but, generally speaking, the obtained values are lower in this second case (smaller areas and length of the major

and minor axis).

The major axis direction provides the orientation in which the highest elastic force is felt and the minor axis gives the direction in which the displacements can be done with less effort (lowest elastic force). For both fits, the minor axis seems to be aligned with the second segment of the robot while the major axis is parallel to the first segment. This seems coherent, as the forces to displace the robot along the minor axis of the ellipses apply a torque on the first joint, which means a longer lever arm since it is associated with the first segment. The force to displace the handle along the major axis produces a torque on the second joint, which has a smaller lever arm. So, for the same joint torque, larger forces are needed for a smaller lever arm. The fact that the ellipses are not aligned with the X-axis, from the expression for the orientation (Eq. 4.37), reveals the presence of non-zero non-diagonal terms causing a rotation of the ellipse.

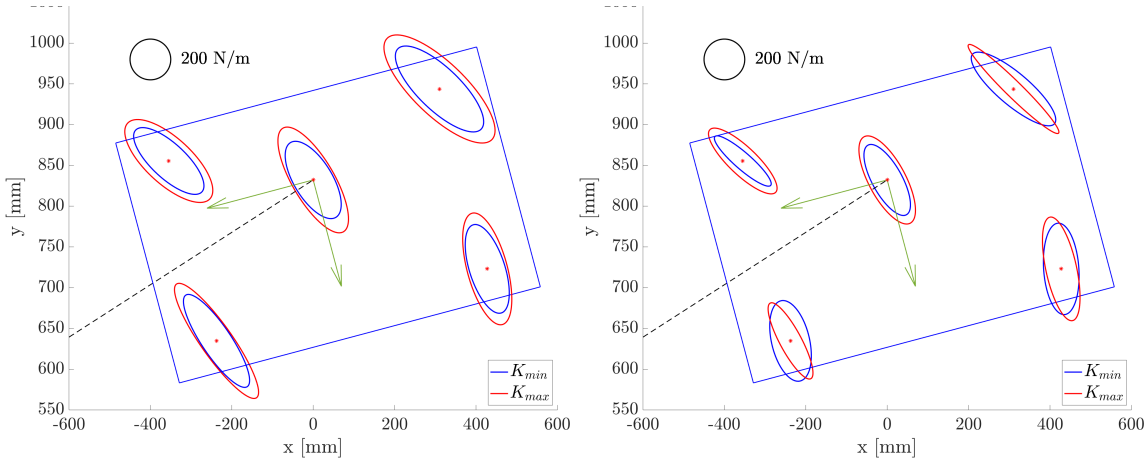

(a) Stiffness: temporal fitting

(b) Stiffness: frequency fitting

Figure 4.17: Elliptic representation of the stiffness: temporal and frequency fitting

For the ellipses representing the damping matrices, presented in figure 4.18, the aspect ratio is significantly different from what is observed for the stiffness. There is also a difference between the temporal fit technique (Fig. 4.18a) and the frequency one (Fig. 4.18b). The temporal fit results in ellipses with one major axis dominating the behaviour. The orientation of the minor and major directions are still relatively parallel to the second and to the first segment respectively.

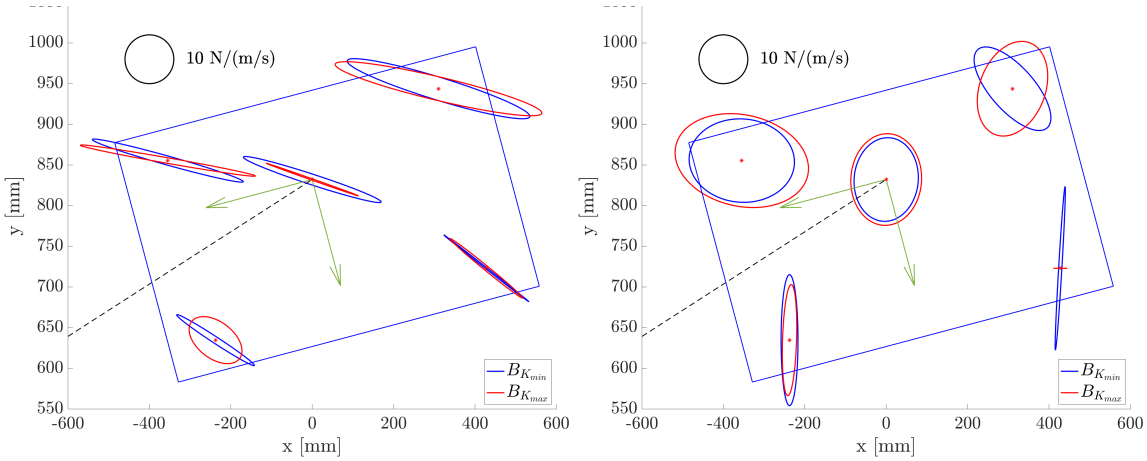

(a) Damping: temporal fitting

(b) Damping: frequency fitting

Figure 4.18: Elliptic representation of the damping: temporal and frequency fitting

Concerning the frequency fit, the results do not allow to reach the same conclusions. The ellipse orientation, as well as their aspect ratio, changes between the five points, which means that reaching a global conclusion about the behavior is less straightforward. The expected behaviour is intuitively closer to the one observed in the temporal fit, as the friction in the joints are felt at the handle to a lesser extent as the lever arm increases. Thus, for the same amount of friction torque, the first segment should induce a smaller viscous force at the handle. This is represented by the smaller axis of the ellipse being aligned along the direction perpendicular to the first segment (the one tangential to its circular motion).

It must be noted that the impact of the damping parameter is harder to interpret, as other terms related to the speed that are not modeled here could have had an impact on the results. Those could be terms related to the velocity squared, such as Coriolis forces, as well as centrifugal effects.

Finally, the elliptic representation of the mass matrices is shown in figure 4.19. The two reference circles of 0.5 kg do not have the same size, since the values obtained via the frequency fit were generally bigger than the ones obtained by the temporal fit. Both the temporal (Fig. 4.19a) and frequency (Fig. 4.19b) fitting methods provide the same aspect ratio for the five points.

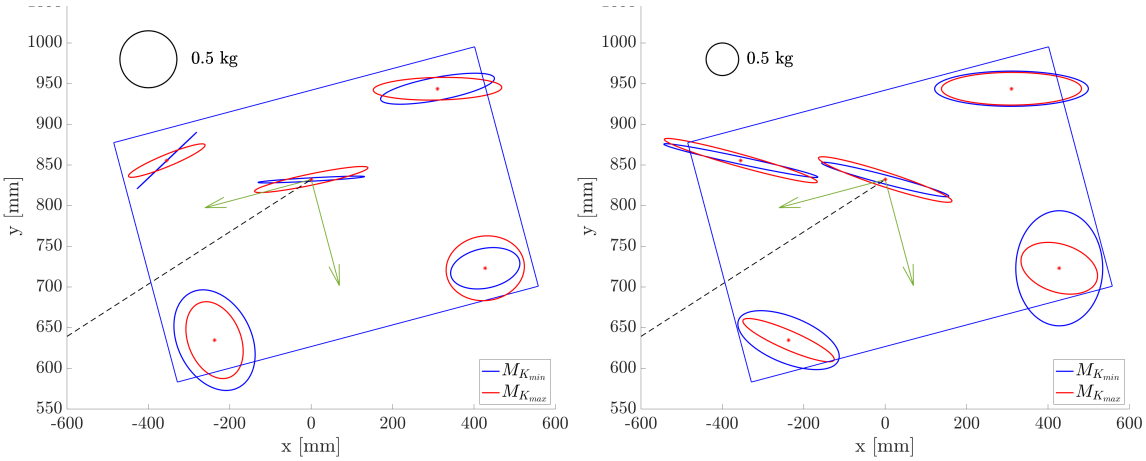

(a) Mass: temporal fitting

(b) Mass: frequency fitting

Figure 4.19: Elliptic representation of the mass: temporal and frequency fitting

Concerning the temporal fit, four of the five ellipses have their major axis oriented along the second segment. This coincides with the higher inertia component, felt when the first segment rotates and the direction of the displacement is then aligned with this major axis. In the frequency fit results, the orientation of the ellipses is slightly modified. This can be explained by the smaller difference between the diagonal and non-diagonal terms in the frequency fit than in the temporal one. For the two types of fit, the differences between the mass observed in the minimum and maximum stiffness are relatively small and could be due to noise in the measurements.

A discussion about the relevance of the observed results in the elliptic representation supported by a statistical analysis must be made. The coefficients of determination R^2 already presented previously for the central point are presented for all the points in a summary table 4.5. The temporal or frequency fit are considered to represent reality correctly if $R^2 \geq 0.75$. Values that do not respect that condition are highlighted in red. Points 2 and 4 are considered as a reference in the following discussion as their coefficient of determination R^2 is close to one.

Concerning point 1 (central point), the results for the stiffness reveal good fitting abilities with the two methods, however the description of the established model becomes rather imprecise for the maximum stiffness along the X-axis, using the temporal fit. When comparing this result in the elliptic representation with points that have better R^2 coefficient, the problem seems to comes from the damping matrix. The tendency is reversed for the central point, where the $B_{K_{max}}$ ellipse is smaller than the $B_{K_{min}}$, with respect to what is shown for points 2 and 4. Concerning the mass and stiffness ellipses, the results show similar tendency for the three points.

For point 3 (lower left corner), none of the models capture well the behavior on the X-axis. Again, this point has significant differences in terms of ellipse aspect ratio, orientation and size, for both damping and mass, with respect to points 2 and 4. Point 5, for maximum stiffness and temporal method, also exhibits lower fit accuracy when compared to the reference points. The consequence of this is a

variation in the aspect ratio of the mass ellipses.

Table 4.5: Coefficient of determination for temporal and frequency fit over the 5 studied points - min. and max. stiffness

Point		1		2		3		4		5	
Fit	Axis	Min	Max	Min	Max	Min	Max	Min	Max	Min	Max
Temp.	X	0.75	0.66	0.95	0.89	0.29	0.28	0.89	0.89	0.83	0.41
	Y	0.97	0.97	0.98	0.98	0.94	0.94	0.97	0.98	0.98	0.95
Freq.	X	0.81	0.86	0.96	0.88	0.29	0.28	0.88	0.84	0.85	0.92
	Y	0.99	0.99	0.99	0.98	0.94	0.94	0.98	0.97	0.95	0.96

General conclusions can be drawn from those elliptic representations and the statistical analysis. First, four of the five studied points achieved frequency identifications that are considered as relevant and valid to represent the robot behavior[7]. The same can be concluded for the temporal fit with a slight reservation regarding the X-axis. For one of the points, the temporal fit has very low coefficients of determination, which could be due to measurement problems. Most importantly, the elliptic representation for the stiffness for the two fitting method are significantly close and the same tendency is observed for the five points.

4.7 Summary

Understanding the behavior of a compliant robot, with a mechanical stiffness rendered via pneumatic muscles is needed in order to better describe the system as well as comprehend the system dynamics. Moreover, doing that in the Cartesian domain is relevant since it will be the domain in which the tasks will be performed. The procedure to find the mass, spring and damping matrices in the Cartesian domain from the joint domain was described and allowed to determine the mathematical constraints that should be imposed on the matrices and their values.

Then, experimental data was obtained via the robots own instrumentation through trials in which an operator moved the handle. This was done at multiple positions since the stiffness limits, as well as pressure requirements for the muscles, are not the same in different points of the workspace. This data was then post-processed so that, from the trials, data regarding force, position, speed and acceleration could be available.

From the obtained data and the dynamic equations of the system in the time domain, the parameters that best describe the system as a spring-mass-damper

[7]As a reminder, results for temporal and frequency fitting for points 2 to 5 are presented in Appendix C and D

system (in the least-squares sense and that respected the mathematical constraints) were found. It could then be stated that, for the Y-axis, these parameters captured quite accurately the behavior of the system, while for the X-axis, the fit also had good accuracy at low frequencies, but this quality was not preserved at higher frequencies.

Another approach was then proposed, performing an analysis in the frequency domain. This was accomplished using the concept of impedance and using the magnitude of the signals, from their single sided spectrum amplitude, and the frequencies. New parameters were obtained, still describing the robot as a spring-mass-damper system.

A comparison was then made between the predictions made by each model. Frequency parameters, when used to describe the system temporally, provided a less accurate estimation than the one done using the parameters obtained for the force fit. When using the temporal fit parameters in the frequency domain, the same was observed: the prediction accuracy was worse than the one obtained when using the parameters obtained via the frequency fit. It was still possible, however, to identify the similarities and differences between the parameters and overall shape of the system obtained from the two different methods.

In general, the fits are better in the Y-axis than in the X-axis. Nevertheless, the coefficients of determination for both methods are acceptable, meaning the mass-spring-damper approach manages to capture satisfactorily the dynamics of the system. Further analysis could be made by also examining the results obtained for the other investigated points.

A graphical approach was used to represent and compare the parameters identified with the two methods for the five points. Using the elliptic representation and the coefficient of determination values, it was revealed that there was a high accuracy when describing the system, specially considering the stiffness component. Three of the five points also presented acceptable description of the damping and mass components of the robot dynamics, while one of the studied point should be considered as an outlier. Considering these conclusions, it can be affirmed that the robot open loop dynamics has been mostly well captured by the approximation to a spring-mass-damper system and the stiffness values issued from the fits describe especially well the low frequency behavior.

Chapter 5

Open loop identification of the dynamic of the I/P converters

A future goal is to be able to use closed loop control to control torque and stiffness of the robot. This will be done by controlling the pressure commands sent to the muscles. As previously stated, the pressure is sent to the muscles via the I/P converters. It is therefore important to understand the dynamics of these converters. In this chapter, identification of the dynamics of the I/P converters is performed, based on the step response input. Then, the results will be discussed and a possible way to improve the feed-forward action of the system will be proposed.

5.1 Component limitations

It must be noted that the I/P converters are responsible for a major limitation of the device. The air flow is limited by their design and this causes a slow reaction time at the muscles level. In order to quantify this limitation, experiments have been done as follows. To have a reference for the inflation and deflation time without the impact of the I/Ps, the muscle was directly connected to the air supply and the 5 bar of pressure were suddenly injected by opening a mechanical valve. The time to go from the completely deflated to the maximum contraction was then measured[1]. At the end of this first part, the valve for the incoming pressure was closed with the muscle fully contracted. After that, to evaluate the deflation time without considering the impact of the I/Ps, the connecting tube was disconnected directly at the muscle output, letting all the air flow out of the muscle. The time to go from the completely contracted to completely deflated configuration was then determined.

The second step of the experiment aimed at determining the impact of the I/Ps on the inflation and deflation time. In the first instance, the muscle was connected directly to the converter's output, the time to go from the deflated to the maximum contraction state was again measured after having fully opened the air inlet of the I/P (by suddenly applying a step of pressure from 0 to 5 bar). Then, the full deflation time with the impact of the I/Ps was evaluated by measuring again the time to go

[1]For better accuracy, the free video analysis and modeling tool Tracker Online© has been used to obtain the results

from the maximum contraction to the fully deflated configuration, after having fully opened the air exhaust of the converter (by suddenly applying a step of pressure from 5 to 0 bar).

Finally, the measurement of inflation and deflation time without the I/P has been realized once again but this time with two different size of connecting tubes: one small (about 5 cm) and one long (about 1.5 m). This helped to investigate the effect of the length of the pneumatic tubes on the inflating/deflating dynamics. All the results in term of time measurement are presented in table 5.1.

Table 5.1: Experimental characterization of the I/P's limitation: measured time

Characterisation experiment		Time
Without I/P	inflation	0.737 s
	deflation	0.275 s
With I/P	inflation	2.412 s
	deflation	1.608 s
Effect of tube length increase (5 cm to 1.5 m)		<0.05 s

It is clear that the the intensity to pressure converters slow down the dynamics of inflation and deflation of the muscles. The impact is asymmetric as the inflation the time with the I/P is 3.2 times longer than without while for the deflation the time is 5.8 times longer with the I/P, but this could be expected due to the presence of hysteresis phenomena. When the converters are not used, the limiting parameter is the muscle in/output diameter of 4 mm while for the experiment with the I/P, the limiting parameters are the internal structure of the converter for the inflating time and the exhaust diameter of 1.2 mm. This is a limitation coming from the choice of the I/P converters that can be solved using a proper controller or by changing the converter by more appropriate ones. Note that the length of the pneumatic tubes has a negligible effect on the dynamics as the delay does not exceed some hundredths of a second.

5.2 Data acquisition

One useful input when performing system identification is a step input. By applying a step input and recording the system's output, one can have the evolution over time of the output and it is possible to identify the system based on the characteristics of that response. Therefore, in the framework of this experience, a reference force step was used as input and a force is measured as output, again using the robot's own instrumentation. In order to eliminate any dynamic behaviour that could arise from the robot's dynamics itself, the handle was mechanically blocked. This was done using weights on all sides of the handle, heavier than the forces that the robot was supposed to develop during the trials.

Given a geometrical configuration of the robot, two trials were conducted, impos-

ing forces in the X-axis then in the Y-axis[2]. First, a force step of absolute value 9.1 N in the X direction is used. The force reference varied first from 0 N to 27.3 N, resulting in three positive steps, and then from 27.3 N to −27.3 N, resulting in six negative steps. Then, the same procedure was applied, but with the force solicited being in the Y direction. This yielded a total of nine steps for a given position and a given axis.

This procedure was performed at nine different positions of (α_1, α_2): $(0°, 0°)$, $(0°, 15°)$, $(0°, -15°)$, $(15°, 0°)$, $(15°, 15°)$, $(15°, -15°)$, $(-15°, 0°)$, $(-15°, 15°)$, $(-15°, -15°)$. This is relevant since different positions impose different minimum stiffness, as well as different pressure value requirements for a same force step. The need to impose different stiffness values for different positions is a consequence of the results presented in chapter 3, in which it was established that, for a given position, stiffness capabilities are bounded by the torque desired at that joint.

In order to determine which stiffness value to use for each joint during the trials, the torque needed at each joint to deliver the highest reference force (in absolute value, and for each axis separately), i.e. 27.3 N and −27.3 N, is found. Then, based on the quadrilateral defined for that specific joint position and these torque values (following the procedure described in chapter 3), it is possible to find the minimum stiffness for each of those values. Finally, the highest minimum stiffness is chosen, i.e. the lowest stiffness that still allows the joint to deliver the solicited torque for all reference forces without changing the stiffness during the trials.

In summary, for each position (α_1, α_2), several step inputs were applied consecutively, meaning that the maximum/minimum force required was $\pm 3 \cdot F_{step} = \pm 27.3\text{N}$. Stiffness values for each joint were chosen based on that condition. The force output was measured using the robot's instrumentation and the step response could be obtained.

5.3 Description of the I/P dynamics as a second-order system

Methods

An example of the data obtained from the experiment is shown in figure 5.1. It indicates that the system response agrees with the expected step response of a second order system, with the presence of an overshoot and then stabilization. Therefore, a graphical approach based on that characteristic response was chosen in order to characterize the system.

For a second order system, the transfer function can be written as

$$H(s) = \frac{G\omega_n^2}{s^2 + 2\zeta\omega_n + \omega_n^2} \tag{5.1}$$

[2]For this experiment, X and Y-axis correspond to the reference frame (x_{w0}, y_{w0}) defined in chapter 2

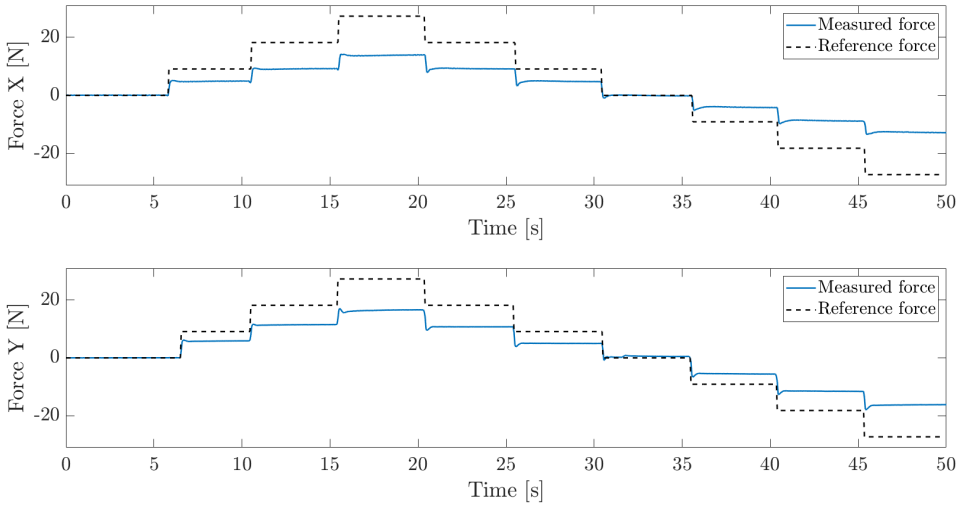

Figure 5.1: Step response for position (15°, 15°) for step forces in X and Y directions

where G is the gain, ζ is the damping ratio and ω_n is the natural frequency of the system. Given the impact of the different parameters on the step response of the system, they can be estimated graphically from this step response. Considering the example presented in figure 5.2, where y denotes the response and u denotes the step input, the parameters can be obtained as follows[39]:

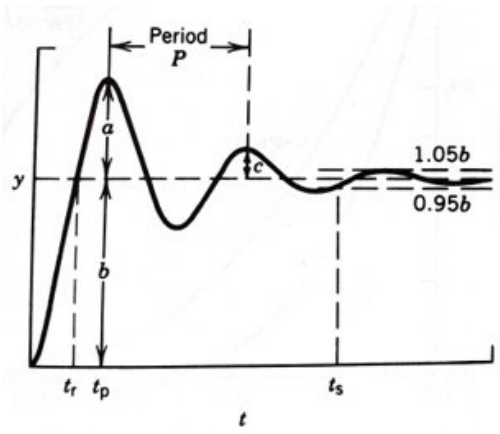

Figure 5.2: Example of the step response of a second-order system[39]

- The gain G is given by the ratio of output steady-state value to the input value, so that:

$$G = \frac{\Delta y}{\Delta u}$$

- The overshoot of the system M_p is a function of the damping ratio ζ. M_p can be graphically obtained since it is the maximum amount by which the response exceeds its steady state value (in percentage). Therefore, ζ can be obtained from this relationship and the overshoot value:

$$M_p = \frac{a}{b} \qquad \text{and} \qquad M_p = e^{\frac{-\pi\zeta}{\sqrt{1-\zeta^2}}}$$

- From the peak time t_p, time at which the overshoot occurs, and the damping ratio ζ, it is possible to estimate ω_n from:

$$t_p = \frac{\pi}{\omega_n\sqrt{1-\zeta^2}}$$

This procedure considers that the step is applied at $t_0 = 0$s. For this reason, in order to correctly estimate ω_n from the data obtained experimentally, one post-processing task had to be performed. Since the steps were applied consecutively in time, the start time ($t_{n,0}$) and end time ($t_{n,f}$) for each of the n steps had to be determined so that the offset in time could be taken into account. For the first step, $t_{1,0} = 0$s. For the second step, $t_{2,0}$ is determined as the time were the difference between two consecutive force measurements exceeds 3 N, i.e. $|F_{t_{i+1}} - F_{t_i}| > 3$ N - note that this also determines $t_{n-1,f}$ as it is the time measurement immediately before $t_{n,0}$. Using that, for each step, K, ζ and ω_n can be determined.

Results and Discussion

The estimation was done independently for F_x and F_y since two controllers with two different gains can be implemented in the future. Figure 5.3 shows an example result. From the estimated parameters, a transfer function that captures quite accurately the dynamic of the I/P converters can be obtained.

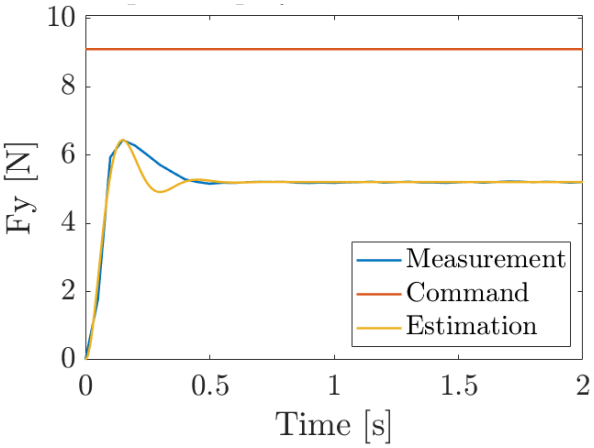

Figure 5.3: Step response - experimental and from identified transfer function

Table 5.2: Parameters values and resulting transfer function

G	0.57
ζ	0.42
ω_n [rad/s]	23.04

$$H(s) = \frac{303.8}{s^2+19.19s+530.7}$$

Ideally, it would be possible to describe the input/output force relationship using one transfer function regardless of the robot geometrical configuration. However, the results obtained via the experiments suggest otherwise. For a given position, average values describe well the system behavior. Nevertheless, between different geometrical configurations, a global average does not describe well the system. This is because the parameters vary considerably, as it can be seen in figures 5.4 and 5.5

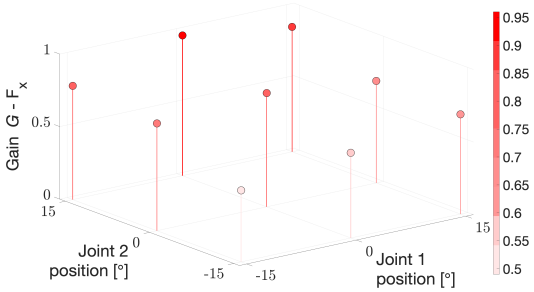

(a) Gain

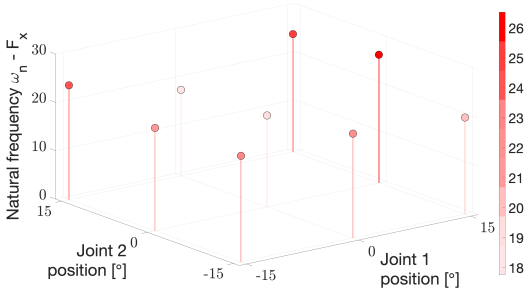

(b) Natural frequency

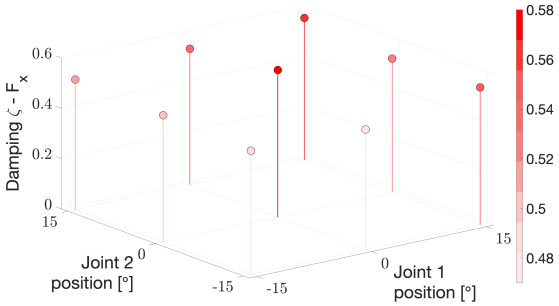

(c) Damping ratio

Figure 5.4: Parameters that describe the second order system at different geometrical configurations - X-axis force

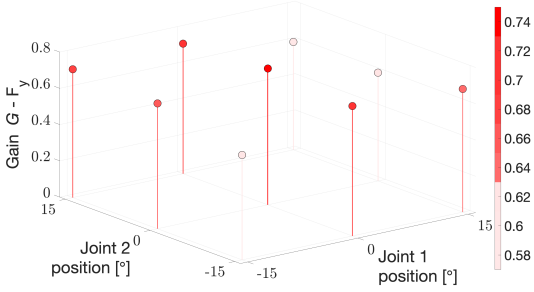

(a) Gain

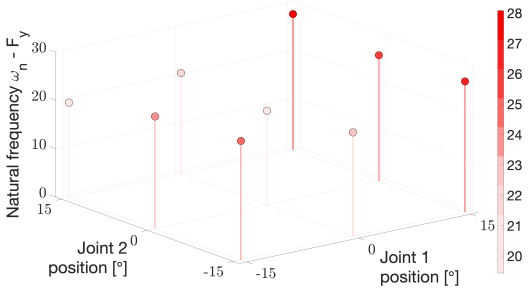

(b) Natural frequency

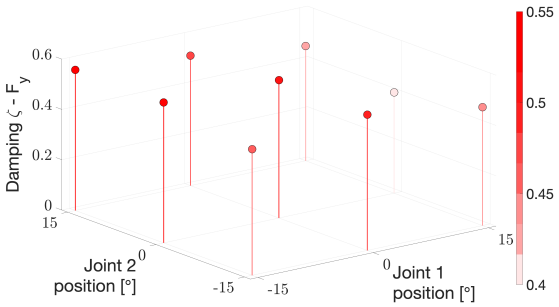

(c) Damping ratio

Figure 5.5: Parameters that describe the second order system at different geometrical configurations - Y-axis force

One plausible explanation is the fact that different positions imply different initial pressure in the muscles and also different pressure requirements to achieve the same force step. Since the force function is highly non-linear with respect to the elongation of the muscles, the pressure needed changes with a pose change. In other words, for a same force step, the pressure step does not remain constant in the workspace. This has an even bigger impact considering that the analysis is done based on a reference force in the (x_{w0}, y_{w0}) reference frame, which has to be first translated into a joint torque and then into the individual muscle forces. Again, given the highly non-linear force model - for a given joint torque, position and initial pressure in the muscle pair - the pressure step for muscle 1 is not necessarily the same that the pressure step for muscle 2 in order to obtain the desired torque.

This indicates that, ideally, different transfer functions should be considered in different geometrical configurations, but, for a given pose, the averaged parameters G, ζ and ω_n can be used to describe the system. This is illustrated in figure 5.6, in which the estimation of the step response of the system is done using a globally averaged transfer function - all parameters averaged over all positions - and a locally averaged transfer function - all parameters averaged over that specific position.

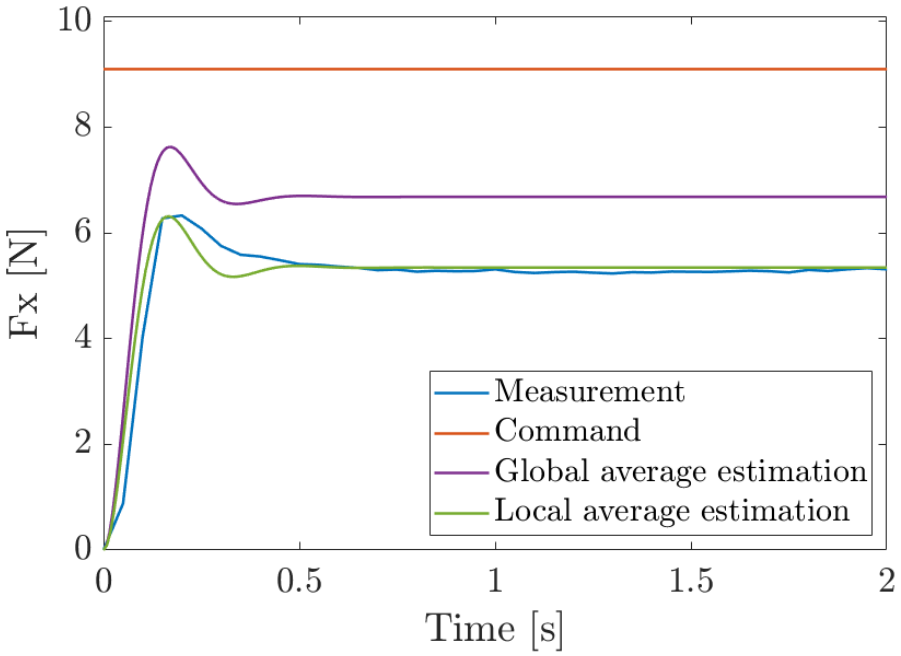

Figure 5.6: Estimation of the step response of the system based on different transfer function estimation - step applied at (0°,15°)

Given the position, however, it is then possible to estimate the gain and use this estimation to improve feed-forward action, even before the use of a closed loop controller. An approach to achieve this is described in the next section. From the values obtained for ζ and ω_n, it is also possible to have a better idea of the stabilization time of the system ($t_s = \frac{4}{\zeta\omega_n}$). For both axis, the mean stabilization time is around 0.35s. For forces in the X-axis, $t_{s,min} = 0.28$s and $t_{s,max} = 0.42$s. For

forces in the Y-axis, $t_{s,min} = 0.31$s and $t_{s,max} = 0.38$s. This highlights the limitation imposed by the dynamics of the I/P when working in open-loop conditions and the need of a closed loop. Ideally, after closing the loop, the stabilization time should be reduced by at least 1/3, i.e. $t_s \approx 0.1$s.

5.4 Feed-forward improvement using command correction based on gain estimation

Methods

One possible way to try to bring the steady-state value of the force closer to the desired one, without yet implementing any specific controller, is by applying a correction on the command. This could improve the feed-forward action that defines the command in function of the desired force.

Since the gain depends on position, this cannot be done with a constant offset. To capture this dependency, the plane that better approximates the gain-position relationship can be found. This is done separately for forces along the X and Y directions. The result can be expressed as:

$$G_{F,fit} = p_1\alpha_1 + p_2\alpha_2 + p_3 \tag{5.2}$$

The parameters p_1, p_2 and p_3 are the ones that best approximate the data, in the least-squares sense. This 2D planar form has been chosen intuitively based on the observation of the gains obtained in figures 5.4a and 5.5a. It is a quite arbitrary choice that could be adapted to improve the performances in the future. Then, based on the surface equation, the correction factor to be applied to the command can be found.

Results and Discussion

The fits are presented in figure 5.7a and 5.7b for the X and Y forces respectively.

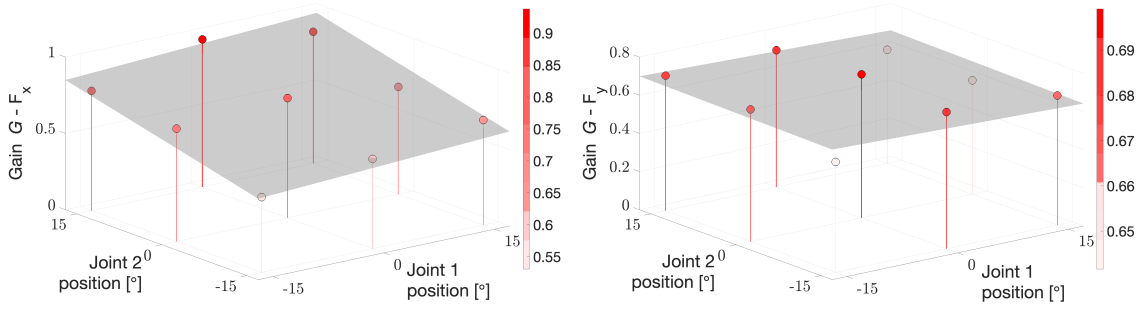

(a) Gain X-axis force

(b) Gain X-axis force

Figure 5.7: 2D planar fit of the gain parameter of the system transfer function

The idea is then to bring the gains on the X-axis and Y-axis forces to one in order to change the command so that the measured force would be equivalent to the desired one. To do so, the previous command inducing the static error observable in figures 5.6 must be locally multiplied by inverse of the fitted value of the gain $\frac{1}{G_{F,fit}}$. This allows to bring the gains on F_X and F_Y in figure 5.7a and 5.7b to one, thus correcting the command. Since the estimation is not perfect, there is still a need for a controller in closed loop, that will remove any residual static error. However, applying this correction on the feed-forward action could already improve the results, as well as the overall performance of the final controller.

5.5 Summary

During rehabilitation tasks, closed-loop control is interesting in order to guarantee that the desired torque and stiffness are being delivered, so to enhance the rehabilitation process. Considering that objective, identifying the dynamic of the converters allows better understanding of the open-loop behavior and limitations of this part of the system, as well as possibly helping in the design of a closed-loop controller.

Having that in mind, an experiment was made in order to determine the transfer function between an input reference force and the output measured force. Several points in the workspace were chosen since pressure requirements for a same force step do not remain constant. This is due to the highly non-linear force relationship for the pneumatic muscles. Force steps were then applied to the robot and the step response was recorded.

Given step responses similar to those of second order systems, a graphical approach, in order to determine the parameters that describe this type of systems, was performed. For a given position, the same force step, even at different offset levels, corresponded to parameters that were close enough so that the averaged parameters provide a good approximation of the system. Between different positions, this did not hold, which means that simply averaging the parameters obtained for all trials does not provide a transfer function that captures well the behaviour of the system.

A possible strategy to improve the open loop behavior, in order to reduce the steady-state error, was proposed. It consists in finding the plane that best approximates the gain in function of the position, using the results from the nine measured configurations. The obtained expression provides the correction factor by which the command should be multiplied, in function of the position, and can be used for all possible geometrical configurations.

The plane does not approximate perfectly the gain distribution so a closed loop controller is still needed in order to eliminate any remaining static error. Also, the stabilization time is too slow, on average around 0.35s. The closed loop controller should then be developed in order to reduce this time to at least 0.1s.

Chapter 6

Conclusion & Perspectives

The following chapter will depict the contribution of the thesis to the field of rehabilitation robots actuated by pneumatic artificial muscles. The main results obtained for the studies performed will be summarised as well as the process that has been followed and the limits which have been identified. Then, a perspective for the continuation of the project and possible improvements in the methodology and mechanical design will be discussed.

6.1 Conclusion

First, a state of the art of the research areas related to post-stroke rehabilitation has demonstrated the relevance of using robots in therapies. Pneumatic artificial muscles have some advantages: they are intrinsically compliant and thus safer, have high power to weight ratio, have inherent similarities with the human skeletal muscles and are low-cost. This made them good candidates for research on a less common actuation technique that could be applied to the medical field. Even if some disadvantages, such as a less precise control and a noisy behaviour, hinder their marketing, the interest in those actuators and their application in robotics remains high. Therefore, it has been decided to continue what was developed in a previous master thesis.

Then, a description of the robot and its mechanical redesign was presented. The frame used to represent the results was also defined. It is fixed, with its origin inside the final rectangular workspace and the axes aligned with the sides of that rectangle. The principle of actuation was explained and it consists in using a muscle pair, connected via cables to a pulley, to implement joint rotations.

The model for the muscle force as a function of the pressure and its elongation developed in [4] was verified, considering now the muscles in their working configuration. The validated model was then used to obtain the torque and stiffness limits of the two joints of the robot. For each angular configuration, a locus representing this limits can be obtained. This locus represents the limit conditions when considering the pressure limits. The maximum achievable torques for the two joints depend on the angles

made by the segments, however a range of achievable torques for the whole workspace could be obtained. Joint one is able to achieve a range of $[-31.5, 31.5]$ Nm and joint two $[-22, 22]$ Nm. The limit stiffness at zero torque can be described by two curves, one representing the minimum and the other, the maximum, over the position range. It was identified that the range narrows as one moves away from the central configuration, this being explained by the imposed limit of 5 bar in the muscles and additional constraints in pressure when moving from the center position in order to keep the pose of the robot. The lowest achievable joint stiffness is when the robot is in neutral position. Those conclusions are relevant for the future application of the robot as they can guide the design the rehabilitation tasks based on the capabilities of the device and serve as information for the physiotherapist in charge of the therapeutic program.

An identification of the system when operating in open loop was performed, in order to better describe the system as well as comprehend its dynamics. The robot was modelled as spring-mass-damper system and results were given in the central reference frame defined. In order to do that, constraints on the matrices K_C, B_C and M_C, from their respective equivalents in the joint domain, were found. Then, different experiments allowed us to obtain the necessary data that was used to find the parameters that describe the system. Two models were developed: one with K_C, B_C and M_C matrices with parameters based in the dynamic equations in the time domain and one with parameters derived from a fit in the frequency domain, using the impedance concept. The quality of the fits was evaluated using the R^2 coefficient and a comparison was done between both approaches.

Overall, both fits provide models with acceptable accuracy, and the system indeed behaves as a classical spring-mass-damper system. However, at higher frequencies and speeds, the quality of the fit was worse. Considering that the stiffness capabilities are not the same for the whole workspace, the results obtained at different points were also compared, considering both models. In order to do that, a graphical representation of the matrices was done using ellipses.

From those ellipses along with a statistical analysis, the results verified the accurate description of the stiffness component provided by the fitting methods. Moreover, the mass and damping behaviour are also correctly captured using the fit for three of the five studied points. Considering those conclusions, it can be affirmed that the robot open loop dynamics is mostly well captured by a mass-spring-damper system over the entire workspace, but that those matrices do not remain constant for different positions.

In the final chapter, the open-loop identification of the I/P converters was performed. This was done in order to better understand the behaviour of the actuators. As presented in the chapter, the converters are responsible for a limitation of the performance of the system in open-loop, specially in terms of response time. Also, given the overall principle of actuation of the robot, the same force requirement in different geometrical configurations does not represent the same pressure requirement. Therefore, this open-loop identification helps better understand those limitations, as

well as the differences in the output force when the pose of the robot is changed.

The step response of the system in open loop was similar to the one observed for second order systems. Therefore, an approach graphically identifying the parameters that describe this type of systems was used. It was discovered that, for a given position, the transfer function could be approximated as the average of the trials at that position. However, it was not possible to derive an unique transfer function for all positions.

In order to reduce the static error still in open loop, it is possible to apply a correction to the command. Since the transfer function (and its gain) changes, a unique offset would not be effective. The gain in function of the position was then modelled as a plane. This approximation could be used to improve the feed-forward action, represented by the pressure command when trying to deliver a certain force. There is still a need of a closed loop controller in order to correct potential remaining static errors, since the plane is not a perfect approximation. This closed loop is also needed in order to improve the stabilization time of the system, which is on average 0.35s and should ideally be at least 0.1s.

Overall, the results of this work help to better understand the robot global behavior, from the position dependent limitations in torque and stiffness to the accurate description of the robot as a mass-spring-damper system. The identification of the second-order system parameters that describe the converters dynamics, also pose dependent, provide valuable information for future design of a closed loop controller. Associating the device with said closed loop controller is the next milestone to be achieved.

6.2 Perspectives

Even if a mechanical redesign has been carried out and satisfactory results were obtained, the project to which this thesis has contributed is not yet complete. First of all, there are still some minor improvements that can be achieved.

The cable of the first joint still slides into the pulley groove when large sudden changes in pressure are applied to the segment or when the arm gets close to the limit of its angular range. This is explained by a tightening problem of the bolts responsible for securing the metallic part added to maintain the cable in place. This is caused by the rotation of the nut in its pocket designed in the Onyx 3D printed part. The edges of hexagonal shape that was 3D-printed became rounded due to the force applied when tightening the bolts. This problem could be solved by reprinting the part with reinforcement around the hexagonal pocket or with a different solution to ensure the clamping of the cable.

The carrier ball supporting the handle has been changed to reduce the friction with the table and to avoid blocking at time. The new carrier ball improved those two aspects, however, the friction is still quite noticeable. Depending on the rehabilitation

needs this could maybe be accepted but it must be kept in mind that an alternative solution could be necessary in the future.

In what concerns the control of the robot, the current work showed a need to implement a closed loop controller. Therefore, a controller should be designed in order to both cancel the static error and reduce the system reaction time. As previously stated, the I/P converters could be a limiting component to the improvement of the temporal performances of the closed loop controller. It could thus be necessary to change those hardware components if time requirements cannot be met after the implementation of the closed loop controller.

In order to comply with the faster stabilization time requirement, one major change needs to be made concerning the interface between electronics and the robot, done using *LabView*. The governing loop runs at around $30 \sim 40$ ms, but ideally it should run at, at least, 10 ms in order to guarantee good performance of the controller.

This list highlights the more immediate steps following this work. It is non-exhaustive and can be completed or improved in function of future developments of the research.

Epilogue

A year after the beginning of this demanding and long-term project combining various skills, we are proud to conclude the accomplishment of our last year at the university as students. This thesis has brought us many learnings in how to conduct a nine month project, and required performing experimental processes as well as rigorous technical and bibliographical research, theoretical development and synthesis work.

This work, combining mechanical design, control methods and system identification techniques, all of this related to the medical field, was rewarding. We learned a lot about the medical aspects of stroke, the existing technologies and the benefits they can provide to this very demanding world. A project combining transversal skills in the medical and engineering domains is challenging and very stimulating and we were thus continuously fascinated and enjoying the work to accomplish.

The benefits of a such thesis combining theoretical knowledge, experimentation and reflection, as well as adaptations depending on changing objectives regarding the evolution of the work and the unforeseen events, are essential to prepare ourselves for our future careers. We also discovered a less common actuation principle, its inherent physics and how it can contribute to improve the medical therapies, as well as other more common actuation methods. This helped us realize how research brings progress and how it is primordial for the future of medical treatments.

Next to the more scientific contributions of the thesis, we also developed organisational skills using Gantt charts, weekly meetings and debriefings. We learned how to identify and formulate objectives and how to determine the most appropriate approach to treat a problem. All of this helped us to achieve the multiples goals defined all year long.

The project has not ceased to arouse our interest and we hope it will have a future. We would be pleased to follow or participate in its coming evolution, to see what the patient interactions will bring and observe the contribution we brought have a real impact on tomorrow's post-stroke rehabilitation.

References

[1] S. Virani *et al.*, *Heart disease and stroke statistics—2021 update: a report from the American Heart Association*, on behalf of the American Heart Association Council on Epidemiology and Prevention Statistics Committee ans Stroke Statistics Subcommittee, January 27 2021, doi: 10.1161/CIR.0000000000000950.

[2] C. W. Tsao *et al.*, "Heart disease and stroke statistics 2014;2022 update: A report from the american heart association," *Circulation*, vol. 145, no. 8, pp. e153–e639, 2022. [Online]. Available: https://www.ahajournals.org/doi/abs/10.1161/CIR.0000000000001052

[3] N. I. of Neurological Disorders and Stroke, "Post-stroke rehabilitation fact sheet," Online published fact sheet referenced as NIH Publication 20-NS-4846, April 2020.

[4] E. Koob, "Modelling and control of a post-stroke robot activated by pneumatic artificial muscles for upper-limb rehabilitation," Master's thesis, Catholic University of Louvain, 2021.

[5] F. Khan, S. Karthikbabu, and W.-P. Teo, "Upper limb rehabilitation post-stroke," Proposed Research Topic at Frontiers, 2022.

[6] L. M. Allen, A. N. Hasso, J. Handwerker, and H. Farid, "Sequence-specific mr imaging findings that are useful in dating ischemic stroke," *RadioGraphics*, vol. 32, no. 5, pp. 1285–1298, 2012, https://doi.org/10.1148/rg.325115760.

[7] J. Kaiser, "Neurorehabilitation using plasticity and growth as a therapeutic tool," *Burke Neurological Institute*, 2020.

[8] M. Puderbaugh and P. D. Emmady, *Neuroplasticity*. StatPearls Publishing, 2022, pMID: 32491743.

[9] M. Maier, B. R. Ballester, and P. F. M. J. Verschure, "Principles of neurorehabilitation after stroke based on motor learning and brain plasticity mechanisms," *Frontiers in systems neuroscience*, vol. 13, no. 74, 2019, doi:10.3389/fnsys.2019.00074.

[10] H. M. Van der Loos, D. J. Reinkensmeyer, and E. Guglielmelli, *Rehabilitation and Health Care Robotics*. Cham: Springer International Publishing, 2016, pp. 1685–1728. [Online]. Available: https://doi.org/10.1007/978-3-319-32552-1_64

[11] C. Frumento, E. Messier, and V. Montero, "History and future of rehabilitation robotics," An Interactive Qualifying Project Report submitted to the Faculty of Worcester Polytechnic Institute in partial fulfillment of the requirements for the Degree of Bachelor of Science, 2010.

[12] Q. Meng, Q. Xie, and H. Yu, "Upper-limb rehabilitation robot: State of the art and existing problems," in *Proceedings of the 12th International Convention on Rehabilitation Engineering and Assistive Technology*, 2018, pp. 155–158.

[13] A. Jebri, T. Madani, and K. Djouani, "Adaptive continuous integral-sliding-mode controller for wearable robots: Application to an upper limb exoskeleton," vol. 2019, 06 2019, pp. 766–771.

[14] E. Ambrosini and other, "The combined action of a passive exoskeleton and an emg-controlled neuroprosthesis for upper limb stroke rehabilitation: First results of the retrainer project," in *2017 International Conference on Rehabilitation Robotics (ICORR)*, 2017, pp. 56–61.

[15] Hocoma, "Armeo power," 2016.

[16] S. Balasubramanian, R. Wei, M. Perez, B. Shepard, E. Koeneman, J. Koeneman, and J. He, "Rupert: An exoskeleton robot for assisting rehabilitation of arm functions," in *2008 Virtual Rehabilitation*, 2008, pp. 163–167.

[17] E. T. Wolbrecht, D. J. Reinkensmeyer, and J. E. Bobrow, "Pneumatic control of robots for rehabilitation," *The International Journal of Robotics Research*, vol. 29, no. 1, pp. 23–38, 2010.

[18] Axinesis, "Reaplan," 2021.

[19] A. Song, L. Pan, G. Xu, and H. Li, "Impedance identification and adaptive control of rehabilitation robot for upper-limb passive training," in *Foundations and Applications of Intelligent Systems*, F. Sun, T. Li, and H. Li, Eds. Berlin, Heidelberg: Springer Berlin Heidelberg, 2014, pp. 691–710.

[20] T. Paolucci *et al.*, "Robotic rehabilitation for end-effector device and botulinum toxin in upper limb rehabilitation in chronic post-stroke patients: an integrated rehabilitative approach," *Neurol Sci*, vol. 42, no. 12, 2021.

[21] L. Zhang, S. Guo, and Q. Sun, "Development and assist-as-needed control of an end-effector upper limb rehabilitation robot," *Applied Sciences*, vol. 10, no. 19, 2020. [Online]. Available: https://www.mdpi.com/2076-3417/10/19/6684

[22] F. Daerden and D. Lefeber, "Pneumatic artificial muscles: actuators for robotics and automation," *European Journal of Mechanical and Environmental Engineering*, vol. 47, 03 2002.

[23] J. Legrand, M. Ourak, and E. Vander Poorten, "Concentric muscles - miniature pneumatic actuator with integrated channel for surgical instruments," 02 2021.

[24] D. Villegas, M. V. Damme, B. Vanderborght, P. Beyl, and D. Lefeber, "Third–generation pleated pneumatic artificial muscles for robotic applications: Development and comparison with mckibben muscle," *Advanced Robotics*, vol. 26, no. 11-12, pp. 1205–1227, 2012. [Online]. Available: https://doi.org/10.1080/01691864.2012.689722

[25] Festo, "Fluidic muscle dmsp/mas," Catalog/datasheet, 2017.

[26] B. Tondu and P. Lopez, "Modeling and control of mckibben artificial muscle robot actuators," *IEEE Control Systems Magazine*, vol. 20, no. 2, pp. 15–38, 2000.

[27] B. Tondu, S. Ippolito, J. Guiochet, and A. Daidié, "A Seven-degrees-of-freedom Robot-arm Driven by Pneumatic Artificial Muscles for Humanoid Robots," *The International Journal of Robotics Research*, vol. 24, no. 4, pp. p.257–274, 2005. [Online]. Available: https://hal.archives-ouvertes.fr/hal-01292939

[28] T. Tsuji and Y. Tanaka, "Bio-mimetic impedance control of robotic manipulator for dynamic contact tasks," *Robotics and Autonomous Systems*, vol. 56, no. 4, pp. 306–316, 2008. [Online]. Available: https://www.sciencedirect.com/science/article/pii/S0921889007001133

[29] J. M. Dolan, M. B. Friedman, and M. L. Nagurka, "Dynamic and loaded impedance components in the maintenance of human arm posture," *IEEE Transactions on Systems, Man, and Cybernetics*, vol. 23, no. 3, pp. 698–709, May-June 1993, doi: 10.1109/21.256543.

[30] P. Artemiadis, P. Katsiaris, M. Liarokapis, and K. Kyriakopoulos, "Human arm impedance: Characterization and modeling in 3d space," 10 2010.

[31] T. Noritsugu and T. Tanaka, "Application of rubber artificial muscle manipulator as a rehabilitation robot," *IEEE/ASME Transactions on Mechatronics*, vol. 2, no. 4, pp. 259–267, 1997.

[32] A. Hošovský, J. Piteľ, K. Židek, M. Tóthová, J. Sárosi, and L. Cveticanin, "Dynamic characterization and simulation of two-link soft robot arm with pneumatic muscles," *Mechanism and Machine Theory*, vol. 103, pp. 98–116, 2016. [Online]. Available: https://www.sciencedirect.com/science/article/pii/S0094114X16300477

[33] MATLAB, *version 9.7.0 (R2019b)*. Natick, Massachusetts: The MathWorks Inc., 2019.

[34] D. Caldwell, G. Medrano-Cerda, and M. Goodwin, "Control of pneumatic muscle actuators," *Control Systems, IEEE*, vol. 15, pp. 40 – 48, 03 1995.

[35] L. . A. programming techniques, *2018*. National Instruments, 2018.

[36] C. English and D. Russell, "Representations of multi-joint stiffness for prosthetic limb design," *Mechanism and Machine Theory*, vol. 43, pp. 297–309, 03 2008.

[37] M. J. Hollerbach and T. Flash, "Dynamic interactions between limb segments during planar arm movement," *Biological Cybernetics*, vol. 44, no. 1, pp. 67–77, 1982, doi: 10.1007/BF00353957.

[38] R. Bartlett, *Introduction to Sports Biomechanics Analysing Human Movement Patterns*. Routledge, 2007, p. 136.

[39] D. E. Seborg, etc., T. R. Edgar, and D. A. Mellichamp, *Process dynamics and control*. Brisbane, QLD, Australia: John Wiley and Sons (WIE), 1989.

Appendices

Appendix A

Jacobian operator of a SCARA robot with 2 DoFs and reference frame changes

The Jacobian operator can be obtained from the direct geometric model. The relationship between different reference frames can be found using the Denavit-Hartenberg convention to obtain a transformation matrix that brings us from the end-effector frame to the base frame.

A 2 DoFs SCARA robot is then shown in figure 1.1.

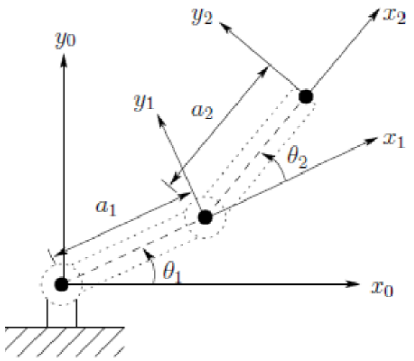

Figure 1.1: 2 DoFs SCARA robot conventions

Link	θ	d	a	α
1	θ_1*	0	a_1	0
2	θ_2*	0	a_2	0

Table A.1: Variables for the Denavit-Hartenberg convention

Using the Jacobian operator, it is possible to find the torque at the joints from the forces in the reference frame as:

$$\tau_{1,2} = J^T F_{x_0,y_0} \tag{A.1}$$

Finally, if considering specifically the robot studied in this thesis, some adaptation is needed. First, the θ angles do not correspond to the α angles measured by the encoders. A variable change is needed and is given by:

$$\begin{cases} \theta_1 = \theta_{1,init} + \alpha_1 \\ \theta_2 = \theta_{2,init} + \alpha_2 \end{cases} \tag{A.2}$$

where $\theta_{i,init}$ represents the initial angular position of joint i with respect to the the original reference frame $i-1$. For the initial configuration considered in this work, $\theta_{1,init} = \frac{\pi}{2} + arctan(\frac{L2}{L1})$ and $\theta_{2,init} = -\frac{\pi}{2}$. This variable change is needed in order to obtain the correct Jacobian operator from the measured angles.

A transformation is also needed in order to have the forces expressed in the correct frame (XY-base frame). This is needed since the force measured by the sensor are expressed in the end-effector frame.

First, the transition matrices between the frames can be expressed as [1]:

$$ {}^{0}H_1 = \begin{pmatrix} C_{\theta_1} & -S_{\theta_1}C_{\alpha_1} & S_{\theta_1}S_{\alpha_1} & a_1C_{\theta_1} \\ S_{\theta_1} & C_{\theta_1}C_{\alpha_1} & -C_{\theta_1}S_{\alpha_1} & a_1S_{\theta_1} \\ 0 & S_{\alpha_1} & C_{\alpha_1} & d_1 \\ 0 & 0 & 0 & 1 \end{pmatrix} \tag{A.3} $$

$$ {}^{1}H_2 = \begin{pmatrix} C_{\theta_2} & -S_{\theta_2}C_{\alpha_2} & S_{\theta_2}S_{\alpha_2} & a_2C_{\theta_2} \\ S_{\theta_2} & C_{\theta_2}C_{\alpha_2} & -C_{\theta_2}S_{\alpha_2} & a_2S_{\theta_2} \\ 0 & S_{\alpha_2} & C_{\alpha_2} & d_2 \\ 0 & 0 & 0 & 1 \end{pmatrix} \tag{A.4} $$

The transition matrix from the end effector to the reference frame is then:

$$ {}^{0}H_2 = {}^{0}H_1 \cdot {}^{1}H_2 = \begin{pmatrix} C_{12} & -S_{12} & 0 & a_2C_{12} + a_1C_{\theta_1} \\ S_{12} & C_{12} & 0 & a_2S_{12} + a_1S_{\theta_1} \\ 0 & 0 & 1 & 0 \\ 0 & 0 & 0 & 1 \end{pmatrix} \tag{A.5} $$

The Jacobian matrix for the two joints is then expressed by:

$$ J = \begin{pmatrix} z_0 \times (O_2 - O_0) & z_1 \times (O_2 - O_1) \\ z_0 & z_1 \end{pmatrix} \tag{A.6} $$

With:

$$ z_1 = z_2 = \begin{pmatrix} 0 \\ 0 \\ 1 \end{pmatrix} \quad ; \quad O_0 = \begin{pmatrix} 0 \\ 0 \\ 0 \end{pmatrix} $$

$$ O_1 = \begin{pmatrix} a_1C_{\theta_1} \\ a_1S_{\theta_1} \\ 0 \end{pmatrix} \quad ; \quad O_0 = \begin{pmatrix} a_2C_{12} + a_1C_{\theta_1} \\ a_2S_{12} + a_1S_{\theta_1} \\ 0 \end{pmatrix} $$

The Jacobian matrix can be found:

$$ J = \begin{pmatrix} -a_1S_{\theta_1} - a_2S_{12} & a_2S_{12} \\ a_1C_{\theta_1} + a_2C_{12} & a_2C_{12} \\ 0 & 0 \\ 0 & 0 \\ 0 & 0 \\ 1 & 1 \end{pmatrix} \tag{A.7} $$

[1] For the following developments $C_{\theta_i} = cos(\theta_i)$, $S_{\theta_i} = cos(\theta_i)$, $C_{12} = cos(\theta_1 + \theta_2)$ and $S_{12} = sin(\theta_1 + \theta_2)$

The last thing to do is to apply the transformation between the force in the end-effector and reference frame.

$$F_{x_0,y_0} = {}^0R_2 \; F_{x_2,y_2} \tag{A.8}$$

Where

$${}^0R_2 = \begin{pmatrix} C_{12} & -S_{12} & 0 \\ S_{12} & C_{12} & 0 \\ 0 & 0 & 1 \end{pmatrix} \tag{A.9}$$

Appendix B

Full mathematical development for model based characterization

The torque and stiffness developed at a given joint can be expressed as:

$$\tau = R(F_2(\varepsilon_2, P_2) - F_1(\varepsilon_1, P_1)) \tag{B.1}$$

$$K = -\frac{\partial \tau}{\partial \alpha} = -R(\frac{F_2(\varepsilon_2, P_2)}{\partial \alpha} - \frac{F_1(\varepsilon_1, P_1)}{\partial \alpha}) \tag{B.2}$$

where $F_i(\varepsilon_i, P_i)$ is the force developed by pneumatic muscle i and is described by the 5^{th}-order polynomial experimental model

$$\begin{aligned} &F(\varepsilon, P) = aP\varepsilon^4 + bP\varepsilon^3 + cP\varepsilon^2 + dP\varepsilon + e + f\varepsilon^5 + g\varepsilon^4 + h\varepsilon^3 + i\varepsilon^2 + j\varepsilon + k \\ &\text{or} \\ &F(\varepsilon, P) = A(\varepsilon)P + B(\varepsilon), \text{ where } A(\varepsilon) = a\varepsilon^4 + b\varepsilon^3 + c\varepsilon^2 + d\varepsilon + e \text{ and} \\ &B(\varepsilon) = f\varepsilon^5 + g\varepsilon^4 + h\varepsilon^3 + i\varepsilon^2 + j\varepsilon + k \end{aligned} \tag{B.3}$$

Since the force is a function of ε, which, for a pair of muscles, is given by

$$\begin{cases} \varepsilon_1 = \varepsilon_0 - \frac{R\alpha}{l_0} \\ \varepsilon_2 = \varepsilon_0 + \frac{R\alpha}{l_0} \end{cases} \tag{B.4}$$

it can be clearly observed that torque and stiffness capabilities depend on joint configuration. Furthermore, using the above relationship between ε and α, it is also possible to rewrite the stiffness equation as

$$\begin{aligned} &K = -\tfrac{R^2}{l_0}(\tfrac{\partial F_2}{\partial \varepsilon_2} + \tfrac{\partial F_1}{\partial \varepsilon_1}) \text{ where } \tfrac{\partial F}{\partial \varepsilon} = \tfrac{\partial A}{\partial \varepsilon}P + \tfrac{\partial B}{\partial \varepsilon} = C(\varepsilon)P + D(\varepsilon), \text{ with} \\ &C(\varepsilon) = 4a\varepsilon^3 + 3b\varepsilon^2 + 2c\varepsilon + d \text{ and } D(\varepsilon) = 5f\varepsilon^4 + 4g\varepsilon^3 + 3h\varepsilon^2 + 2i\varepsilon + j \end{aligned} \tag{B.5}$$

.

Finally, the explicit expression for torque and stiffness for a given configuration is:

$$\tau = R(A(\varepsilon_2)P_2 + B(\varepsilon_2) - A(\varepsilon_1)P_1 - B(\varepsilon_1)) \tag{B.6}$$

$$K = -\frac{R^2}{l_0}(C(\varepsilon_1)P_1 + D(\varepsilon_1) + C(\varepsilon_2)P_2 + D(\varepsilon_2)) \tag{B.7}$$

Then, we can either impose (P_1, P_2) and obtain torque and stiffness (direct model) or impose desired (K, τ) and find the needed pressure pair (inverse model). To invert the model, an expression for P_1 can be obtained from B.7:

$$P_1 = \frac{K + \frac{R^2}{l_0} D(\varepsilon_1) + \frac{R^2}{l_0} D(\varepsilon_2)}{C(\varepsilon_1)} + \frac{\frac{R^2}{l_0} C(\varepsilon_2) P_2}{C(\varepsilon_1)} \tag{B.8}$$

Then, it is possible to use this expression for P_1 in equation B.6 , in order to obtain an expression for P_2 which is independent from P_1:

$$\frac{\tau}{R} = A(\varepsilon_2)P_2 + B(\varepsilon_2) - A(\varepsilon_1)\left[\frac{K + \frac{R^2}{l_0} D(\varepsilon_1) + \frac{R^2}{l_0} D(\varepsilon_2)}{C(\varepsilon_1)} + \frac{\frac{R^2}{l_0} C(\varepsilon_2) P_2}{C(\varepsilon_1)}\right] - B(\varepsilon_1)$$

$$P_2 = \frac{\frac{\tau}{R} + B(\varepsilon_1) + A(\varepsilon_1)\left[\frac{K + \frac{R^2}{l_0} D(\varepsilon_1) + \frac{R^2}{l_0} D(\varepsilon_2)}{C(\varepsilon_1)} + \right] - B(\varepsilon_2)}{A(\varepsilon_2) - A(\varepsilon_1)\left[\frac{\frac{R^2}{l_0} C(\varepsilon_2)}{C(\varepsilon_1)}\right]} \tag{B.9}$$

Finally, the value obtained for P_2 can be used in equation B.8 to obtain P_1

Appendix C

Result for points 2 to 5 - temporal fit

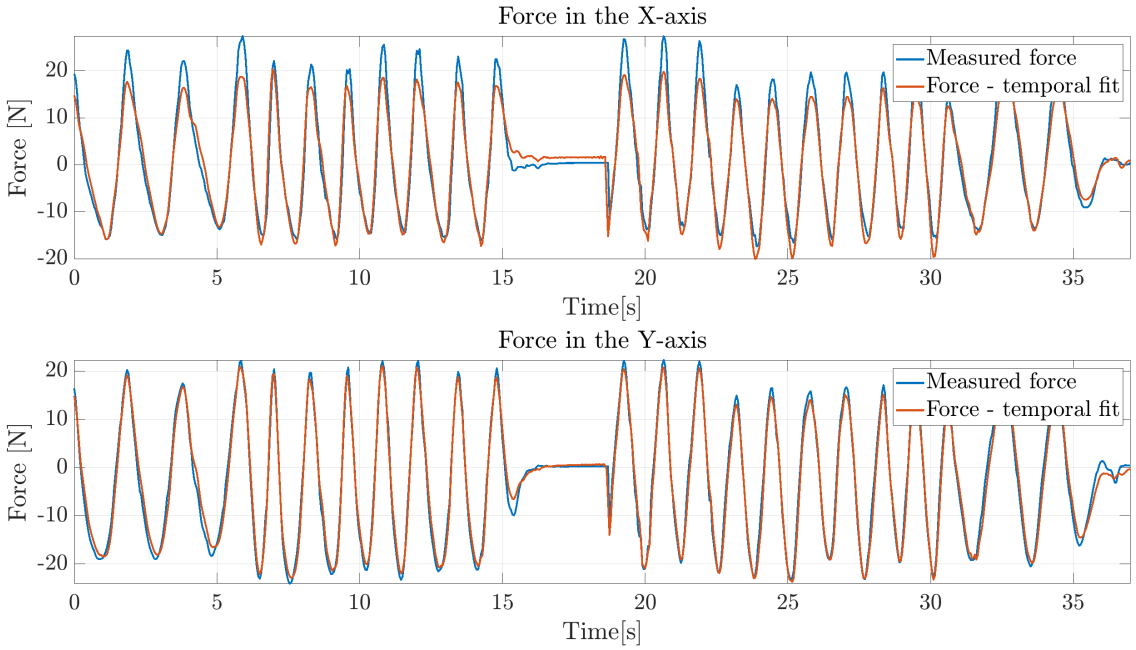

Figure 3.1: Measured and computed forces for point 2, minimum stiffness

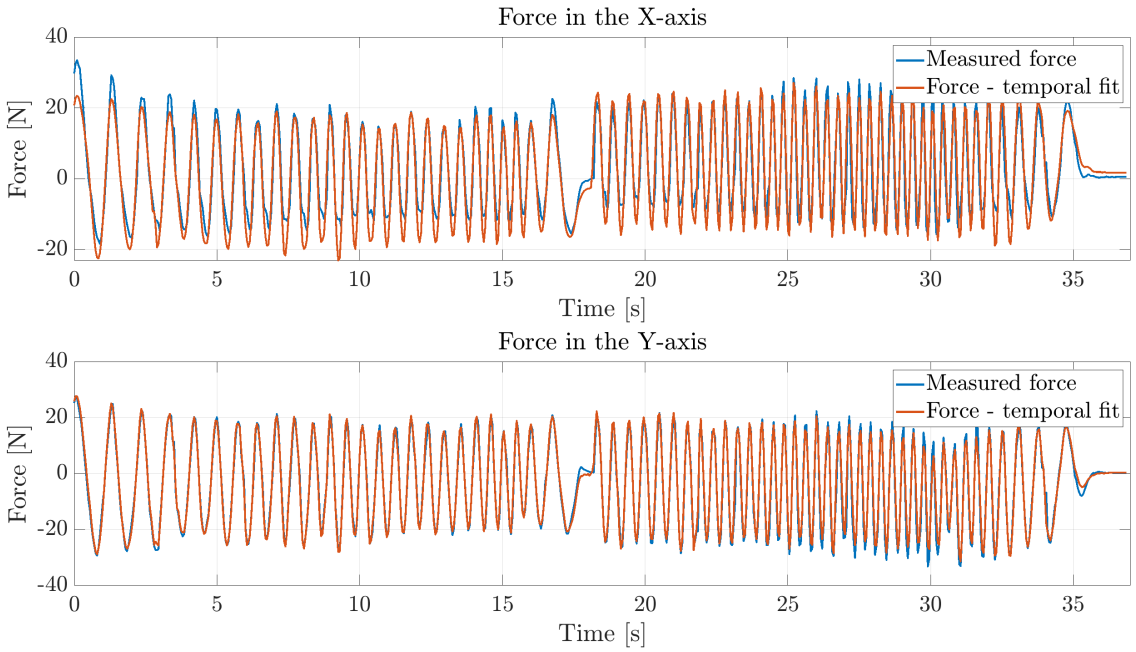

Figure 3.2: Measured and computed forces for point 2, maximum stiffness

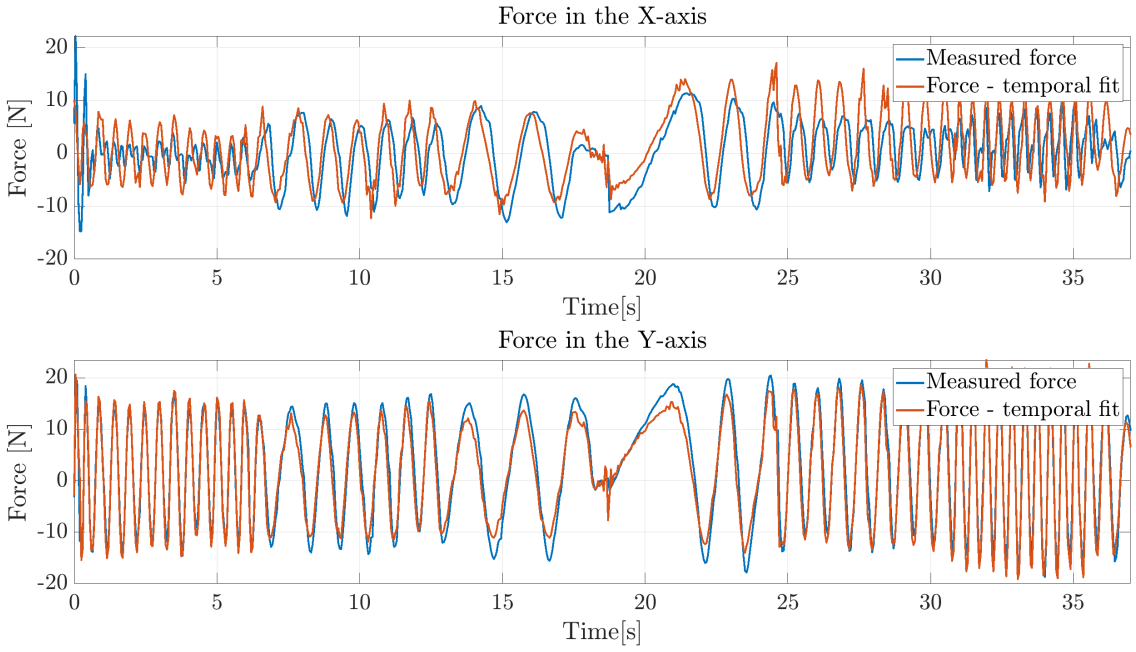

Figure 3.3: Measured and computed forces for point 3, minimum stiffness

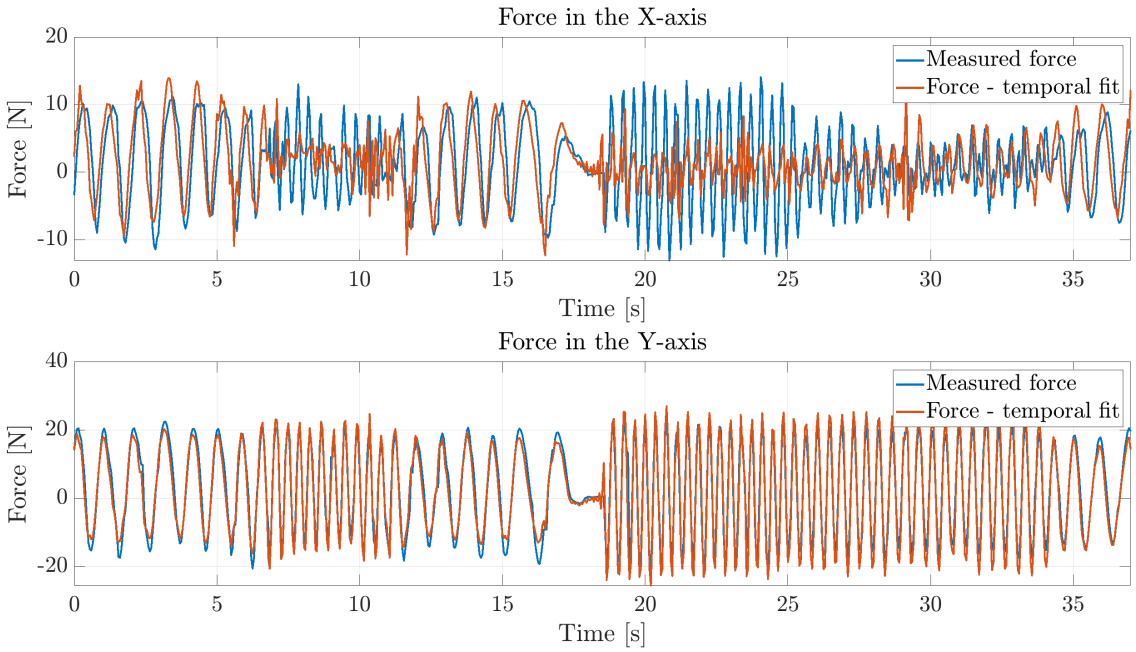

Figure 3.4: Measured and computed forces for point 3, maximum stiffness

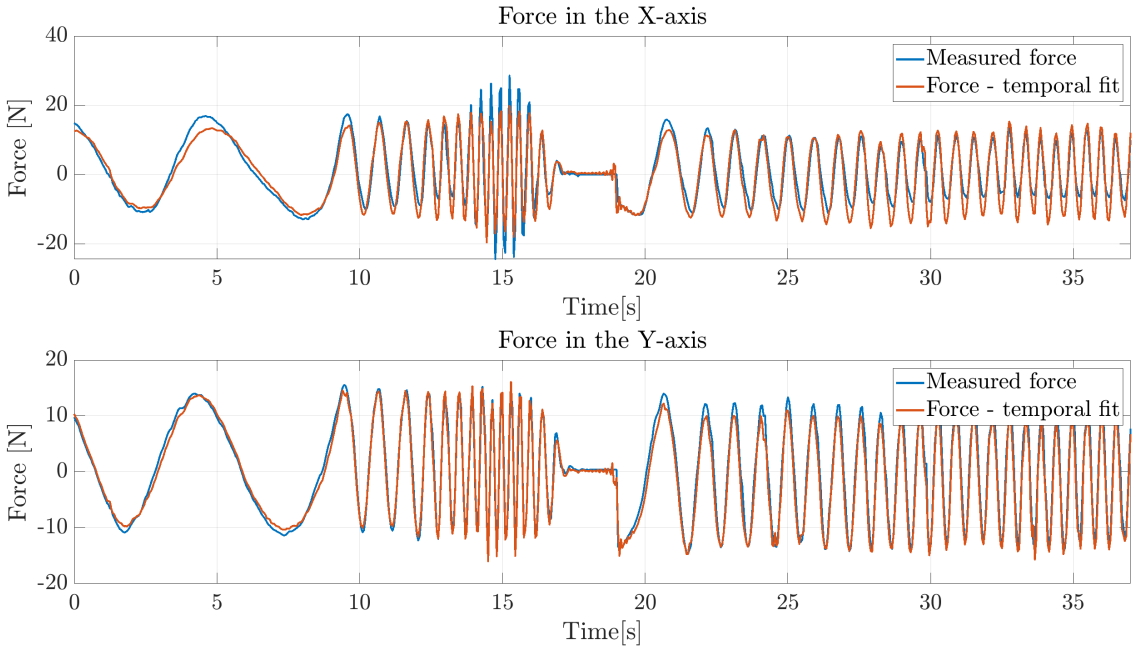

Figure 3.5: Measured and computed forces for point 4, minimum stiffness

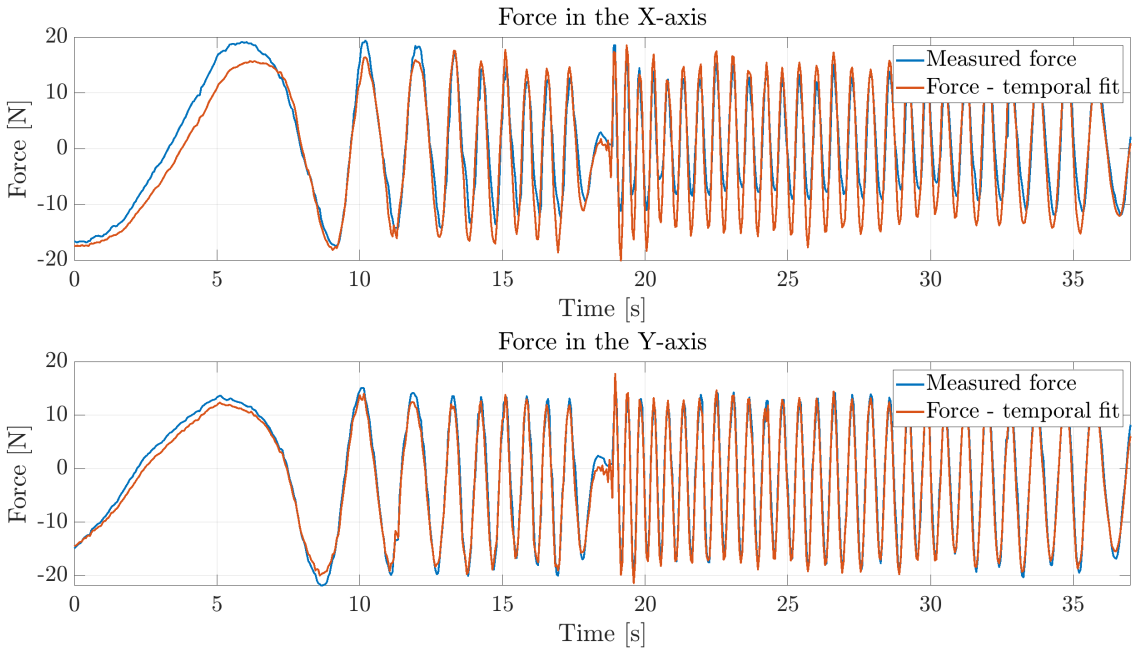

Figure 3.6: Measured and computed forces for point 4, maximum stiffness

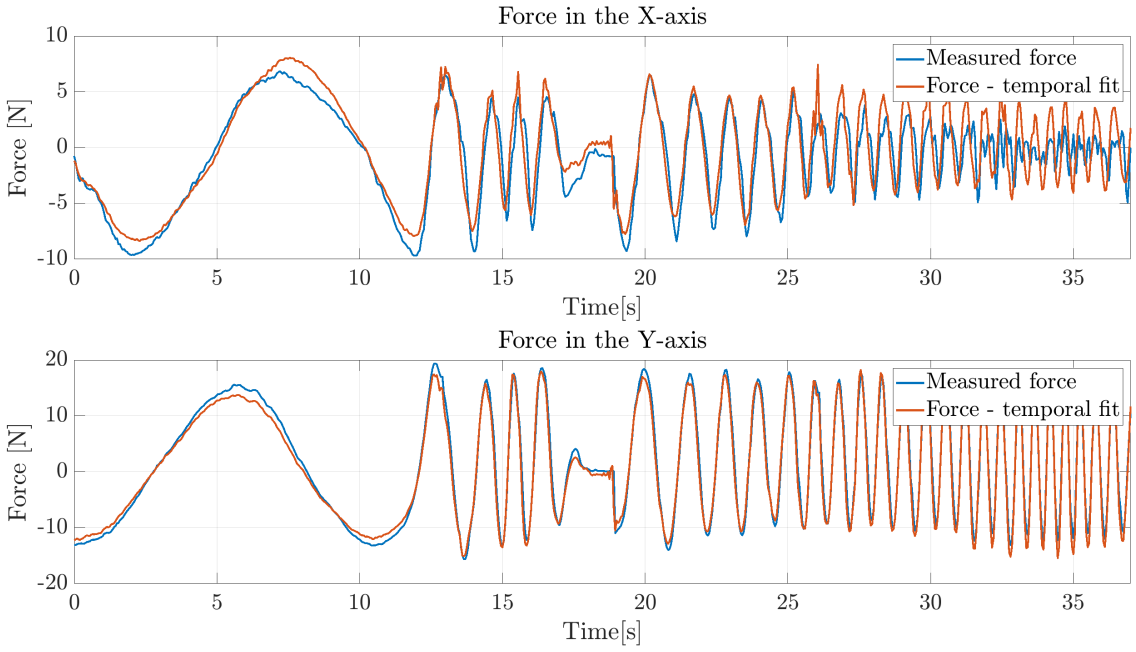

Figure 3.7: Measured and computed forces for point 5, minimum stiffness

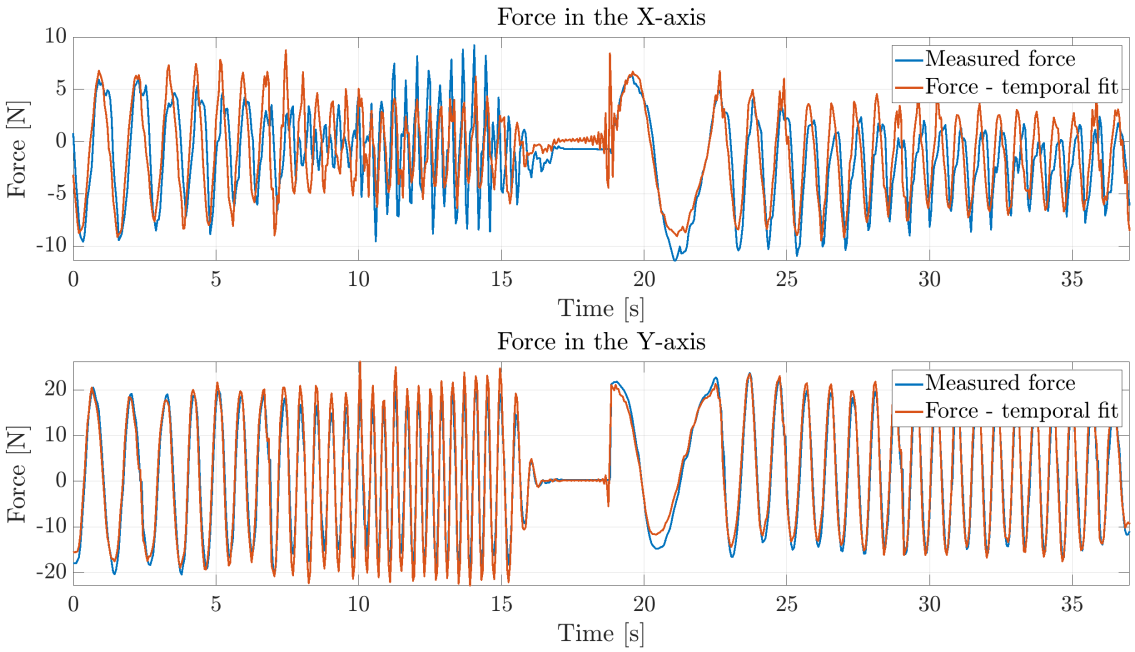

Figure 3.8: Measured and computed forces for point 5, maximum stiffness

Appendix D

Result for points 2 to 5 - frequency fit

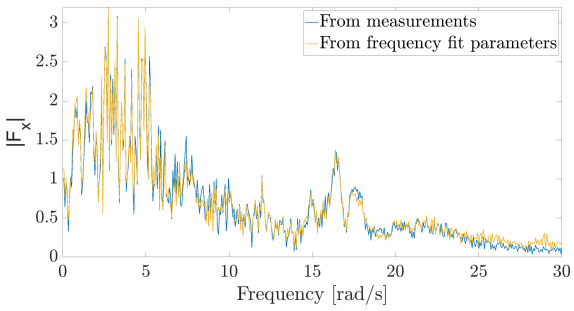

(a) X-axis force - Point 2

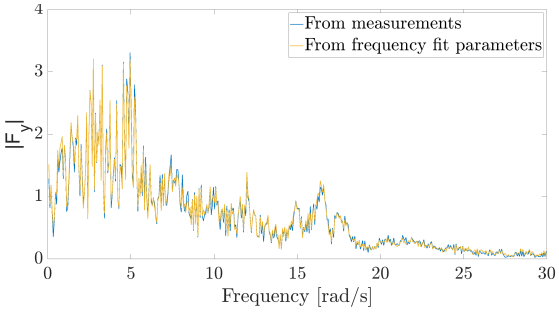

(b) Y-axis force - Point 2

Figure 4.1: Single sided amplitude spectrum of force signals - minimum configuration

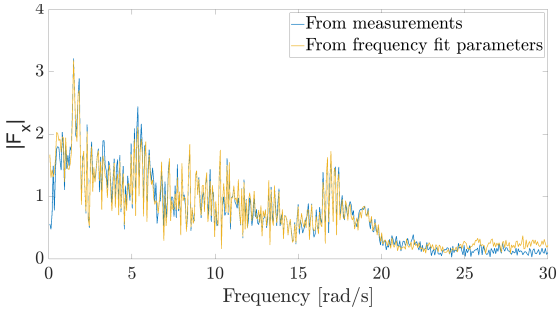

(a) X-axis force - Point 2

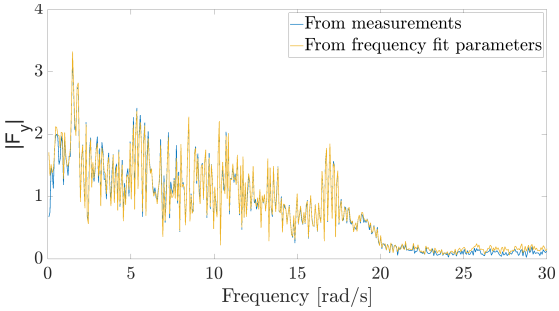

(b) Y-axis force - Point 2

Figure 4.2: Single sided amplitude spectrum of force signals - maximum configuration

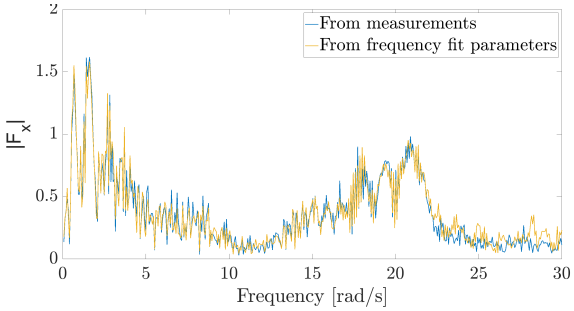

(a) X-axis force - Point 3

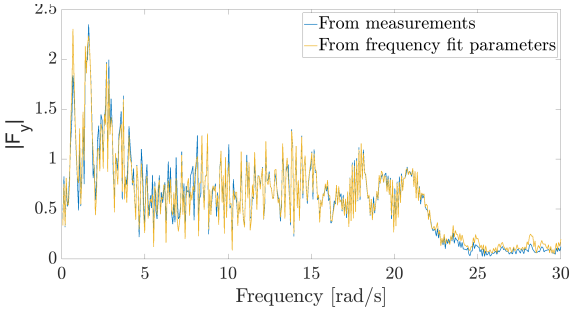

(b) Y-axis force - Point 3

Figure 4.3: Single sided amplitude spectrum of force signals - minimum configuration

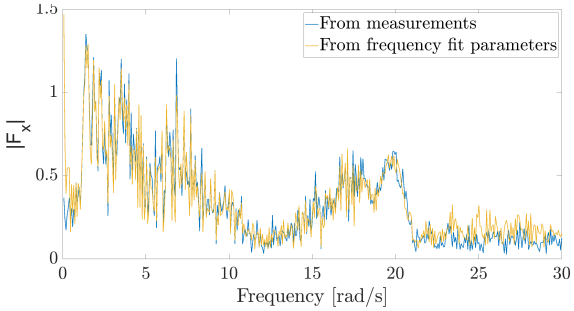

(a) X-axis force - Point 3

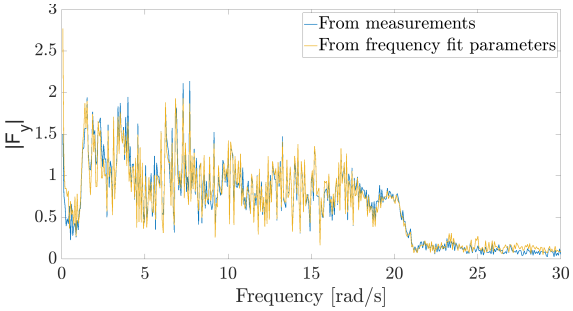

(b) Y-axis force - Point 3

Figure 4.4: Single sided amplitude spectrum of force signals - maximum configuration

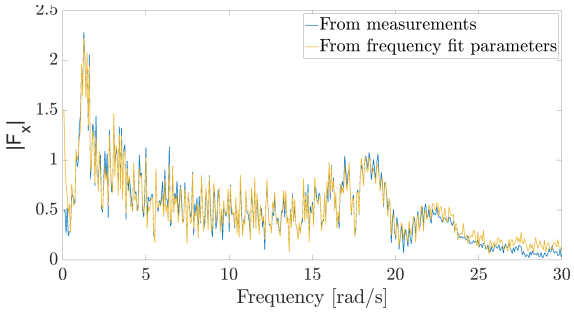

(a) X-axis force - Point 4

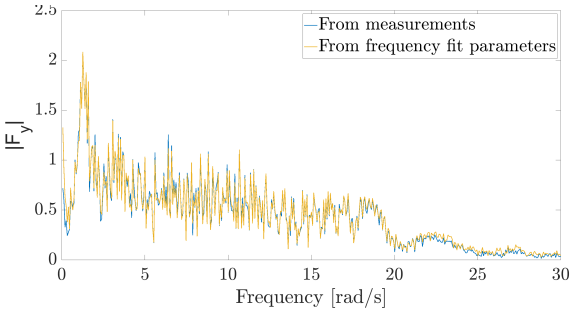

(b) Y-axis force - Point 4

Figure 4.5: Single sided amplitude spectrum of force signals - minimum configuration

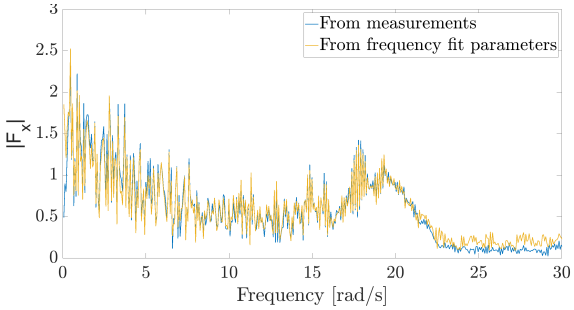

(a) X-axis force - Point 4

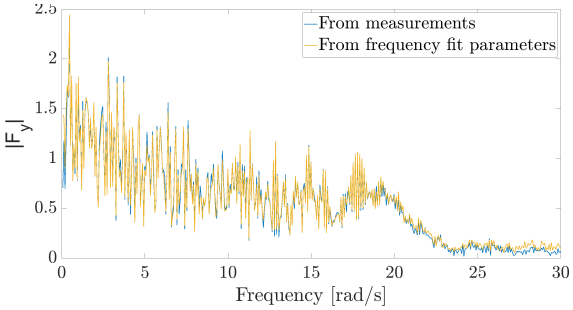

(b) Y-axis force - Point 4

Figure 4.6: Single sided amplitude spectrum of force signals - maximum configuration

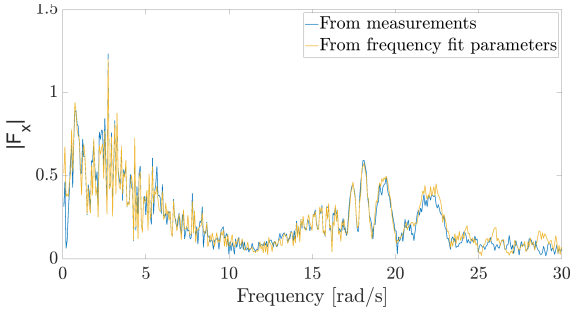

(a) X-axis force - Point 5

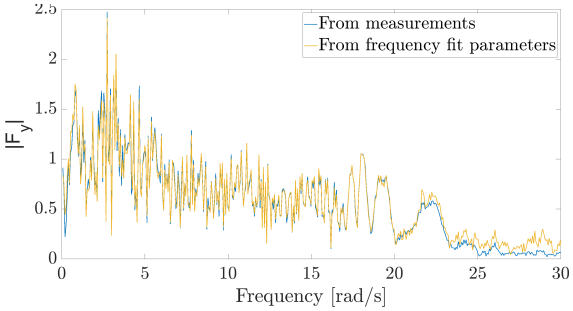

(b) Y-axis force - Point 5

Figure 4.7: Single sided amplitude spectrum of force signals - minimum configuration

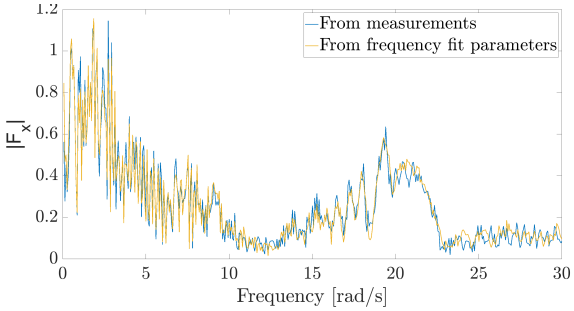

(a) X-axis force - Point 5

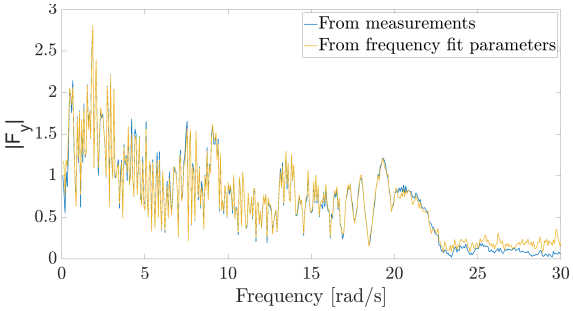

(b) Y-axis force - Point 5

Figure 4.8: Single sided amplitude spectrum of force signals - maximum configuration

UNIVERSITÉ CATHOLIQUE DE LOUVAIN
École polytechnique de Louvain
Rue Archimède, 1 bte L6.11.01, 1348 Louvain-la-Neuve, Belgique | **www.uclouvain.be/epl**